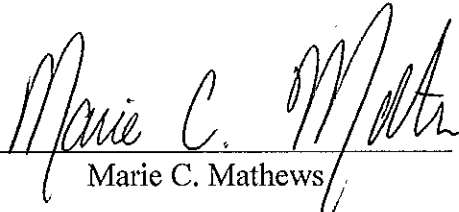


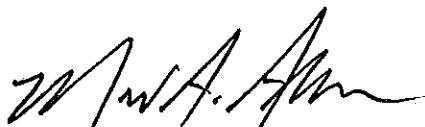
GEOMORPHIC EFFECTIVENESS OF MARSH TERRACING AS A COASTAL
RESTORATION TECHNIQUE IN SOUTHERN LOUISIANA

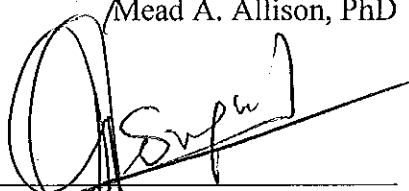
AN ABSTRACT

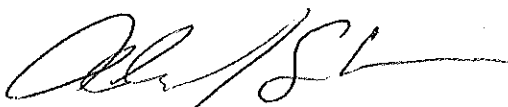
SUBMITTED ON THE THIRD DAY OF DECEMBER 2020
TO THE DEPARTMENT OF EARTH AND ENVIRONMENTAL SCIENCES
IN PARTIAL FULFILLMENT OF THE REQUIREMENTS
OF THE SCHOOL OF SCIENCE AND ENGINEERING
OF TULANE UNIVERSITY
FOR THE DEGREE
OF
MASTERS OF SCIENCE
BY


Marie C. Mathews

APPROVED:


Mead A. Allison, PhD


Ferbyörn E. Törnqvist, PhD


Alexander S. Kolker, PhD

ABSTRACT

Marsh terracing is a localized, lower-cost coastal restoration strategy often utilized in Gulf Coast wetlands in lieu of larger and more expensive projects, like sediment diversions and long-distance pipeline conveyance for marsh creation. Over 115 projects have been constructed to date in Louisiana since the 1990s as an aid to combat rapid wetland loss. These marsh creation efforts are generally sited in small water bodies (<5 km diameter) that have opened in basin wetlands by subsidence-driven internal collapse and/or marsh edge retreat. By creating ridges in these water bodies dredged from subaqueous *in situ* substrate, and planting terrace perimeters with colonizing marsh vegetation characteristic of the area, marsh terraces provide immediate marsh edge habitat and are predicted to interrupt fetch to reduce wave energies in basins where previously erosive waves generated basin bounding shoreline erosive retreat.

This study was designed to test assertions about the sediment benefits of extant marsh terrace projects in coastal Louisiana, specifically whether they (1) accelerate sediment trapping of particles brought in by hydrological exchange or organic matter generated locally, both subaqueously and on vegetated terrace tops, and (2) reduce shoreline erosion or interior land loss of the bounding marsh around the basin where they are placed. Field measurements such as feldspar-plots, short-period radiotracers (^7Be), and stratigraphic markers were utilized in the present study to show that deposition rates of trapped sediment are greatest within the lowest submerged areas of the marsh terrace field, specifically the excavation pits produced during construction. Accretion rates measured on subaerial marsh terraces is significant (up to 0.183 mm/d) during the winter-

spring frontal season when terrace tops are frequently submerged during high wind frontal events: rates decrease with increasing terrace elevation with the lowest accretion rates are observed at the crown (apex) of the terrace ridge. The subaerial and subaqueous particulate material accumulated within terrace fields is a mixture of autochthonous and allochthonous organic matter and mineral particles, consistent with the material accumulated in natural marshes across the Louisiana coast. These results from three terrace fields in different parts of the Mississippi delta support the concept that marsh terraces increase rates of sediment retention, with higher than natural rates of sediment deposition characteristic of south Louisiana concentrated in submerged areas. Over the longer term, this can be anticipated to reduce the bathymetric irregularities caused by excavation but not lead to subaerial emergence. This pattern of deposition is interpreted to be caused by reduced water velocities and total bed shear stresses within the field when hydrologic connectivity (water exchange) is low to intermediate, as higher degrees of water exchange appears to export more sediment out of the terraced basin.

Remote sensing analysis of 10 terrace projects across coastal Louisiana to examine wetland area change in the periods before and after project construction shows that terrace presence does reduce shoreline erosion along the bounding marsh in a slight majority of sites (6 of 10). This is interpreted to be a byproduct of interrupting wave fetch that would otherwise produce erosive waves and higher water velocities capable of eroding bounding basin shorelines. Imagery shows that at some sites where fetch remains high in project basins, terraces show evidence of “sacrificial” erosion that protects the adjacent shoreline against which they were built. Terraces also were shown in imaging results from several sites to reverse bounding shoreline wetland edge loss and

display marsh accretion either along the shoreline or in the marsh interior. All of the sites that did not show a benefit in reducing land loss in their basins were examples where hurricane passage within the first year of project construction damaged both the terraces and extant wetlands.

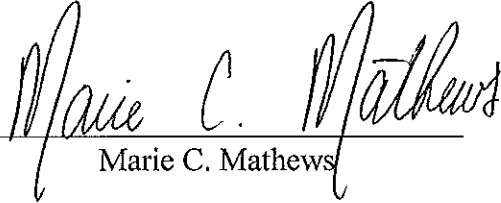
Numerical simulations of terraces were performed in a synthetic basin to test various terrace designs (i.e., linear, chevron, box) relative to the orientation of the wave-current field. Results showed that placing terraces in the synthetic basin reduced water velocities and total bed shear stresses inside the field and in the lee of the tested winds. These factors were enhanced around the edges of the field. The leeward effect can be anticipated to “shadow” the basin-bounding marsh shoreline from wave-current induced marsh retreat if build close enough (<500 m) from the shoreline: closer locations will reduce energies further but will decrease the linear section of shoreline protected. The observed reduction in bed shear stress inside the field can be expected to facilitate sediment trapping in the subaqueous portion of the terrace field, as observed in the field results. Results suggest that marsh terraces should be constructed perpendicular to the strongest winds, which are typically the NNW-SSE winds associated with cold front passages through the winter and early spring in coastal Louisiana. Further, constructing marsh terrace projects during the winter months (November – February), instead of the Spring-Summer as is usually practiced, will maximize the time for terrace ridges to consolidate prior to the tropical storm season later in the year. Overall, this study has shown that marsh terracing appears to be a generally successful strategy along the Louisiana coast for reducing marsh erosion in coastal water bodies, and for improving sediment retention. These results should motivate both additional studies to optimize

design and encourage project construction in the future as a tool to combat wetland loss in Louisiana.

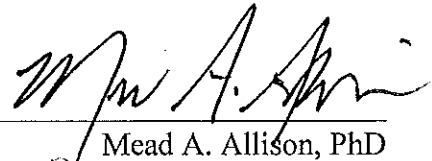
GEOMORPHIC EFFECTIVENESS OF MARSH TERRACING AS A COASTAL
RESTORATION TECHNIQUE IN SOUTHERN LOUISIANA

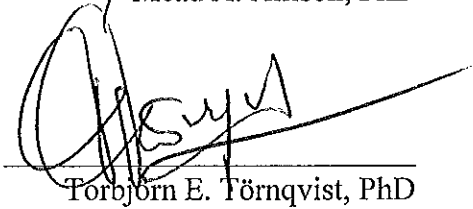
A THESIS

SUBMITTED ON THE THIRD DAY OF DECEMBER 2020
TO THE DEPARTMENT OF EARTH AND ENVIRONMENTAL SCIENCES
IN PARTIAL FULFILLMENT OF THE REQUIREMENTS
OF THE SCHOOL OF SCIENCE AND ENGINEERING
OF TULANE UNIVERSITY
FOR THE DEGREE
OF
MASTERS OF SCIENCE
BY


Marie C. Mathews

APPROVED:


Mead A. Allison, PhD


Torbjörn E. Törnqvist, PhD


Alexander S. Kolker, PhD

ACKNOWLEDGEMENTS

I am so grateful for the time I spent in New Orleans and with Tulane's Department of Earth and Environmental Sciences and its Department of River-Coastal Science and Engineering. Mead Allison has been an incredible advisor, pushing me to become a stronger scientist (and person) with his immeasurable patience and dedicated mentorship. This would have been a much more dull experience without his stories in and out of the field.

I would also like to thank my committee members, Tor Törnqvist and Alex Kolker, for their support from start to finish with a special thank you to Alex for always going out of his way to check in throughout this process. Additionally, I'd like to extend a huge thank you to Ehab Meselhe and Kelin Hu for their guidance (and patience) as I took my inaugural dive into numerical modeling. I also thank Louisiana's Coastal Protection and Restoration Authority for their funding through the Coastal Science Assistantship Program, as well as ConocoPhillips & Ducks Unlimited – especially Mike Brasher – for sharing site access and data throughout this project.

Thank you to all the friends I've made in New Orleans and beyond who offered essential support during and comedic relief from this whole journey – especially my phenomenal confidants and role models: Dana Carstens, Catherine Fitzpatrick, Sabrina Martinez, Rachel Sortor, Udit Mukherjee, and Ryder Myers. Huge thanks to my Tulane (now Vicksburg!) partner-in-crime Autumn Murray, too – looks like we'll be doing science together for a while, and I couldn't be happier.

This thesis is dedicated to Douglas Mathews, Diane and William Lucca, as well as my extraordinary grandparents, Bob and Diane Sayegh. Without your love, encouragement, and occasionally feigned but always enthusiastic interest in my research, I wouldn't have gotten here. You all know I'm stoked about where I am, so thank you a million times over.

Pressure makes diamonds.

Table of Contents

ACKNOWLEDGEMENTS.....	ii
LIST OF TABLES.....	v
LIST OF FIGURES.....	vi
SECTION 1: INTRODUCTION.....	1
SECTION 2: BACKGROUND.....	6
2.1 Wetland Loss Rates in Coastal Louisiana.....	6
2.2 Marsh Loss Mechanisms.....	7
2.3 Marsh Accretion Mechanisms.....	10
2.4 Marsh Terracing.....	13
SECTION 3: METHODS.....	20
3.1 Field Methods.....	20
3.1.1 Site Selection.....	20
3.1.2 Sediment Sampling.....	26
3.1.3 Feldspar Marker Horizons.....	28
3.1.4 Elevation Measurements.....	29
3.1.5 Bathymetric Mapping.....	31
3.2 Laboratory Methods.....	32
3.2.1 Core Processing.....	32
3.2.1.1 Bulk Properties & Sedimentary Facies.....	32
3.2.1.2 Granulometry.....	34
3.2.1.3 Radioisotope Analysis.....	35
3.2.2 Geospatial (Remote Sensing) Wetland Area Analysis.....	36
3.2.2.1 Site Selection.....	36
3.2.2.2 Image Acquisition.....	37
3.2.2.3 Image Processing.....	38
3.2.2.4 Classification Accuracy Assessment.....	40
3.3 Numerical Model.....	41
3.3.1 Model Software.....	42
3.3.2 Model Setup.....	43
3.3.3 Bathymetry.....	44
3.3.4 Simulation Settings.....	47
SECTION 4: RESULTS.....	48
4.1 Short-term deposition.....	48
4.1.1 Feldspar & ⁷ Be Deposition Rates.....	49

4.2 Characteristics of Short-term Sediment Deposition.....	57
4.2.1 Bayou Monnaie.....	57
4.2.2 Yankee Canal.....	58
4.2.3 Bay Alexis.....	59
4.3 Core Stratigraphy and Properties.....	60
4.4 Remote Sensing Analysis.....	64
4.4.1 Overall Marsh Area Change in Terrace Fields.....	65
4.4.2 Overall Interior and Exterior Marsh Area Change.....	66
4.4.3 Classification Accuracy Assessment.....	71
4.5 Numerical Modeling of Hydrodynamic Impacts of Terrace Designs...	73
SECTION 5: DISCUSSION.....	78
5.1 Effect of Marsh Terracing on Nearfield Sediment Deposition and Marsh Stability.....	78
5.1.1 Sediment Deposition Patterns in Terrace Fields and Implications for Marsh Emergence.....	79
5.1.2 Geospatial Evidence for Increased Sediment Retention.....	86
5.1.3 Reduction of Bounding Shoreline Marsh Erosion.....	89
5.1.4 Role of Tropical Storms.....	93
5.2 Insights into Terrace Geometry and Orientation on Performance.....	98
5.2.1 Terrace Geometry.....	98
5.2.2 Terrace Orientation.....	101
SECTION 6: CONCLUSIONS.....	101
REFERENCES CITED.....	105
APPENDICES.....	124
Appendix A: Feldspar Deposition Rates and Layer Characteristics in Terraces.....	124
Appendix B: Remote Sensing Category Change Results.....	140
Appendix C: Numerical Modeling Supplementary Results.....	143
Appendix D: Hydrological Connectivity Analysis for Remote Sensing Study Sites.....	146
BIOGRAPHY.....	148

List of Tables

Table 1. ^{7}Be deposition rates from unconsolidated depths.

Table 2. ^{7}Be deposition rates and inventories from consolidated depths.

Table 3. ^{7}Be deposition rates and mass fluxes recalculated without activities = 0 dpm/g.

Table 4. Integer to corresponding change definitions for remote sensing analysis.

Table 5. Annual marsh land change at each remote sensing study site before and after terrace construction.

Table 6. Interior (terrace field) and exterior (bounding marsh) annual marsh land area change after terrace construction.

Table 7. Kappa coefficients for each classified image across all 40 images utilized in the remote sensing study.

Table 8. Deposition (minimum and maximum) vs. RSLR rates at field sites.

Table 9. Conversion of water to mudflat (mudflat development) at remote sensing sites.

Table 10. Factors impacting terrace performance against overall terracing project success.

Table 11. Gap-to-structure ratio and energy dissipation efficacy by terrace geometry.

List of Figures

Figure 1. Modified map of predicted land loss in coastal Louisiana without intervention.

Figure 2. Shallow subsidence rates across coastal Louisiana modified from Neinhuis et al. (2017).

Figure 3. Water bodies of coastal Louisiana with sufficient fetch for wave generation to cause marsh edge erosion.

Figure 4. Vertical accretion surplus and deficit rates across coastal Louisiana.

Figure 5. Three dominant marsh terrace designs (geometries).

Figure 6. Terrace perimeter plants with vegetation (*S. alterniflora*) sprigs.

Figure 7. Distribution and orientation of marsh terraces and fields within basins.

Figure 8. Spatial distribution of terrace projects and year of construction (emplacement).

Figure 9. Field study sites.

Figure 10. Bayou Monnaie.

Figure 11. Yankee Canal.

Figure 12. Bay Alexis.

Figure 13. Location of excavators during marsh terrace construction at Bay Alexis.

Figure 14. Peat auger core (BM13) from Bayou Monnaie.

Figure 15. Feldspar marker horizon plots.

Figure 16. Geospatial analysis (remote sensing) study sites.

Figure 17. Representative classified image (Site 2015E).

Figure 18. Representative distribution of classification accuracy assessment points.

Figure 19. Simplified model domain.

Figure 20. Model grid resolution.

Figure 21. Assigned and interpolated linear terrace model bathymetry.

Figure 22. Deposition rates derived from feldspar at Bayou Monnaie.

Figure 23. Deposition rates derived from feldspar at Yankee Canal.

Figure 24. Relationship between feldspar accretion rates and elevation (NAVD88).

Figure 25. Unconsolidated ⁷Be-derived deposition rates and inventories at Bay Alexis.

Figure 26. Representative unconsolidated and consolidated downcore ⁷Be activities.

Figure 27. Properties of Bayou Monnaie feldspar plot samples against elevation (NAVD88).

- Figure 28.* Properties of Yankee Canal feldspar plot samples against elevation (NAVD88).
- Figure 29.* Properties of Bay Alexis cores against elevation by location.
- Figure 30.* Stratigraphic illustration of transect collected at Bayou Monnaie.
- Figure 31.* Stratigraphic illustration of transect collected at Yankee Canal.
- Figure 32.* Subaqueous piston cores collected at Yankee Canal.
- Figure 33.* Change map showing marsh land gain along bounding marsh (2015E).
- Figure 34.* Change map showing marsh land gain within marsh interior (7001).
- Figure 35.* Change map showing accelerated marsh land loss following terrace construction (5001).
- Figure 36.* Change map showing interior and exterior change with marsh land area change concentration along the bounding shoreline (2015E).
- Figure 37.* Change map showing interior and exterior change with marsh land area change concentrated within terrace field (3008).
- Figure 38.* True color to classified image with highest index of agreement shown (2015E).
- Figure 39.* True color to classified image with lowest index of agreement shown (2015W).
- Figure 40.* Hydrodynamic impacts of lower linear terraces.
- Figure 41.* Hydrodynamic impacts of lower grid terraces.
- Figure 42.* Hydrodynamic impacts of lower chevron terraces.
- Figure 43.* Impacts of hurricane passage on recently constructed terracing projects.
- Figure 44.* Long-term impacts of hurricane passage on terracing projects.
- Figure 45.* Mean velocity field around an impermeable ($\Phi = 0$) structure modified from Chan et al. (2012).

1. Introduction

Coastal wetlands account for < 5% of global land mass (Tiner, 1984), but these mangrove swamps, freshwater and salt marshes, and mud flats have supported high ecological productivity and human development for millennia (Mitsch and Gosselink, 1993; Michener et al. 1997). Civilizations across the world have been cradled by coastal wetland environments from China to the Middle East to the East and West Coasts of the United States (Bildstein et al. 1991). With as much as 70% of the global population estimated to reside within the coastal zone and upwards of 40% of those in the United States living in coastal counties (NOAA, 2020), environments like coastal wetlands are critically important for the sustained development and functionality of human coastal communities. Coastal wetlands feature waterways that are available for, or have been modified to allow navigation, providing a route for essential transportation and trade; this, in part, led to the growth of communities like Boston, New York City, and New Orleans along – or atop – coastal wetlands. In addition to cradling human settlements and encouraging the growth of civilizations, coastal wetlands serve as a vital ecotone between terrestrial and marine environments. By integrating these two ecosystems, coastal wetlands host a wide array of unique species and rank as one of the most productive natural ecosystems (Whittaker and Likens, 1971; Odum, 1979). Through primary and especially secondary productivity, coastal wetlands create and distribute considerable energy to support large food webs and high species richness (Bildstein et al. 1991). Furthermore, coastal wetlands offer carbon sequestration capabilities, with coastal wetlands recording the highest rates of carbon sequestration per unit area of all natural ecosystems (Rogers et al. 2019). Their functionality as carbon sinks is widely

recognized (Adams et al. 1990; Chmura et al. 2003), giving coastal wetlands a prominent role in global climate regulation.

Despite their ecological importance and societal value (Mitsch and Gosselink, 2000), coastal wetlands are endangered along many coastlines by continued coastal development and accelerating climate change (Bildstein et al. 1991; Lin and Yu, 2018; Rogers et al. 2019). As coastal communities expand, coastal wetlands are drained, polluted, or otherwise modified so significantly that their ecological functionality is impaired or eliminated. Climate change puts coastal wetlands at risk because although many coastal wetlands have evolved to keep pace with relatively slow rates of sea level rise, and to withstand a particular frequency and intensity of storms, where even slight changes to these patterns may substantially impact coastal wetlands and their essential processes (Michener et al. 1997; Knutson et al. 2010; Kirwan and Megonigal 2013). If unable to compete with rising seas or strengthened storms, then coastal wetlands risk drowning and erosive disappearance. In regions like the United States' Gulf Coast, where rising seas are often coupled with high rates of subsidence (Liu et al. 2020), coastal wetlands are in even graver danger. Multiple anthropogenic drivers also exacerbate the threat; levee construction, canal cutting, sediment supply disruption, and subsurface fluid extraction all contribute to wetland loss and are pervasive across the State of Louisiana (Turner, 1997; Day et al. 2000; Morton et al. 2006; Blum and Roberts, 2009; Kolker et al. 2011; Couvillion et al. 2011; Jankowski et al. 2017; White et al. 2019). In coastal Louisiana, these practices, in conjunction with sediment compaction-driven subsidence and eustatic sea level rise lead to relative sea level rise (RSLR) rates that average 9.5 ± 6.3 mm/yr and 13.2 ± 8.8 mm/yr in Louisiana's Chenier Plain and its

Delta, respectively (Figure 1; Jankowski et al. 2017). These conditions strain wetlands' natural ability to accrete vertically at rapid enough rates to outpace rising sea level; an estimated 58% of marshes across the state are estimated to be unable to keep pace with present rates of RSLR, the range of which varies spatially from 0.1 to 29.4 mm/yr (White et al. 2019).

To combat coastal wetland loss, Louisiana has devoted billions of dollars towards coastal restoration. Following Hurricanes Katrina and Rita in 2005, Louisiana established its Coastal Protection and Restoration Authority (CPRA) to coordinate local, state, and federal efforts to restore and protect the coast. Every five to six years since its inaugural report in 2007, CPRA develops and publishes a Comprehensive Master Plan for a Sustainable Coast (Coastal Master Plan 2017), which aggregates the best available science and engineering to predict the condition of the coast and evaluates and selects restoration and protection initiatives to be enacted over the next 50 years. Considering various scenarios of intervention and the case of no action, this plan allocates \$50 billion

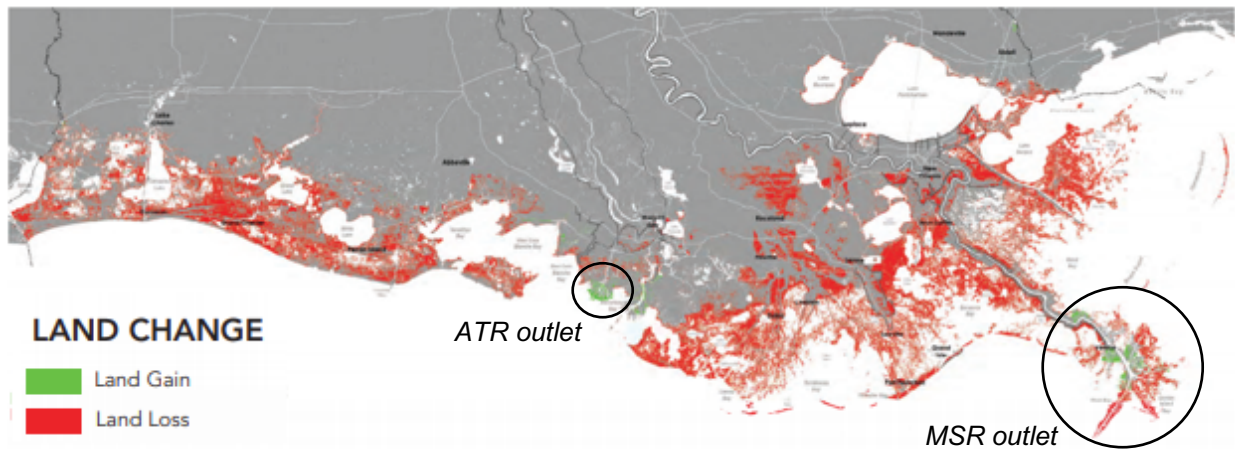


Figure 1. Modified map of predicted land loss in coastal Louisiana without intervention (e.g., Future Without Action) as modeled in Louisiana's CPRA 2017 Comprehensive Plan for a Sustainable Coast (Coastal Master Plan). Without intervention, land loss will predominate except for restricted regions close to the Mississippi and Atchafalaya River sediment sources (see the circled Mississippi River (MSR) outlet and Atchafalaya River outlet (ATR)).

(about \$1 billion/y) towards large and small initiatives proposed by the public, private enterprises, as well as universities and state scientists as well as levees and other forms of protection. One of many smaller, less expensive marsh protection and restoration strategies mentioned in this plan and implemented across Louisiana using Federal, State, and private funds is known as marsh terracing, and it has gained attention as a green alternative to structural features like levees to protect and stabilize shorelines. First implemented in the late 1980s, marsh terracing involves excavation of local subtidal substrate and its placement into subaerial ridges within a coastal water body, which are built to be elevated above the mean water level surface by 0.5 m to allow for periodic inundation (Rozas and Minello, 2001; Brasher, 2015).

Given their relatively simple design of fields and ridges in linear, chevron, or grid (box) shapes separated by intervening water segments, marsh terraces projects are relatively low cost to construct and require limited space for implementation: this has made marsh terraces to become a coastal restoration tool accessible to local governments and smaller non-governmental organizations (NGOs) that may not have the funds or land area to implement large-scale projects. Despite their low cost and ease of implementation, the efficacy of marsh terraces has not been extensively researched (Steyer, 1993; Brasher, 2015). The proposed benefits of marsh terraces can be classified as either ecological or morphological in nature, with the majority of research evaluating the ecological efficacy of marsh terracing (Rozas and Milleno, 2001; Bush Thom et al. 2004; Rozas and Milleno, 2007; Rozas and Milleno, 2009; Brasher, 2015), with the ascribed benefits for land gain and preservation remaining relatively untested. Among the proposed benefits often used as justification for their construction in project design

plans are increased marsh edge, enhanced habitat for nekton and waterbirds, increased sediment deposition, and the encouragement of emergent marsh.

The goal of the present thesis is to assess the geomorphic effectiveness of marsh terracing through a combination field study, remote sensing analysis, and numerical model simulations, adding to the limited number of studies of the morphological benefits that have been conducted to date (Steyer, 1993; Brasher, 2015; French, 2020; Osario and Linhoss, 2020). The present thesis will test the following hypotheses, that, if properly engineered, marsh terraces will:

- i. Encourage sediment trapping in the water body within the field and on the vegetated terraces if sufficient material or allochthonous organic matter is available,
- ii. Reduce marsh land loss in smaller basins and wetland edge erosion if the pre-construction water body fetch is sufficiently large,
- iii. Terrace design – geometry, placement, and orientation – will impact the magnitude of i) and ii)

As the 2023 Coastal Master Plan is under development, it is particularly important to understand the efficacy of marsh terracing as a land building and preservation tool, now that it has been utilized for several decades to construct several dozen projects, because it is one of multiple strategies being considered for future use in wetland restoration and protection. If deemed effective in the State's widely disseminated plan, state and local governments, NGOs, and other private organizations may choose to fund additional

marsh terracing sites in Louisiana and elsewhere, which may augment the wetlands' own efforts to grow and outpace RSLR, allowing these indispensable environments to survive for future generations.

2. Background

2.1 Wetland Loss Rates in Coastal Louisiana

Louisiana wetlands account for 40% of coastal wetlands in the continental United States and 80% or more of its total coastal wetland loss (Boesch et al. 1994). From 1932 to 2016, Louisiana lost 25% (approximately 4,833 km²) of its wetland area; this loss has occurred at non-linear rates over time, varying from -28 ± 16 km² to -83 ± 11 km² per year (Couvillion et al. 2017). Wetland loss is the conversion of vegetated marsh to upland or drained areas, unvegetated mudflats, or submerged environments (Boesch et al. 1994). In Louisiana, this wetland loss is largely loss to open water and is driven by subsidence and marsh edge erosion, both of which are caused by a combination of natural and anthropogenic processes (see §2.2 Marsh Loss Mechanisms). Although land loss rates have slowed in recent years, recent rates are still equivalent to the loss of an American football field (5,351 m²) every 100 minutes (Couvillion et al. 2017). Conservatively, the United States Geological Survey (USGS) has estimated Louisiana may lose its wetlands within the next 200 years. However, other more recent studies suggest virtually all remaining coastal wetlands will convert to open water within the next 50 years if global sea level rise exceeds 6-9 mm/y (Törnqvist et al. 2020). The CPRA 2017 Master Plan (CPRA, 2017) predicts a “Future Without Action” – where no intervention is implemented to slow or reverse wetland loss – of significant land loss

across coastal Louisiana in the next 50 years, with only small areas of land gain in isolated regions of the Mississippi River (MSR) and Atchafalaya River (ATR) outlets (Figure 1). Based on these assessments and many others, Louisiana wetlands and the crucial habitats they house are at risk of not surviving the 21st century without effective intervention.

2.2 Marsh Loss Mechanisms

Subsidence occurs in Louisiana at depth and at the shallow subsurface (< 5 m), and while the rates and drivers of subsidence vary spatially and with depth, both threaten low-elevation coastal zone marshes by lowering the land surface and exacerbating RSLR (Figure 2; Meckel et al. 2006; González and Törnqvist, 2009; Yuill et al. 2009; Jankowski et al. 2017; Nienhuis et al. 2020). Subsidence at depth is due to isostasy and fault movement, but it occurs at a slower rate than shallow subsidence (González and Törnqvist, 2009; Wolstencroft et al. 2014; Jankowski et al. 2017). Shallow subsidence (SS) is primarily due to sediment compaction and fluid extraction (Meckel et al. 2006; González and Törnqvist, 2009; Yuill et al. 2009; Jankowski et al. 2017; Nienhuis et al.

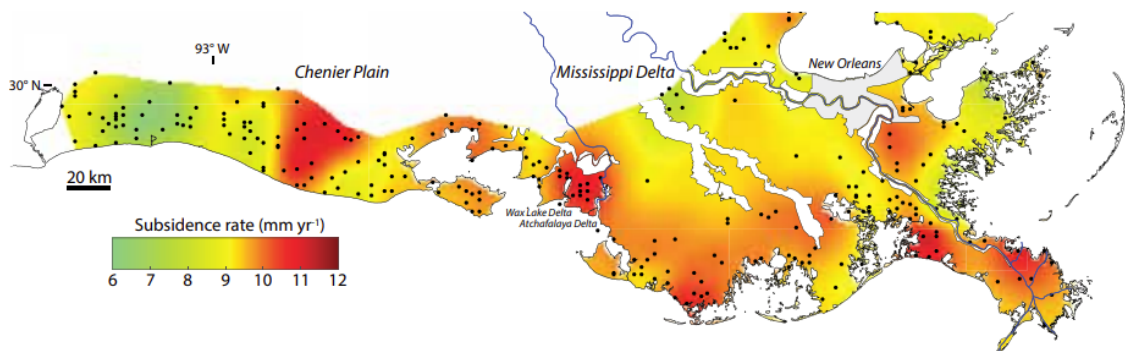


Figure 2. Geostatistical interpolation of calculated shallow subsidence rates across coastal Louisiana from 274 Coastwide Reference Monitoring System (CRMS) stations (modified from Nienhuis et al., 2017). CRMS stations locations are represented by the black dots.

2020). The quantification of these natural and anthropogenic drivers has been debated (Meckel et al. 2006), but recent measurements have estimated total subsidence rates in coastal Louisiana average 9 ± 1 mm/y, and have determined that the majority of subsidence occurs at shallow depths (Jankowski et al. 2017; Nienhuis et al. 2017; Keogh & Törnqvist, 2019). Organic-rich deposits – like peat typically found in Louisiana marshes – undergo compaction after formation and initial burial, and these rapid compaction rates are documented across recent and ancient coastal strata (Törnqvist et al. 2008). Fluid extraction also accelerates subsidence by decreasing soil porosity and decreasing hydrostatic pressure as fluids are removed, which increases overburden pressure-induced soil compaction (Yuill et al. 2009; Kolker et al. 2011). As soils compact, their elevations decrease, driving subsidence.

In conjunction with subsidence exacerbating RSLR, the erosion of wetlands also is a primary mechanism for the land loss experienced across Louisiana's coastal wetlands. Even in the absence of sea level rise, wave-induced edge erosion can cause land loss; in periods of high wave energy when the marsh is not submerged, waves exert the maximum wave thrust onto the marsh scarp – a ubiquitous wetland edge feature where bare sediment is exposed beneath the vegetation – which can cause erosional retreat of the scarp (Fagherazzi et al. 2013). This water level condition is frequently met during a tidal cycle, so marsh edge degradation could persist even in the absence of other drivers (Fagherazzi et al. 2013). Additionally, independent of RSLR, marsh edge erosion can also cause lateral shoreline retreat of interior ponds that may have initially been created by subsidence-induced collapse (Ortiz et al. 2017): this expansion creates a negative feedback-system where, as inland ponds increase in size due to erosion or

subsidence, fetch increases across the water body, increasing wave size and energy, and thus increasing wave-induced edge erosion (Ortiz and Edmonds, 2016; Allison et al. 2017).

Other feedback drivers are present in Louisiana coastal wetlands and continue to exacerbate marsh edge erosion. Canalization, or canal cutting, was a popular excavation technique utilized prior to the 1960's to traverse Louisiana wetlands for hydrocarbon extraction or navigation to coastal communities. This fragmented wetlands, increased marsh edge exposure to wave attack, removed adjacent wetland due to canal margin slumping, and impacted the hydraulic and hydrologic regime (Craig et al. 1980). Given its pervasiveness along canals and shorelines bounding larger water bodies, marsh edge erosion is a significant and known mechanism for wetland loss in Louisiana and has been repeatedly suggested as one of the primary drivers of shoreline retreat in coastal wetlands (Nyman et al. 1994; Wilson and Allison, 2008; Morton et al. 2009; Allison et al. 2017; Sapkota and White, 2019; Elsey-Quirk et al. 2019). However, not all waves are capable of eroding marsh edges. To form waves with energy capable of eroding marsh edges, there must be approximately four km or more of uninterrupted fetch over water body depths that are typical in coastal Louisiana (Allison et al. 2017). In Louisiana, the marshes bounded by the Gulf of Mexico are all susceptible to fetches this great, as are many inland bays, lakes, and larger ponds (Figure 3). Even in smaller coastal water bodies, expansion may continue driven by subsidence, until water bodies become large enough where marsh edge erosion also may become a second driver.

known rather than assumed; therefore, understanding local accretion is an important component of any restoration project.

The organic components of vertical accretion of coastal marshes may be autochthonous or allochthonous. Autochthonous biomass production occurs above- and belowground (e.g., roots and shoots), with aboveground biomass including stems per area and leaf mass and belowground biomass referring to live root mass (Mitsch and Gosselink, 2015). Belowground productivity leads to marsh surface elevation as roots grow and displace the overlying soil. In coastal Louisiana, above- and belowground productivity indicate seasonal responses, but the magnitude of these seasonal components varies by species composition (Hopkinson et al. 1978). While not strictly “autochthonous”, inorganic (mineral particle) constituents may be derived from erosion within the local marsh system from lateral erosion of shorelines associated with pond expansion or resuspension of pond bottoms during storms, and both can supply sediment for redistribution within a basin (Cahoon and Turner, 1989). Allochthonous inorganic material is supplied by hydrologic connectivity to external sediment sources such as rivers, estuaries or the Gulf of Mexico (GOM) delivered by tides or storm events (Nyman et al. 2006; Turner et al 2006).

Biological and hydrological regimes affect mineral sediment deposition; the former can influence the rate and spatial distribution of sedimentation, while the latter governs external sediment sourcing and access. Without sufficient sediment, coastal wetlands will be unable to accrete enough to compete with RSLR, risking permanent inundation and ultimately, marsh loss (Jankowski et al 2017). Both the biological and hydrological regimes will govern organic accumulation, as well. Biology impacts

sedimentation because sediments tend to deposit at the highest rates where plant density (i.e., stem density) is greatest, including forming berms at the marsh edge which filters much of the available suspended sediment (Ranwell, 1964; Cahoon and Turner, 1989). Hydrologically, marsh sites nearest to the sediment source (e.g., river, diversion, etc.) record the highest rates of vertical accretion (Baumann et al. 1984; Lane et al. 2006). A mineral sediment source disruption (through alterations to the hydrologic regime) contributes to wetland loss in coastal Louisiana (Kesel, 1989; Snedden et al. 2007). Isolation from fluvial sediment inputs due to levee construction has severely limited overbank delivery and the reduction of suspended sediment loads carried by the MSR together have starved previously river-fed marshes of mineral sediments necessary to compete with RSLR (Gagliano et al. 1981; Blum and Roberts, 2009). Similar construction along the ATR and other southwestern Louisiana rivers have caused the same problems to persist across Louisiana's Chenier Plain as well (Gould and McFarlan, 1959; Hijma et al. 2017).

Vertical accretion and subsidence both contribute to surface elevation change. As described by Jankowski et al. 2017, vertical accretion and subsidence processes sum to equal a vertical surplus or deficit coefficient defined by:

$$VA_{SD} = VA - (SS + DS + SLR) \quad (1)$$

where VA_{SD} is the vertical accretion surplus or deficit, VA is vertical accretion, SS is shallow subsidence, DS is deep subsidence, and SLR is geocentric sea level rise.

Ultimately, VA_{SD} determines the overall success of a marsh facing submergence, as net

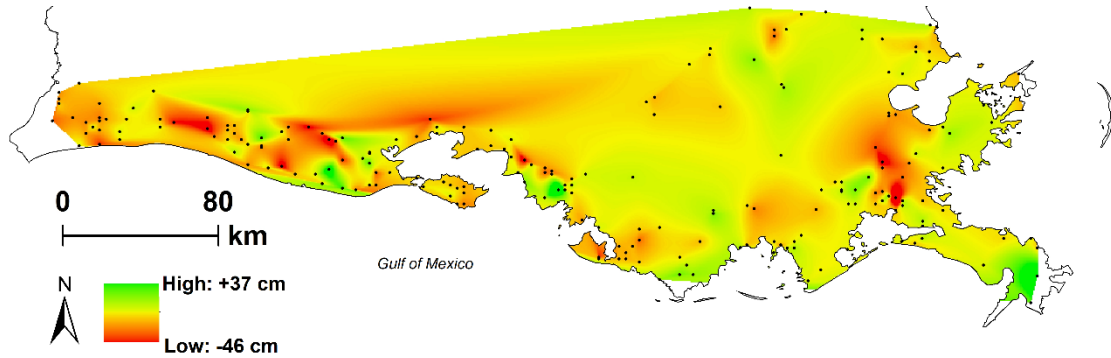


Figure 4. Geostatistical interpolation (kriging) of vertical accretion surplus/deficit (VA_{SD}) data derived from 274 CRMS stations (Jankowski et al. 2017) in coastal Louisiana. CRMS stations are represented by black dots.

accretion must outpace RSLR (= SS + DS + SLR) to maintain subaerial status

(Jankowski et al. 2017). VA_{SD} varies across the state with little spatial trend (Figure 4).

2.4 Marsh Terracing

One potential lower-cost alternative for coastal restoration of marshes that has gained popularity across Louisiana since its inception in the late 1980s is known as marsh terracing. Most terracing projects are accomplished for between a few hundred thousand and few million US dollars, making them significantly cheaper and more accessible for smaller government and non-government entities than large-scale projects that cost several million to a billion or more US dollars (Rozas et al. 2005). Marsh terracing is the construction of discontinuous linear segments (marsh terraces) in enclosed or partially enclosed water bodies, generally in areas that have recently converted from land to open water, as a method of coastal restoration (Figure 5; O’Connell and Nyman, 2010; Osario and Linhoss 2020). Marsh terraces are built by excavating *in situ* subtidal substrate and placing that material into a ridge until it reaches approximately the same elevation as the surrounding natural marsh to allow for periodic inundation (Brasher, 2015). Excavation



Figure 5. Google Earth satellite images of the three predominant marsh terraces designs (geometries) utilized in coastal Louisiana. Image (A) are linear terraces in Teal Pond, LA. Image (B) are grid terraces (top) and chevron (i.e., duck-wing) terraces (bottom) in Starks North Canal, LA.

is typically done by an excavator towed to the site on a floating barge or driven to the site on tracked treads. This process also creates a series of excavation pits (referred to as borrow pits) adjacent to the constructed marsh terrace. Marsh terrace construction projects typically require 3 to 6 months to construct because the first level of excavated material, which is generally composed of relatively high porosity muds, must be left to consolidate before additional material is added to reach the desired elevation. Following construction and consolidation, vegetation sprigs (plugs) are planted around the perimeter of the terrace in many terrace sites to accelerate marsh colonization with the desired species (Figure 6). Given the additional cost associated with complete terrace planting and studies that suggest plants like *Spartina alterniflora* is capable of colonizing inward quickly (Proffitt et al. 2003; Xiao et al. 2010), more recent projects have not planted sprigs beyond the marsh terrace perimeter.



Figure 6. *Vegetation sprigs of *Spartina alterniflora* planted along a grid terrace shoreline at Bayou Monnaie, one of the three field sites of in the present study. The image was taken in February 2018, and the terraces were constructed in August 2015.*

While each terrace ridge or segment individually is generally linear, they tend to be assembled into three predominate shapes in a field made of multiple segments: linear, grid, and chevron (Figure 7). Existing terrace fields tend to utilize the same shape throughout the site, but terrace compass orientation can vary. Most sites feature similarly shaped terraces oriented to line the existing natural marsh shoreline, expand the entire water body, or as their own entity clustered toward the center of the water body. Some sites place multiple shapes within one field or across multiple fields (Figure 7). With little existing research to aid in the optimization of terrace shape or orientation (Rozas and Milleno, 2007), the final designs of projects constructed to date are at the discretion of the project engineers.

Although widely utilized across the entire Louisiana coast, with 115 identified terrace sites distributed from the Texas border to the Mississippi Deltaic Plain between 1990 and 2017 (Figure 8), there have been relatively few research studies dedicated to the

proposed benefits of marsh terracing, with the majority focusing on the ecological benefits of terraces (Brasher, 2015). The proposed ecological benefits include increased marsh edge habitat, promote primary productivity, improve habitat quality, enhance nekton and waterbird presence, and the reduction of turbidity to increase light penetration and encourage SAV growth (Steyer, 1993; Brasher, 2015). Of the proposed ecological benefits, most studies to date have focused on nekton abundance and biomass as well as habitat quality (Rozas and Milleno, 2001; Bush Thom et al. 2004; Rozas and Milleno, 2007; Rozas and Milleno, 2009; Brasher, 2015). This research shows



Figure 7. Google Earth satellite images of examples of the distribution of terraces in fields in projects carried out in coastal Louisiana. A) Linear terraces constructed in 2014 in Lake Tom on Marsh Island proximal to the shoreline and hydrological outlet of the lake. B) Grid terraces constructed in 2005 at Bay Alexis in the center of the bay. C) Linear terraces constructed in unnamed pond in 2015 south of Larose, LA that stretch across the entire water body.

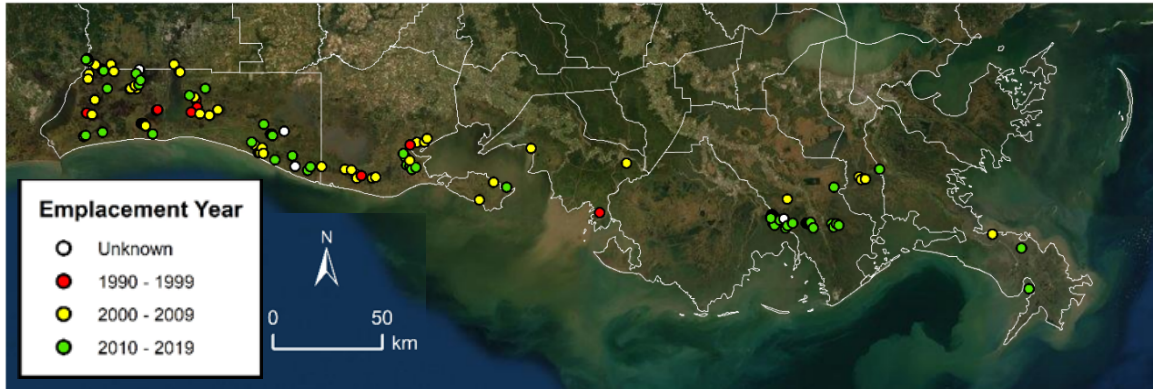


Figure 8. Marsh terrace project sites constructed up to 2019 in coastal Louisiana grouped by year the project was constructed.

that terraced sites are capable of producing higher nekton abundance and biomass than reference sites, but not for all species (Rozas and Milleno, 2001; Rozas and Milleno, 2007). When using nekton as a proxy for habitat quality, terraced sites show increased habitat quality as compared to a pre-restoration conditions proxy open-water environment (Bush Thom et al. 2004). Terraced sites neither outperformed reference sites in all categories nor did they prove to be functionally equivalent to reference sites when species distributions were compared, but terraced sites did tend to provide more suitable habitat conditions and produce higher nekton use than areas with pre-restoration conditions (Rozas and Milleno, 2001; Bush Thom et al. 2004; La Peyre et al. 2007; Rozas and Milleno, 2007).

Studies regarding turbidity reduction and increased SAV growth around terrace fields have showed little to no significant differences in turbidity between terrace and reference sites, though the few instances of notably different turbidities favored the terraced sites (Rozas and Milleno, 2001; Cannaday, 2006; La Peyre et al. 2007; O’Connell and Nyman, 2010). The primary study regarding terrace effects on waterbirds (O’Connell and Nyman, 2010, 2011) was disrupted by Category 5 Hurricane Rita in

September 2005, which split the intended year-long study and limited data availability (Brasher, 2015). O'Connell and Nyman (2010, 2011) found terraced sites had greater waterbird abundance and species richness, both of which were attributed to the greater marsh edge habitat at the terraced site. While terraced sites have not proven themselves significantly superior to reference sites ecologically, they do appear to function similarly to yield a comparable, viable environment. This, coupled with terraced sites apparent superiority to pre-restoration sites (Brasher, 2015), have provided motivation to continue their construction and to continue investigation into marsh terracing and its proposed benefits.

Far less documented but equally as important as ecological benefits are the morphological benefits of marsh terracing. These potential benefits include an increase in marsh edge, creation of emergent marsh area, reduction in bounding shoreline erosion, and enhanced sediment trapping and deposition in and around the terrace field. These can be further divided as immediate or gradual benefits. Immediate benefits are those available immediately following construction completion, such as the additional (planted) marsh area and the additional marsh edge created at the site. Once ridge construction is complete, terraces should immediately begin intercepting fetch-driven waves or interrupting the tidal-meteorological current field that would otherwise impact the natural marsh shoreline bounding the water body or marsh fragments remaining within the water body. The few existing morphological studies have shown terraces help reduce erosion or increase aggradation and impact shoreline change (Steyer, 1993; McGinnis and Guidry, 2011), but these studies were limited by smaller sample sizes. The creation of emergent marsh is a more gradual benefit and develops initially as the vegetation

colonizes the terrace, and then, later as submerged areas within a terrace field potentially elevate due to sediment retention until it becomes emergent and marsh grasses colonize. Rapid colonization of terraces by marsh vegetation has been widely observed by field observations, experimentation, and remote sensing analyses (Steyer, 1993; Turner and Streever, 2002; Castellanos and Aucoin, 2004; Nyman and Chabreck, 2012; Brasher, 2015). Improved sediment trapping and increased deposition are thought to take place within terrace fields because the terraces disrupt and slow flow velocities, allowing for material to fall out of suspension, or due to the increased presence of vegetation and SAV, where increased stem density leads to increased deposition when material is available (Friedrichs and Perry, 2001). Assessing deposition in Louisiana terrace fields and around those terraces while excluding the bounding shoreline has indicated as many as 55% of terrace fields are depositional, while the remaining 45% appear erosional (Osorio et al. 2020).

While there are promising results regarding the morphological effects of marsh terracing (Osorio et al. 2020; McGinnis and Guidry, 2011; Castellanos and Aucion, 2004; Steyer, 1993), the scarcity of research leaves many knowledge gaps that this current study was designed to address. Previously, no studies quantified deposition rates within terrace fields and accretion rates on terraces across multiple study sites. Existing research typically assessed deposition within single terrace fields or between projects in close proximity (Steyer, 1993). Additionally, the existing geospatial analysis is limited as it excludes changes along the bounding marsh shoreline (Osorio and Linhoss, 2020). Without this component, terrace efficacy regarding shoreline erosion cannot be interpreted. Osorio and Linhoss (2020) also did not assess changes prior to terrace

construction, which is necessary to determine whether terrace presence encouraged the observed depositional trends or if favorable (depositional) processes were already active in the basins studied. The current study improves upon this existing geospatial analysis by measuring changes along bounding marsh shoreline and assessing basin change prior to terrace construction to isolate and analyze the impact of terrace presence. Further, the current study performs the first numerical modeling effort to illustrate the hydrodynamics within and around terrace fields of varying geometries. The models presented herein also serve to verify the presumed impacts of terraces on water velocities and total bed shear stress values, which can be used to predict sediment dynamics within and around terraces fields as well as guide future modeling efforts.

3. Methods

3.1 Field Methods

Nine field campaigns involving boat and on foot, marsh-based efforts were conducted between February 19, 2018 and May 21, 2020 across three study sites in coastal Louisiana (Figure 9) to investigate the sedimentary characteristics of subaerial marsh terraces and surrounding, subaqueous terrace field substrates as well as the sediment dynamics within the terrace fields.

3.1.1 Site Selection

Approximately 17% of marsh terracing sites in Louisiana are located in the state's Mississippi-Atchafalaya deltaic plain region (Osario and Linhoss, 2020). Within the sites located in this region, three study sites were selected based on varying degrees of

hydrologic connectivity to upland riverine sources, predominant sediment delivery mechanisms, and terrace construction date (Figure 9). When sites were selected in early 2018, terrace fields less than one year old were eliminated from consideration. Although terraces are proposed to provide immediate benefits (e.g., increased marsh edge habitat, erosive wave interruption; Brasher 2015), the field studies were designed to investigate more gradual benefits (e.g., increased deposition), and therefore, older, more established terraces were prioritized.

The Bayou Monnaie study site in the Terrebonne Basin (Figure 10) was selected for its intermediate hydrologic connectivity to upland or bay water sources (i.e., water exchange through narrow canals and natural bayous) and presumed intermediate riverine-

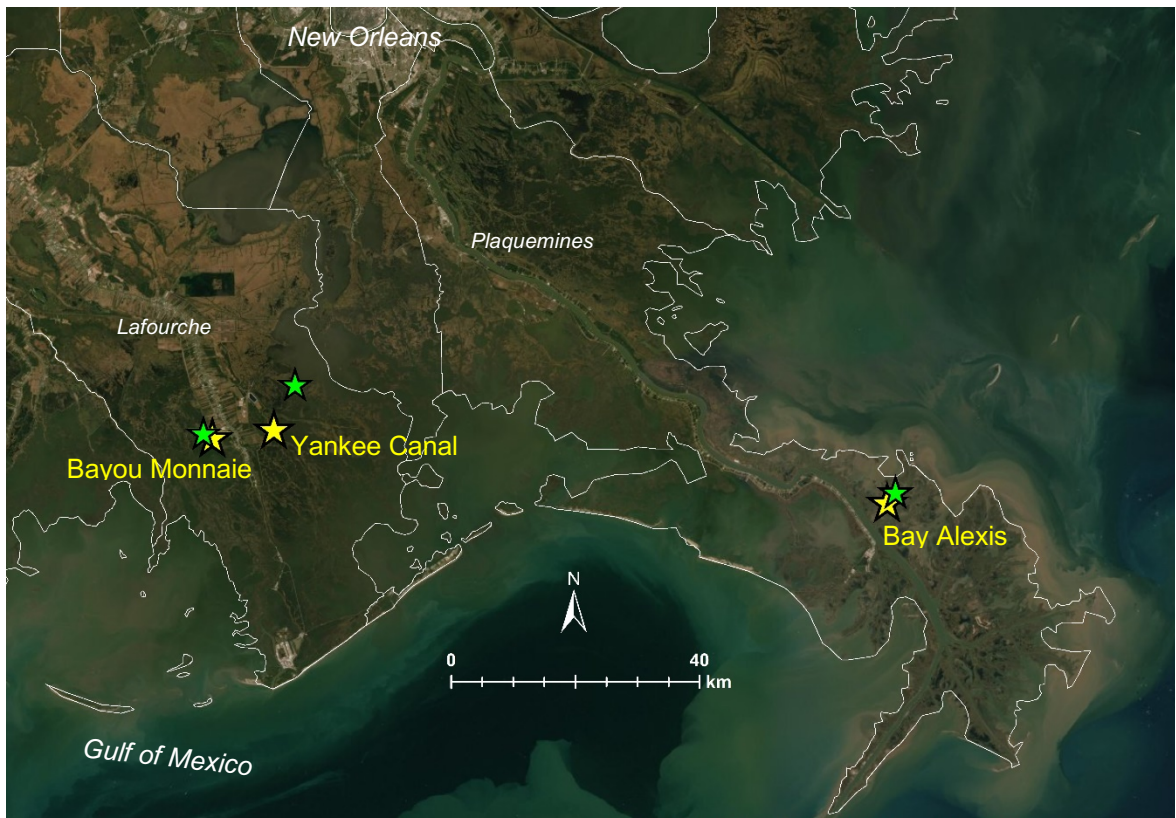


Figure 9. Field sites (yellow) and the closest CRMS station (green) occupied for the present study. From West to East, the sites are Bayou Monnaie (CRMS 0387), Yankee Canal (CRMS 6303), and Bay Alexis (CRMS 2614).

bay sediment supply given its proximity to Catfish Lake. Bayou Monnaie was accessed prior to and during the construction of a new terrace field to the North of the selected study site (Figure 10). Although the field sampling did not occur in this region, the exploratory visits provided essential insights into terrace building procedures at the site.

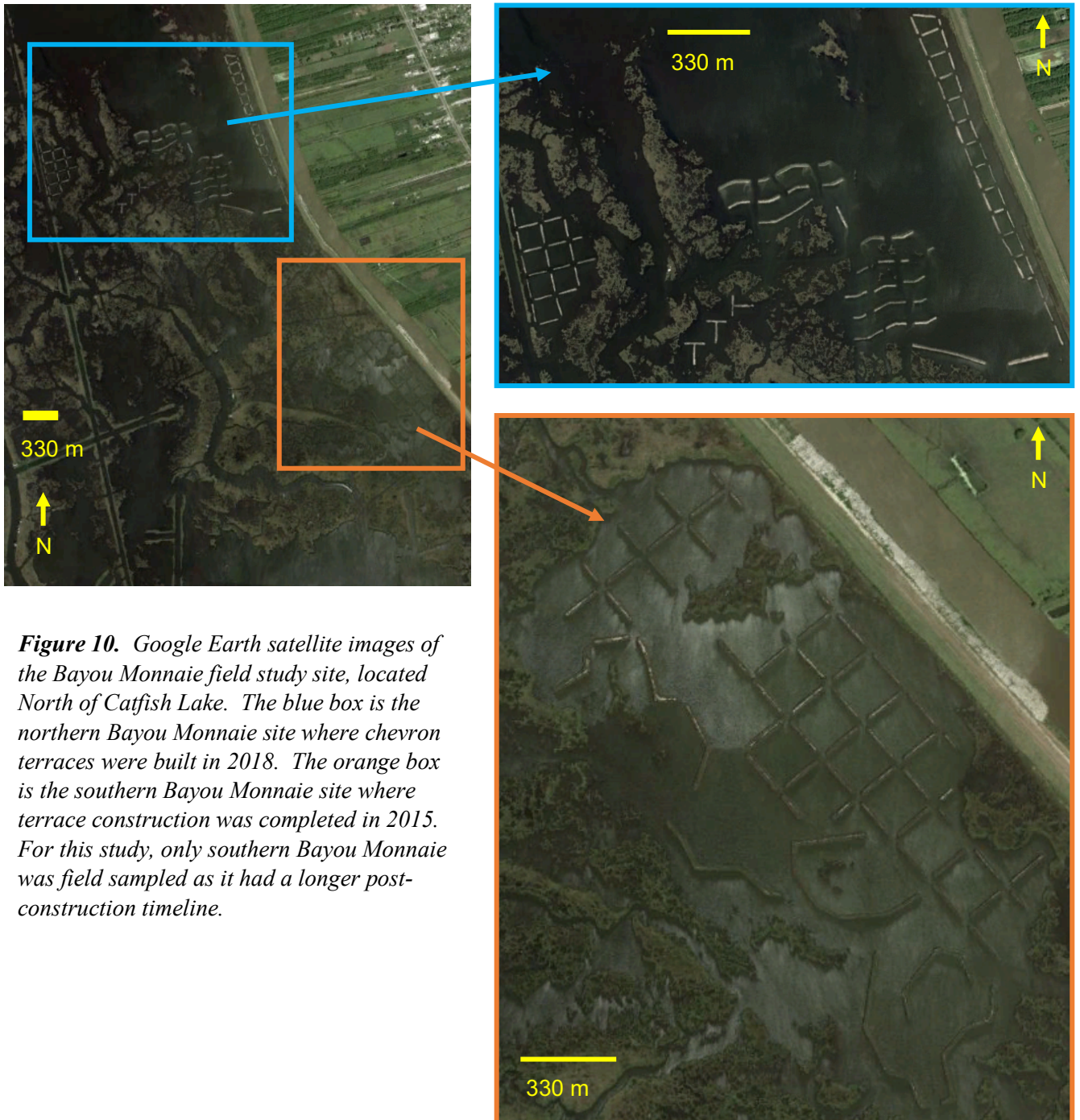


Figure 10. Google Earth satellite images of the Bayou Monnaie field study site, located North of Catfish Lake. The blue box is the northern Bayou Monnaie site where chevron terraces were built in 2018. The orange box is the southern Bayou Monnaie site where terrace construction was completed in 2015. For this study, only southern Bayou Monnaie was field sampled as it had a longer post-construction timeline.

The selected study field at Bayou Monnaie is predominantly composed of grid terraces and some linear or semi-linear terraces (Figure 10). These terraces range in length depending on shape but the single largest terrace is a non-linear 325 m. Average terrace length at Bayou Monnaie is 80 m and width is consistently at or near 10 m for all terraces regardless of shape. To complete the construction in 2015, vegetation plugs of *S. alterniflora* were planted along the edge of the terrace, leaving the center and apex of the ridge bare to await inward colonization (Ducks Unlimited, unpublished data, 2015).

The second field site, Yankee Canal, is located approximately 8 km northeast of Bayou Monnaie across Bayou Lafourche in Barataria Basin. Yankee Canal was selected as a site with intermediate hydrological connectivity and presumed intermediate river-bay sediment supply as well (Figure 11). The study site includes two terrace fields, which are termed North and South for their geographic relation to one another. Both North and South Yankee Canal terrace fields are composed of chevron terraces which tend to exceed 160m in length. Similar to Bayou Monnaie, the terraces are generally 10 to 12 m wide; however, some terraces in the South have thinned to 5 to 7 m in width of vegetation since constructed. Completed in 2015, the Yankee Canal terraces were also planted with *S. alterniflora* plugs around terrace perimeters to support inward vegetation expansion.

The third field site, Bay Alexis (i.e., Alexis Bay), is located on the east bank of the MSR near a large distributary channel Baptiste Collette. Bay Alexis was selected for its high-level of hydrologic connectivity and presumed high riverine sediment supply because it is connected to the MSR system through channels connected to Baptiste Collette and other small channels directly leading from the MSR (Figure 12). Based on



Figure 11. Close-up Google Earth satellite image of Yankee Canal field study site. Northern Yankee Canal and southern Yankee Canal were both sampled during this study.

the location, the sediment supply (and to a certain extent water level) at Bay Alexis is likely controlled by the riverine source and some tidal influxes. Here, there are two terrace fields, referred to as the Old and New fields. The old field includes a few surviving grid terraces that were constructed in early 2005 and subsequently damaged by Hurricane Katrina in August of the same year (FEMA, 2015). The Old field was originally 870 x 610 m and was composed of 70 individual grid terraces (7 terraces wide, 10 terraces long) located near the center of Bay Alexis. As of site selection in early 2018, the remnants of approximately 20 individual terraces can be recognized in satellite imagery (Figure 12). The New field refers to the grid terraces constructed adjacent to the Old field in 2015. The New field was constructed following a vote by Plaquemines



Figure 12. Google Earth 2019 satellite image of the Bay Alexis field study site. The degraded subaerial terraces shown on the left are remnants of the first terracing project in Bay Alexis completed in 2005, shortly before they were damaged by Hurricane Katrina. The more recent grid terrace field was constructed in 2015, which were funded by FEMA. The original extent of the 2005 field is illustrated by the yellow box.

Parish to replace rather than restore the old field terraces. In the New field, there are approximately 55 complete (i.e., enclosed) and incomplete (i.e., three or fewer sided) grid terraces, and they were placed between the Old field and the marsh edges of Bay Alexis. Both the Old and New fields were constructed like Bayou Monnaie, with a marsh excavator located at a central point in each grid square where it excavated subtidal substrate and placed the material into terrace ridges (Dan Dehon, P.E., personal communication, 2018). Terraces in both fields were 70 m long and 15 m wide. As at Bayou Monnaie and Yankee Canal, vegetation plugs were planted around the external perimeter of the terraces. Within one year of their completion (2016), vegetation had covered or nearly covered every terrace in the new field in satellite imagery.

3.1.2 Sediment Sampling

Sediment cores were obtained working from two Tulane University Bywater Institute vessels: R/V *Mudskipper* and R/V *Shelley Meaux*. Short (<50 cm long) sediment cores were collected from submerged areas of the terrace using an Aquatic Research Instruments Icelandic piston corer to determine sedimentological properties of the substrate and to differentiate between pre- and post-construction sediment. Cores were collected in acrylic 6.67 cm inner-diameter tubes and were sealed onsite with overlying water for same day return to Tulane laboratories in New Orleans. Nine cores were collected along 3 transects (i.e., 3 cores per transect) at each study site. At Bayou Monnaie and Bay Alexis, each transect consisted of 2 cores from each subaqueous borrow pit and one core from the unexcavated central pond platform between two terraces where the excavator was located during the construction (Figure 13). At Yankee

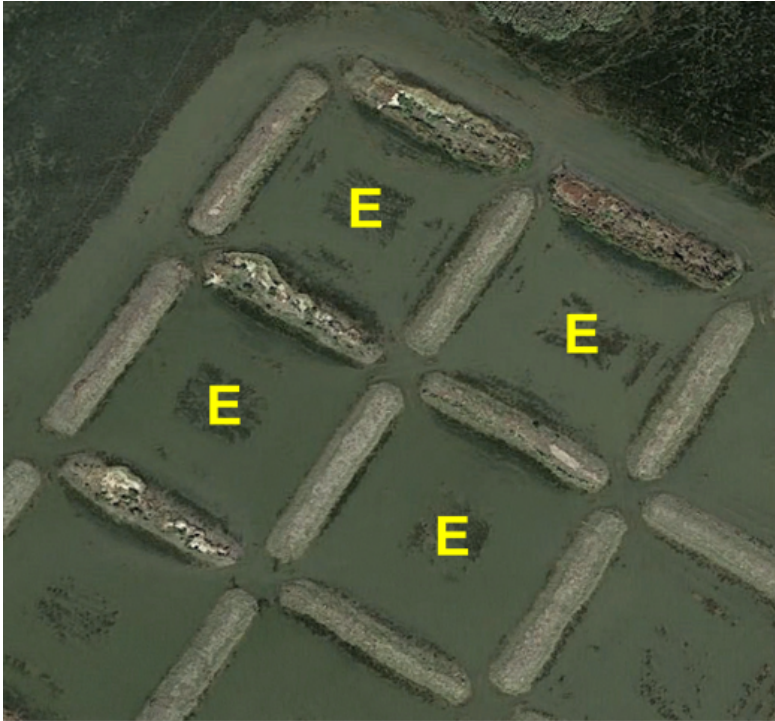


Figure 13. Google Earth 2019 satellite image of the Bay Alexis marsh terrace grids showing the location that the excavator was placed during terrace construction. The result was that a central high was left post-construction surrounded by excavation (borrow) pits (deep areas) where material was excavated to construct the adjacent terraces.

Canal, the bathymetry differed, and each terrace had a single borrow pit, which ran the length of the terrace and sat approximately 10 m from the terrace edge. This bathymetry suggests the excavator may have been located at either end of the terrace for construction. Adjusted to the unique bathymetry of a single borrow pit, transects at Yankee Canal were composed of 2 cores on either side of the borrow pit and 1 core at the pit's center. Core sites were selected based on the deepest bathymetry mapped at each site; the deepest borrow pit was identified and a transect was drawn between the two adjacent terraces. Core elevations were either measured relative to the water level obtained from nearby Coastal Reference Monitoring System (CRMS) stations at the time of their collection or measured using survey instruments (Figure 9; see §3.1.4 Elevation Measurements).

To characterize the sediment on the subaerial marsh terraces themselves and any material that accumulated post-construction, additional sediment cores were collected using an Eijkelkamp 5-cm diameter peat auger or a PVC pushcore (6.67 cm diameter).

Four auger cores and six pushcores were collected from Bayou Monnaie, 11 pushcores were collected from Bay Alexis, and nine pushcores were collected from Yankee Canal. All but the four auger cores at Bayou Monnaie were returned to the Tulane River-Coastal Center (TRCC) in New Orleans for extrusion and further laboratory analysis. Those four cores were examined in the field and 2 cm interval samples from each visually distinct layer were retained for further laboratory analysis (Figure 14). Neither cores collected along transects between terraces nor cores collected on subaerial terraces displayed evidence of compaction or alteration during sampling.



Figure 14. Peat auger core collected from the Bayou Monnaie study site. The interval shown was is from a depth of 100 cm to 140 cm. These cores were described in the field and subsampled at 2 cm intervals for return to the laboratory for analysis.

3.1.3 Feldspar Marker Horizons

Deposition rates on the marsh terraces at Bayou Monnaie and Yankee Canal were quantified using feldspar marker horizons (FMH), utilizing the methods of Cahoon & Turner (1989). At Bayou Monnaie, 46 FMHs were deployed along 3 subaerial terraces. At Yankee Canal, 18 FMHs were deployed along six terraces equally divided between the North and South fields. To deploy each FMH, a thin layer (<1 cm) of feldspar was sprinkled into a 10.8 cm-diameter PVC ring laid on the terrace surface, which created a 183.85 cm² plot (Figure 15). The FMHs were in place at Bayou Monnaie on February 4, 2020 and were visited again for measurement on April 15, 2020: placement and

measurement at Yankee Canal was conducted on March 10, 2020 and May 21, 2020, respectively. For determination of sediment thickness of each FMH and recovery of sediment for laboratory analysis, each flagged plot was cored using an Oakfield compact soil probe (2.38 cm inner diameter). After core removal, thickness of the sediment atop the white marker layer was measured with a metric ruler (mm) and subsamples of the overlying material were carefully collected with a spatula and placed into a labeled



Figure 15. Feldspar marker horizon (FMH) plots. FMH plots were deployed on the subaerial portions of the terraces using a 10.8 cm diameter PVC ring laid on the terrace surface resulting in a thin layer (< 1 cm thick) plot with 183.85 cm² surface area.

WhirlPak bag. The retrieved FMH samples were returned to TRCC laboratories for analysis.

3.1.4 Elevation Measurements

Elevation measurements for the core and FMH plot locations at the three study sites were made with either a Trimble R8 Real-Time Kinematic (RTK) global positioning

system (GPS) or a theodolite surveying system working from an initial GPS point. The RTK system was used to measure elevation of cores taken during the 2018 field season at Bayou Monnaie and Bay Alexis. The theodolite system was utilized at Bayou Monnaie and Yankee Canal to determine the elevation of each FMH site.

The RTK system measured the water surface elevation at the start of coring a transect between terraces. To provide high precision position and elevation data, the Geospatial Position System (GPS) antenna of the RTK system received real-time correction factors via mobile internet through the Louisiana State University (LSU) Center for Geoinformatics (C4G) network. This antenna was placed atop a 2m leveled survey pole during measurements, which were taken at the sediment surface for terrestrial samples and at the water surface for submerged sampling. Elevation of the subaqueous core sites was then obtained by measuring site water depth with a stadia rod. RTK-GPS survey points were collected at a location by continuously recording position and elevation (Trimble Access "topo-point" method) until 5 seconds of sufficiently accurate data (± 3.05 cm x, y, z location) had been collected. The horizontal datum of the survey was Universal Transverse Mercator (UTM) Zone 15N in the North American Datum of 1983 (NAD83). The vertical datum was the North American Vertical Datum of 1988 (NAVD88) and was calculated referencing the 2012a Geoid (Geoid12A) where horizontal and vertical units are measured in meters.

The theodolite surveying method provides elevation data at an accuracy of about ± 1 cm at the distances surveyed (< 100 m). A WAAS-GPS unit was utilized to measure the latitude and longitude of the theodolite when it was initially positioned. Using measurements of height of the optical telescope and the elevation of the water surface by

positioning the stadia rod at the shoreline at the beginning and end of each tripod location measurement series, individual FMH locations were measured using the stadia rod.

Relative elevation and distance was determined for each using the theodolite compass line of sight and trigonometric offset on the rod. Relative elevations were then converted to NAVD88 vertical datum using mean water elevation during the measurement period at a nearby CRMS water level gage (Figure 9). Each of the three field sites has an active CRMS stations within 6.5 km of the terrace field (Bayou Monnaie to CRMS 0387 = 0.97 km; Yankee Canal to CRMS 6303 = 6.5 km; Bay Alexis to CRMS 2614 = 1.7 km).

3.1.5 Bathymetric Mapping

To illustrate the evolution of the bathymetry within terrace fields, bathymetric maps were produced for representative sample regions within each study site. A Garmin echoMAP single beam fathometer with CHRIP 74dv transducer were affixed to the *R/V Mudskipper* for mapping at Bayou Monnaie and Yankee Canal, and to a pirogue at the shallow Bay Alexis site. The vessel maneuvered through each terrace by running as close alongside a terrace shoreline as possible until the outer border of the pond was mapped. The vessel then moved progressively farther out from the terrace shoreline and repeated this path until it reached the center of the pond. Then, the vessel was maneuvered diagonally across the terrace field to create an “X” with the tracklines shown on the Garmin screen to complete the mapping within a single terrace. Depths were corrected for water level elevation to NAVD88 using the same CRMS water level gage as for the FMH elevation mapping for each site.

3.2 Laboratory Methods

3.2.1 Core Processing

Each core collected in the field was returned to TRCC's laboratories for further analysis. Stratigraphic characteristics were recorded for each interval during extrusion, and estimated stratigraphic boundaries were measured as well. Piston and push cores were vertically extruded and subsampled at 1 cm intervals for the first 0-10 cm of each core. Starting at 11 cm, every other 1 cm interval (e.g., 11-12 cm, 13-14 cm, etc.) was subsampled. Auger cores were subsampled into 2 cm increments starting at the top of each described sedimentary facies interface. These intervals were placed in pre-weighed WhirlPaks to determine the wet weight of each sample. For each sample interval, organic matter content and grain size was estimated during core description. These parameters were later analyzed quantitatively in the laboratory.

3.2.1.1 Bulk Properties & Sedimentary Facies

Core samples were weighed to determine wet weight and then freeze-dried to determine dry weight and preserve the organic fraction for further analysis. Due to the nature of their collection, FMH samples were smaller than core samples and were not freeze-dried. Instead, FMH samples were heated in an oven to 60°C for 24 hours to determine their dry weights.

From water content (wet – dry weight), downcore porosity was calculated by assuming a sediment mineral grain density of 2.65g/cm³ when loss on ignition (LOI) data was not available. Results were calculated as a function of saturated bulk density:

$$Porosity = 1 - \left(\frac{SBD - 1.01}{2.65} \right) \quad (2)$$

where SBD is saturated bulk density (g/cm^3), $1.01 \text{ g}/\text{cm}^3$ is the density of water, and $2.65 \text{ g}/\text{cm}^3$ is the density of quartz. As derived by the function above, porosity is a dimensionless value. Where LOI data was available to determine organic content, the differing density of organic matter was taken into consideration in calculating porosity. LOI was determined by the percent change in weight after the freeze-dried sample was heated to 550°C for 14 hours in a small laboratory furnace. Using saturated bulk density calculated from the above, porosity corrected for organic content was determined using:

$$Porosity_{corr} = 1 - \left(\left(\frac{SBD - 1.01 \text{ g cm}^{-3}}{2.65 \times (1 - LOI)} \right) + 1.24 \text{ g cm}^{-3} \times LOI \right) \quad (3)$$

where S_{BD} is saturated bulk density, $1.01 \text{ g}/\text{cm}^3$ is water density, $2.65 \text{ g}/\text{cm}^3$ is the assumed sediment mineral grain density, $1.24 \text{ g}/\text{cm}^3$ is the assumed organic material density, and LOI is the decimal fractional loss on ignition.

For samples of known volume (e.g., core samples of fixed diameter where samples fully filled the volume), saturated bulk density was calculated by dividing the wet weight by the volume of the sample. Similarly, dry bulk density was calculated by dividing the dry weight by the volume of the sample. For samples of unknown volume (e.g., incomplete FMH retrievals), dry bulk density (mass dry sediment/volume wet sediment) was calculated by:

$$\rho = \frac{1 - W}{\frac{W}{\rho_w} + \frac{1 - W}{\rho_s}} \quad (4)$$

where ρ is the dry bulk density, W is water content, ρ_w is water density (g/cm^3), ρ_s is sediment mineral grain density, which is determined by:

$$\rho_s = 1 - \text{LOI} * 2.65 \text{ g cm}^{-3} + \text{LOI} * 1.24 \text{ g cm}^{-3} \quad (5)$$

where 2.65 g/cm^3 and 1.24 g/cm^3 are the assumed densities of mineral and organic sediments, respectively (Kolker et al. 2009).

Sedimentary (mud) facies were defined using organic content derived from LOI and porosity values determined from Equation 2. High porosity muds are defined as facies where $\Phi \geq 0.8 \pm 0.1$. For defining facies based on organic content, Organic-rich Mud facies was defined where LOI values were $\geq 0.2 \pm 0.1$. Facies were defined as True Peat when organic content values exceed 75% (Kosters et al. 1989; Wilson and Allison, 2008). These parameter distinctions are based on ranges reported by Wilson and Allison (2008) for sedimentary facies found in the upper 200 cm of cores collected across southeastern Louisiana. For the definitions of facies based on porosity (high versus low porosity muds), the boundary (80%) was based on values reported by Wilson and Allison (2008) that range from 56.2 to 83.6. Average organic content (%) reported by Wilson and Allison, (2008) from the same dataset range from 4.6 to 31.8, which led to the selection of 20% organic content to define the boundary of the Organic-rich Mud facies.

3.2.1.2 Granulometry

Grain size analysis (D_{10} , D_{50} , D_{90} , etc.) was completed for selected post-LOI samples using a Malvern Mastersizer 3000 laser diffraction grain size analysis system with a HydroEV dispersion unit. Prior to analysis, samples were sonicated for at least 1 h with 20 mL of 0.1% sodium metaphosphate solution for 24 h to ensure the sample was completely disaggregated. Then, a sample was added until a laser obscuration between

8% and 20% was reached. The mixture was further sonicated using the HydroEV ultrasound for 90 seconds at 30% power before measuring the grain size distribution. Each grain size distribution is an average of three measurements. Each measurement is a combination of two 15 second measurements, one with a laser of 632.8 nm wavelength and one with a laser of 470 nm wavelength.

3.2.1.3 Radioisotope Analysis

Sediment deposition rates at Bay Alexis were evaluated by analyzing eleven cores for the particle-reactive, naturally-occurring radiotracer Beryllium-7 (^7Be , half-life 53 d), which is produced in the Earth's atmosphere through the spallation of oxygen (O) or nitrogen (N) atoms and enters the terrestrial system through precipitation or dry deposition (Sommerfield et al. 1999). Riverine clay-sized particles tend to be enriched in ^7Be due to the focusing of a large collection area and their relatively reactive negative charge, respectively (Allison et al. 2005). Given its delivery mechanisms and short half-life ($t_{1/2} = 53.1$ days), ^7Be can be used to trace seasonal sediment dynamics, such as deposition derived from seasonal MR flooding that is presumed present at Bay Alexis. Due to its half-life, 87.5% of measured ^7Be activity can be ascribed to sediment deposition from the 159 days preceding collection (06 December 2019 to 13 May 2020; Kolker et al. 2012). Four cores from the Bayou Monnaie study site collected on 02/18/2018 were also analyzed for ^7Be but no activity was observed in any sites, presumably due to the low mineral content of stored sediments (particle-reactive tracers such as ^7Be tend to be adsorbed onto clay mineral surfaces; Allison et al. 2005; Taylor et al. 2012; Taylor et al. 2013).

To conduct the analysis, aliquots of oven-dried sediment samples from Bay Alexis cores were ground in a mortar and pestle to disaggregate and packed into vials or petri dishes for radioisotope analysis using Canberra Low-Energy Germanium (LEGe) gamma spectrometers. Samples in vials were run on well-configured detectors and samples in petri dishes were run on planar-configured detectors, and all samples were processed for at least 24 hours. The top (shallowest) interval (0-1cm) of a core was analyzed first with subsequent (deeper) intervals run in the following days. Given the time constraint associated with processing ^7Be , when an interval at depth showed no counts above background, the next interval was run to ensure total penetration of ^7Be had been captured. All samples were analyzed between 4 and 20 days after core collection and samples from the same core were run on a single detector. ^7Be activity (dpm/g) was calculated using net peak area of the 477 keV photopeak corrected for efficiency using the IAEA-Baltic Sea 3000 standard.

3.2.2 Geospatial (Remote Sensing) Wetland Area Analysis

3.2.2.1 Site Selection

For this aspect of the studies, the examined terrace fields in Louisiana were expanded beyond the three on-ground study sites. As of March 2020, there are approximately 115 marsh terrace fields across Louisiana (Ducks Unlimited, unpublished data) and each field was assigned a unique integer value between 1 and 115 (inclusive). A random number generator yielded an integer value used to randomly select fields for geospatial analysis. The field was then identified on the Louisiana Terrace Inventory GIS

Application and Resource (LTIGAR) database (Westphal and Nakashima, 2019). In LTIGAR, terrace fields are grouped into sites by various parameters including but not limited to: geographical proximity, construction date, and permitting agency. As each site may have one or more terrace field, there are fewer than 115 distinct sites within LTIGAR. When a randomly selected field corresponded to a site with more than one field, each field from that site was selected for analysis. Seven random integers were generated, which yielded seven different sites and 13 total fields for remote sensing analysis (Figure 16).



Figure 16. Geospatial analysis (remote sensing) terrace sites in the present study. From West to East, site numbers are: 1102 (W/E), 2015 (W/C/E), 3008, 3006 (W/E), 5001, 7001, and 7006 (N/S). Site numbers are derived from the Louisiana Terrace Inventory GIS Application & Resource (LTIGAR).

3.2.2.2 Image Acquisition

The aerial imagery used to assess shoreline change along terraced sites was obtained from the USGS EarthExplorer website (<https://earthexplorer.usgs.gov/>). USGS Digital Orthophoto Quadrangle (DOQ) images were used for dates preceding 2007 and United States Department of Agriculture (USDA) National Agriculture Imagery Program (NAIP) photographs were used for dates from 2007 and later for the image analysis.

Each aerial image was projected to the Universal Transverse Mercator (UTM) coordinate system and georeferenced to the North American Datum of 1983 (NAD83) with 1-meter resolution using ArcMap 10.4.1 from the ESRI ArcGIS suite. Available images were limited by cloud coverage, and only images with fewer than 10% cloud coverage were considered for analysis. For each site, at least four images were selected: the earliest available DOQ, the latest available NAIP, and images as close in time to before and after terrace construction as possible.

3.2.2.3 Image Processing

Site borders were manually defined, using bounding water body shorelines around the terrace fields and channels (bayous/canals) as guidelines. All images were clipped to site boundaries using the *Extract by Mask (Spatial Analyst)* tool in ArcGIS. Multiple individual aerial images were merged when terrace site borders extended beyond a single quadrangle. A supervised (Interactive Supervised) classification tool was used to classify each clipped image into four classes: marsh, vegetated mudflat, bare mudflat, and water (Figure 17). Modifying the classification methodology of Westphal and Nakashima (2019), vegetated mudflats were treated as a subclass of land and bare mudflats were treated as a subclass of water. Both vegetated and bare mudflats are intertidal features, and their extent is largely controlled by local water level. Given the temporal and spatial extent of the images, there is no readily available method to correct each image for water level at its time of acquisition; therefore, vegetated and bare mudflats are excluded from quantified analysis of change (Westphal and Nakashima, 2019). Despite their exclusion, both features are important for more qualitative assessments at each site.

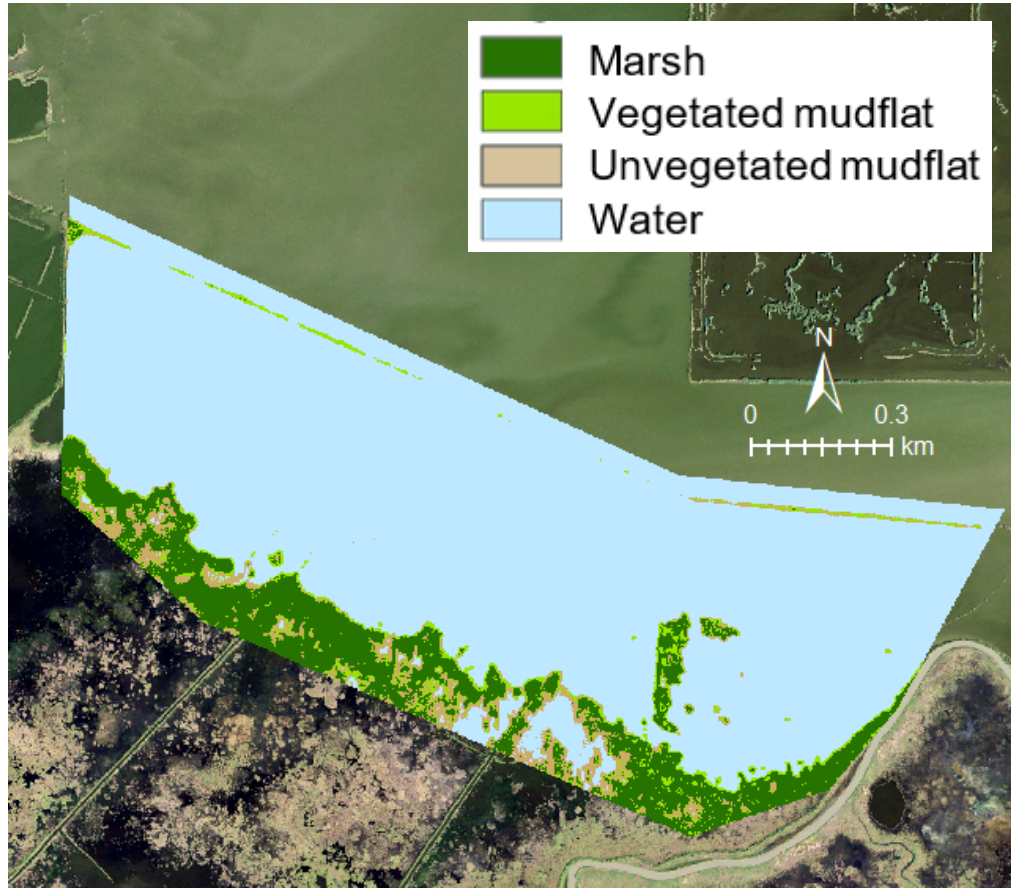


Figure 17. Representative classified image (pre-terrace construction) of a terrace site shoreline (Site 2015E) showing the four class categories (marsh, vegetated mudflat, unvegetated mudflat, water) developed for the present study.

To allow interpretation of the subtraction-produced change maps between images, each class was assigned a unique integer – land (1), vegetated mudflat (2), bare mudflat (5), and water (7). Once classified, earlier image values were subtracted from their later counterparts using the *Minus (Spatial Analyst)* tool to produce a change detection map. The earliest DOQ image was subtracted from the image immediately preceding terrace construction, and the latest NAIP image was subtracted from the image immediately following construction. The resulting maps had discrete integer values at the 1 m² pixel size ranging from (-6) to (+6), where (-6) represented water to marsh conversion (marsh gain) and (+6) indicated marsh to water conversion (marsh loss). Zero (0) represented no

change, and (-5 to -1) and (+1 to +5) represented changes into and from the vegetated and bare mudflat subclasses. The net change was quantified by adding the marsh gain and marsh loss values only. A positive sum of these values indicated net aggradation and a negative sum indicated net degradation at each site before and after terrace construction.

3.2.2.4 Classification Accuracy Assessment

To quantify the accuracy of each classification map relative to its reference image, a confusion matrix was computed using 100 stratified-random accuracy assessment points to yield a kappa index of agreement value (i.e., Cohen's kappa; Kvålseth, 1989). The stratified random sampling scheme was used to ensure each classification class had a proportional number of accuracy assessment points relative to its area. The number of accuracy assessment points exceeded 100 in every image as points were randomly generated until they were equally stratified among all four classes; most images host 116 accuracy assessment points (Figure 18).

In a generated table, each accuracy assessment point had a *Classified* and *Ground Truth* field. The *Classified* field was updated to display the value of the point derived from the classification map with integer values as described above (see §3.2.1.3). Then, the *Ground Truth* field was populated by manually inputting a value for each point based on its true value as determined by the corresponding NAIP image. A confusion matrix was computed to compare the *Classified* and *Ground Truth* fields. The resulting confusion matrix calculated errors of omission (false positives, user's accuracy, type I errors), errors of commission (false negatives, producer's accuracy, type II errors), and a kappa index of agreement. Kappa ranges from 0 to 1, where 0 indicates no agreement

between the true-color image and its classification map and 1 indicated perfect agreement between the true image and its classification map. Kappa values that exceed 0.7 are considered acceptable, while kappa values equal to or below 0.4 show low correlation between a classification and its reference (Mohammed, 2013; Ratnahparkhi et al., 2014).



Figure 18. An example of the use of 102 accuracy assessment points (yellow circles) displayed on the terrace field at 2015C. Each site features 100 to 120 stratified random accuracy assessment points to compare classification results with ground-truth values derived from the NAIP true color imagery. Sites 2015W and 2015E are also labeled.

3.3 Numerical Modeling

A numerical modeling exercise, utilizing a hypothetical marsh terrace basin, was conducted in order to examine the impact of terraces of different designs on the wind-wave-current field utilizing Delft3D software. Delft3D is an open source, finite difference modeling system developed by Deltares in the Netherlands that consists of

several integrated modules to simulate fluid flow, wave generation and propagation, sediment transport, and morphological changes (Hydraulics 2006, §1.1). Of these integrated modules, the hydrodynamic and transport simulation program Delft3D-FLOW (FLOW) has been extensively validated and used for numerous studies and applications. Delft3D-FLOW uses tidal and meteorological forcing to calculate non-steady flow and transport phenomena within a rectilinear (regular) or curvilinear (irregular) grid fitted to a defined land boundary (Hydraulics 2006; §2).

RGFGRID – another Deltares program – was used to create and modify an orthogonal, curvilinear grid for the FLOW module. Curvilinear grids allow for varied resolution throughout a grid; high-resolution can be applied to areas of interest, while lower resolution is used elsewhere to reduce computational expense. These grids can be curved to avoid artificial diffusion at non-linear boundaries and smoothed to reduce finite difference approximation errors. Coordinates within the grid system can be set as Cartesian or spherical, measured in meters and decimal degrees, respectively. The selected coordinate system is applied to all features within the grid and to any object imported into the project. To assess grid quality prior to export into FLOW, grid properties like smoothness, orthogonality, and resolution are viewed within RGFGRID (Deltares 2008, §2). The grid must be orthogonal to function within FLOW because non-orthogonal grids may require computational expensive transformation terms. Deltares recommends additional effort during grid development and model setup within RGFGRID to produce faster, more accurate computations.

3.3.1 Model Software

To illustrate sediment dynamics and circulation patterns throughout marsh terrace fields, a two-dimensional hydrodynamic and sediment model was developed using the Delft3D Flexible Mesh (FM) Suite 2020.04 HM, software version 1.5.4.45037. Additional Deltares tools that were used included the grid editor, RFGRID version 5.05.0059149, and the output visualization tool, QUICKPLOT version 2.32.59645.

3.3.2 Model Setup

To minimize numerical complexities and reduce computation expense to allow for multiple model repetitions, an idealized domain (hypothetical basin) was created using simple land boundaries. The domain is 15 km x 14.8 km with riverine and tidal inputs oriented at 180° relative to one another (Figure 19). A locally refined irregular grid (U-GRID) allowed the model to capture the effects of flow within the region of interest (i.e., extent of terrace field) while managing computation expense. Grid resolution was refined through this region of interest because it required more computation points for assessment than less dynamic areas of the domain, which remained coarse and less refined. In RFGRID, each level of refinement was produced using the *Create Rectangular Grid* operation, which ensured orthogonality was maintained throughout the grid to allow its function within FLOW. Grid nodes were manually connected within designated polygons to help transition between regions of higher and lower resolution. The final grid had 59606 elements and 57811 nodes with its finest resolution at the center (12.5 x 12.5 m grid cells). The largest grid cells (i.e., coarsest resolution) measured 200 x 200 m (Figure 20).

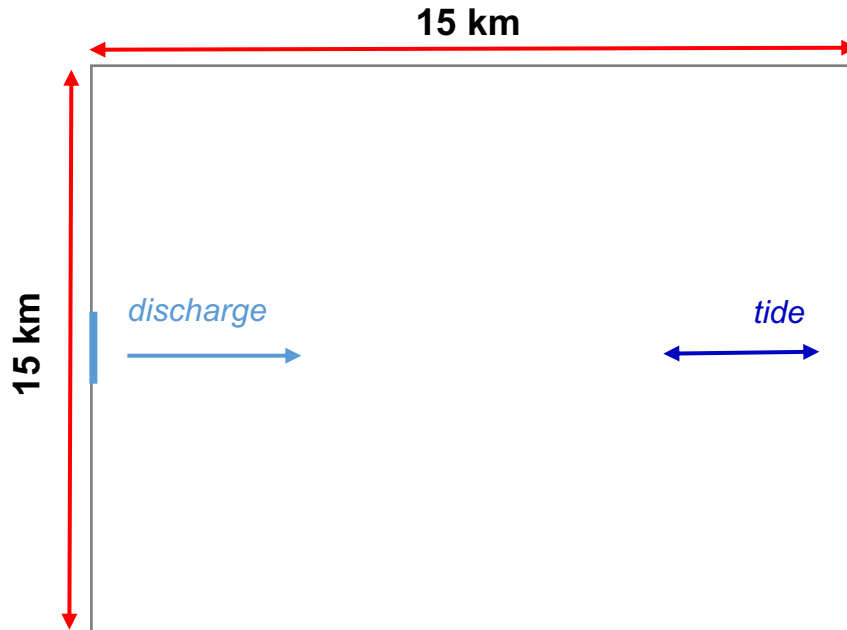


Figure 19. Simplified model domain. The domain extent is 15 x 15 km² and features two hydro-boundaries: an upstream discharge boundary and a downstream tidal boundary.

3.3.3 Bathymetry

Four bathymetries were created to reflect the three predominate terrace styles and one control. The control bathymetry was uniform with a maintained depth of -1.5 m which is an average of pre-construction water depths in terrace project sites in Louisiana. The three additional bathymetries corresponded with linear, grid, and chevron terraces, which were built by adjusting bathymetry values from the uniform -1.5 m to depths representative of terrace ridges (+0.5 m) and borrow pits (which varied in depth by terrace shape). Bathymetric contours were enumerated with XY coordinates (Figure 21A) and imported into the project, where they were interpolated onto the grid using the *Triangulation* method (Figure 21B).

Each terrace field file was developed in a spreadsheet, which determined the location of each terrace ridge relative to a starting coordinate and the necessary depth for

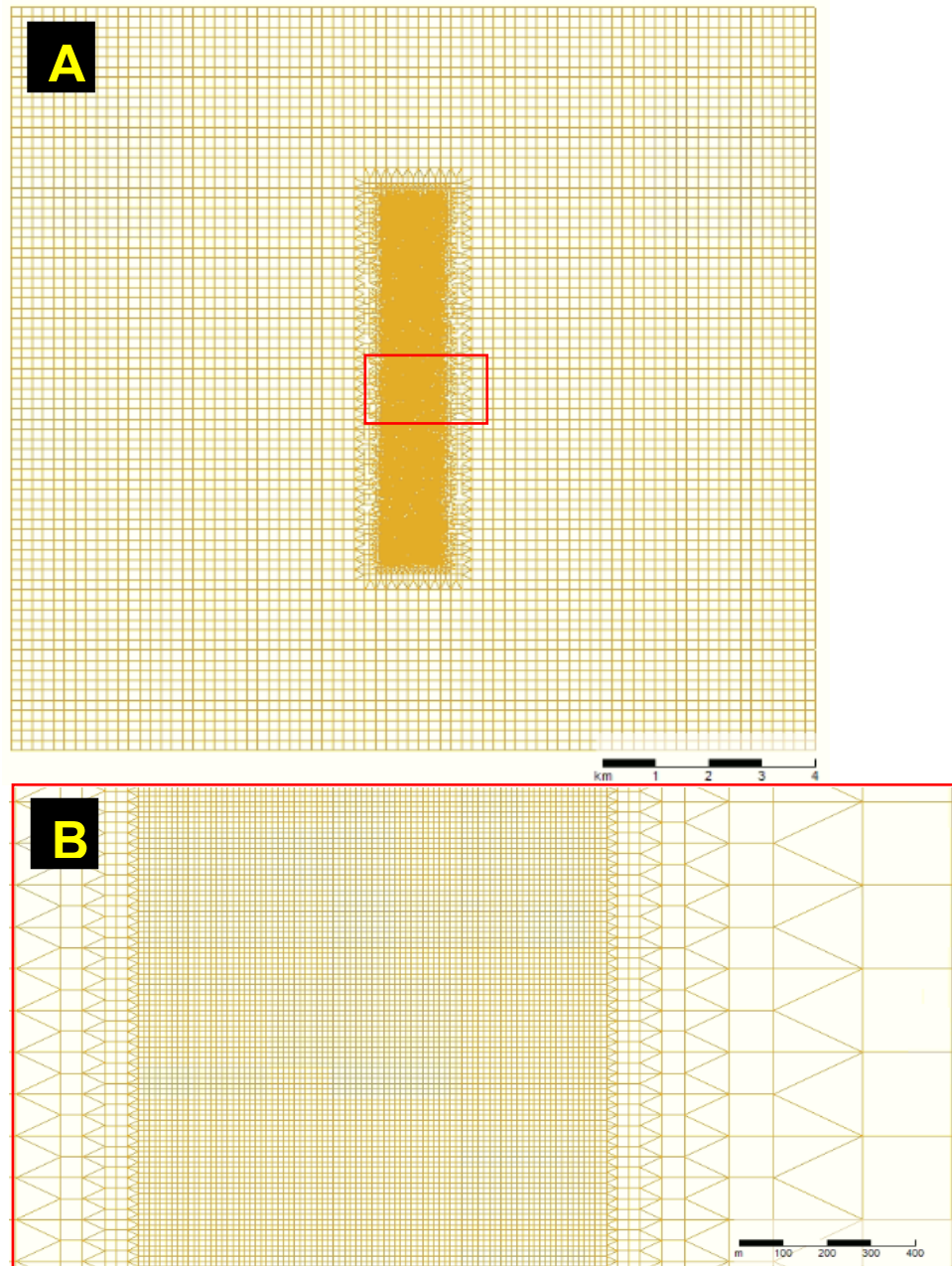


Figure 20. Model grid resolution within the hypothetical basin shown in Figure 19. Panel (A) is the entire extent of the grid, illustrating the central location of the high resolution region for test runs using the linear terrace design. Panel (B) is a magnified view of the high resolution area (red box in panel A) and the transition zone between the fine and coarse zones of grid resolution.

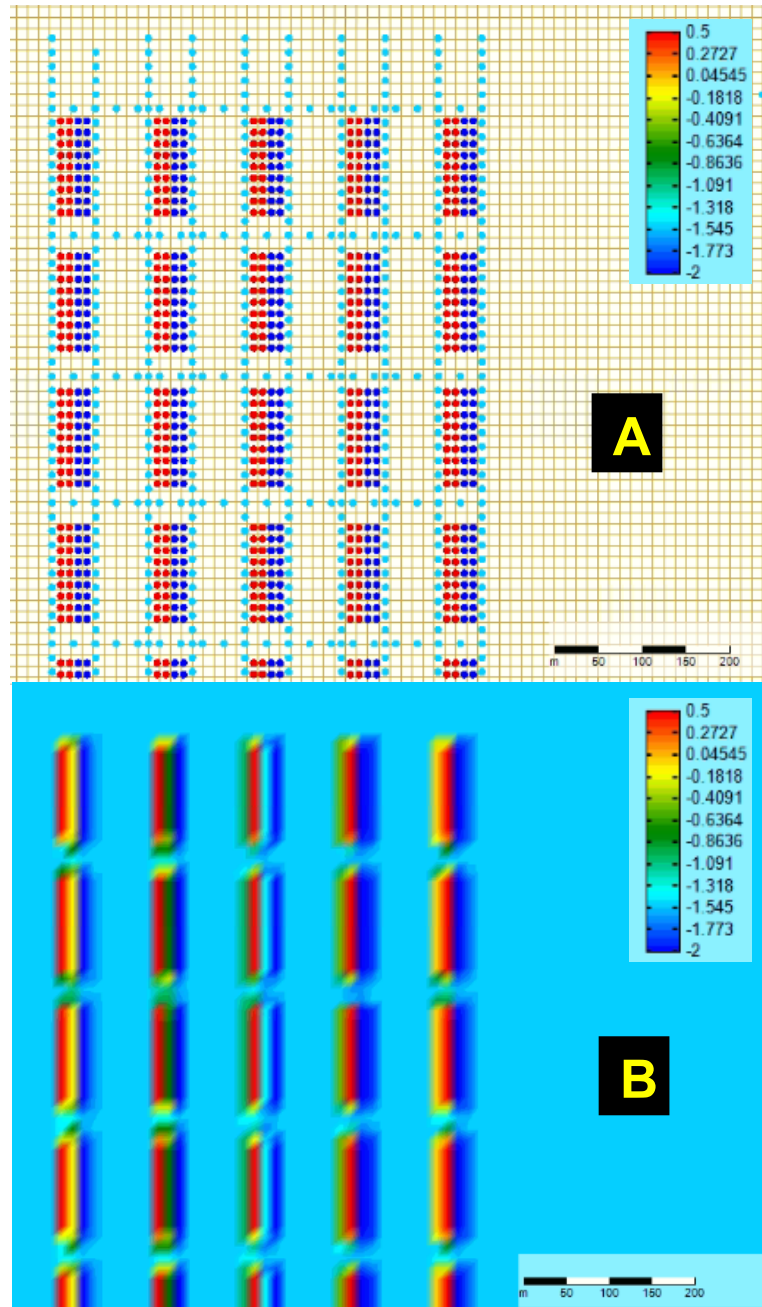


Figure 21. Model bathymetry setup within the hypothetical basin. Panel (A) shows the linear terrace bathymetric points assigned prior to interpolation. Panel (B) shows the Triangulation interpolation of the points in Panel (A) for the linear terrace simulation. Terraces are constructed as raised bathymetry (0.5m) relative to the bed. Borrow pits are presumed to be of equal volume with their adjacent terraces.

the adjacent borrow pits. The calculation for borrow pit depth is based on the construction assumption that the volume of material excavated from each pit is equal to the volume of the adjacent marsh terrace. For the calculation of grid terrace borrow pits, interior borrow pits were halved in size because each marsh terrace was presumed to be built from two borrow pits, resulting in shallower internal borrow pits and deeper borrow pits along edge terraces. To encourage smooth interpolation of the resulting bathymetry, additional interpolation points with non-adjusted (-1.5 m) bathymetry values were placed along the border of each terrace and borrow pit. Grid terraces required additional non-adjusted bathymetry points placed between internal borrow pits to ensure the platform at the pond center was replicated in the model.

3.3.2 Boundary Conditions and Physical Parameters

The model used two hydro boundary conditions – an upstream flow (river discharge) and a downstream tidal boundary. The upstream flow was a constant discharge of 10 m³/s. The tidal boundary utilized observed hourly water level data from the National Oceanic and Atmospheric Association (NOAA) station at Grand Isle, Louisiana (ID# 8761724). A constant wind with a uniform velocity (15 m/s) and direction (0, 45, or 90°) was applied to the domain for the duration of each simulation with a Smith and Banks (2 break points) wind drag coefficient.

3.3.4 Simulation Settings

One simulation for each wind direction (0, 45, or 90°) and each terrace geometry (linear, grid, chevron, or none) was run, resulting in 12 independent simulations. Each

simulation ran for five days (from 2018-01-01 00:00:00.00 to 2018-01-06 00:00:00.00). Observation points (158) centered in the domain capture changes before, within, and after the terrace field in all directions. For all 12 simulations a dynamic time-step was utilized with minimum and maximum allowable time-steps of 1 and 30-seconds, respectively. The model was configured to select the appropriate time-step based on a maximum Courant number of 0.7 (Deltares). The 5-day simulations each took between 20 to 24 minutes to run on a SAR-WIN10 device (desktop PC) with dual 2.20 GHz processors. Sediment and morphology were not activated for these simulations to speed run time.

4. Results

4.1 Short-term deposition

Short-term deposition rates (days to months) and the characteristics of deposited sediment (mineral and organic) were determined using feldspar marker horizons at Bayou Monnaie and Yankee Canal, and ^7Be activity from cores taken at Bay Alexis. In the present study, feldspar-derived deposition rates represent 71 d (Bayou Monnaie) or 72 d (Yankee Canal) of unconsolidated deposition, while ^7Be deposition rates derived from the thickness of the active layer in cores describe the previous ~250 d of unconsolidated deposition. Of 66 feldspar plots deployed, 56 proved viable for assessment or sample collection – the remainder were either washed away by erosion in the interim or the marker flags could not be located. The missing plots include seven at Bayou Monnaie and three at Yankee Canal. At both sites, washouts occur primarily along the marsh terrace shoreline (e.g., those sites of lowest elevation with the largest frequency of

submergence and exposure to wave action). At Bay Alexis, depth of penetration and ^7Be activity profiles were measured at 11 core sites to provide a corollary to the feldspar method for measuring short term deposition utilized at the other two sites.

4.1.1 Feldspar and ^7Be Deposition Rates

Over 71 days (02/04/20 to 04/15/20) the feldspar plots at Bayou Monnaie accumulated between 0 and 18mm of sediment (mineral and organic), resulting in rates ranging from 0 to 0.253 mm/day across three terraces (Figure 22). Over 72 days,



Figure 22. Deposition rates derived from feldspar plots at Bayou Monnaie over 71 days across 3 terraces. Values range from 0 mm/d to 0.25 mm/d (0 – 18 mm over 71 days). There is an inverse relationship between elevation and accretion on terraces at Bayou Monnaie.

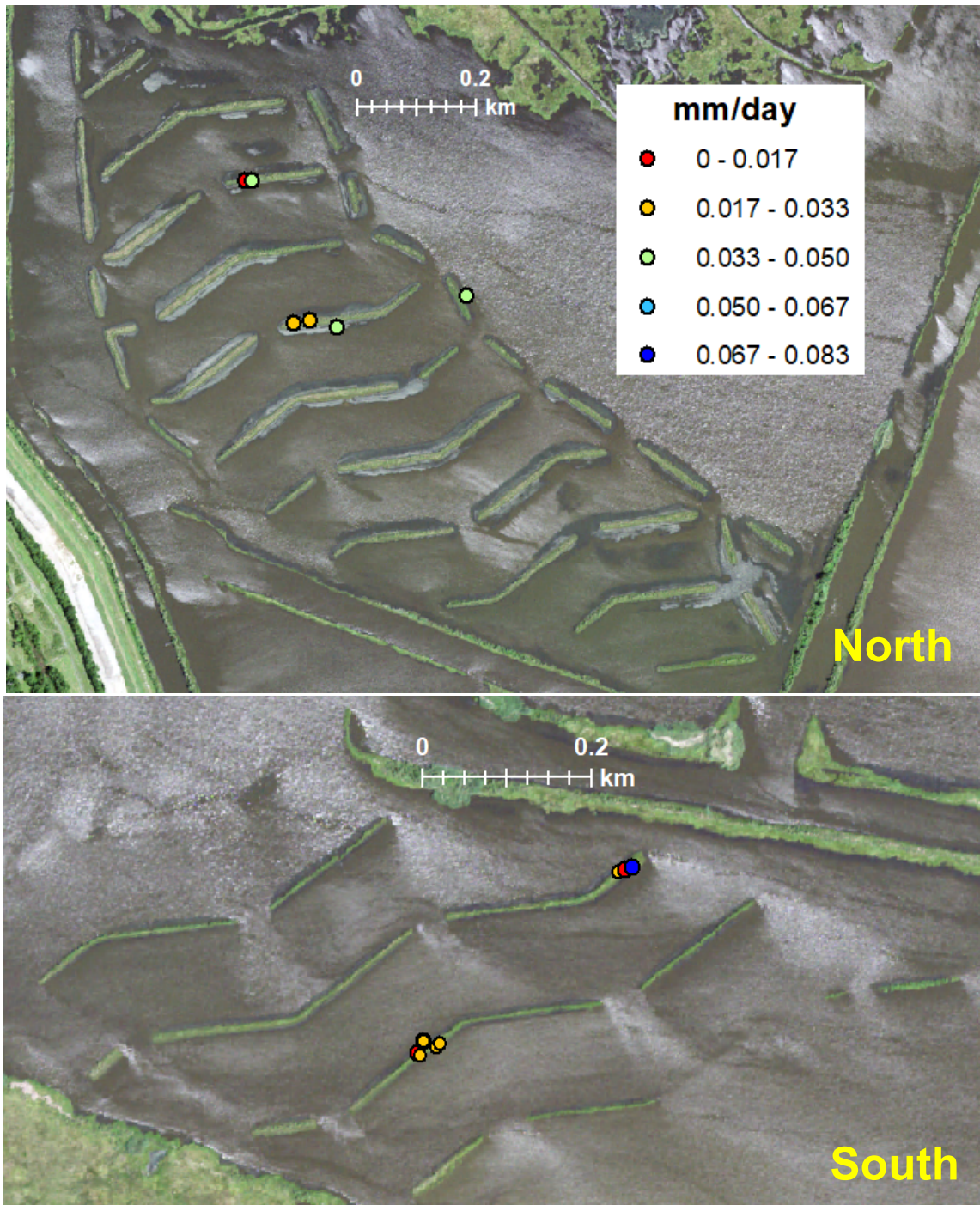


Figure 23. Deposition rates derived from feldspar plots at Yankee Canal over 72 days across six terrace sites. Values range from 0 mm/d to 0.083 mm/d (0 – 6 mm over 72 days). There is an inverse relationship between elevation and accretion on terraces at Yankee Canal.

(03/10/20 to 05/21/20), the feldspar plots at Yankee Canal accumulated between 0 and 6 mm of material, yielding deposition rates ranging from 0 to 0.083 mm/day (Figure 23). Despite the loss of 10 total shoreline plots, both sites record a relationship between elevation of the site (flooding hydroperiod) and deposition rate (Figure 24). It should be noted that one point of 18 mm (62.5 cm NAVD88) was removed from the Bayou Monnaie dataset given its unique location at the end of a terrace adjacent to a major channel within the field. This plot was positioned on a terrace scarp with high elevation and frequent interaction with the adjacent channel flow. No other points were collected on terrace edge scarps to validate this retrieval data as there are relatively few end scarps present at Bayou Monnaie. At both Bayou Monnaie and Yankee Canal, the only plots to record no deposition were located on the terrace tops at elevations above 60 and 30 cm NAVD88, respectively; the terrace cross-section tends to be mounded with a central apex equidistant from both shorelines of the terrace. Tables A1 and A2 (Appendix A) provides the rate of deposition calculated along each terrace.

At the third site (Bay Alexis), where ^7Be was utilized to measure deposition rates instead of feldspar, depth of penetration ranged from 0 to 5 cm, and surficial (0-1 cm

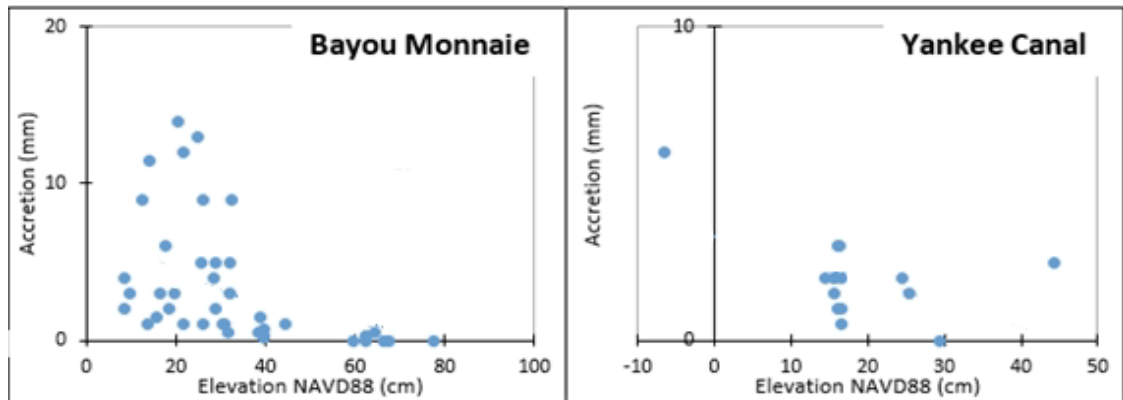


Figure 24. Relationship between accretion rates at feldspar plots in Winter-Spring 2020 and elevation (in NAVD88) at Bayou Monnaie (left) and Yankee Canal (left). Best-fit regressions for these datasets are also shown.

interval) activities were up to 4.81 ± 0.69 dpm/g across the 11 sites cored. Deposition rates derived from unconsolidated depths, which correspond most closely to the feldspar measurement technique, range from 0.037 to 0.245 mm/day (Table 1; Figure 25A). For inter-comparison with feldspar rates, it should be noted that ^7Be can be measured up to 4-5 half-lives in age (3-6% of initial activity), corresponding to ~ 250 d, which averages deposition rates over a period of time more than 3x that of the feldspar deployments (71 and 72 d). That ~ 250 -day period extends backward from the coring date at Bay Alexis (05/13/20).

^7Be can also be expressed in total depth-integrated inventory at a site, which is a measure of total deposition that also allows examination of site-to-site variations in activity that are driven by particle origin and grain size as well as total amount deposited in ~ 250 d. At Bay Alexis, total inventories ranged from 0.042 to 3.79 dpm/cm² (Table 1; Figure 25B). Recognizing that some of the site-to-site variability is ^7Be deposition rates that can be caused by differences in porosity of the ^7Be -active layer, core intervals were consolidated to a standardized mean porosity (0.75), and these corrected depths in the core were then used to derive an independent decay regression line and deposition rate; these consolidated deposition rates range from 0 to 0.102 mm/day and differ from unconsolidated deposition rates (Table 2; Figure 26). These values were then utilized to calculate a mass depositional flux, which varies from 0 to 0.067 mg/cm²/day (Table 2).

Table 1. Deposition rates of ^7Be activity of 11 cores collected in the terrace fields at Bay Alexis in May 2020 derived from unconsolidated depths. DOP = depth of ^7Be penetration in the core.

Site	DOP cm	Deposition rate mm day^{-1}
1BA	3	0.049
2BA	0	0
3BA	2	0.037
4BA	4	0.081
5BA	1	0.023*
6BA	>3	0.245
7BA	2	0.046
8BA	>3	0.215
9BA	3	0.063
10BA	5	0.094
11BA	1	0.017*

Table 2. Rates and inventories of ^7Be activity across 11 cores collected in the terrace fields at Bay Alexis derived from consolidated depths and all available activity measurements. Asterisk (*) denotes samples derived from two activity depth measurements ($r^2 = 1$).

Site	Deposition rate mm day^{-1}	Mass deposition flux $\text{mg cm}^{-2} \text{day}^{-1}$	Integrated inventory dpm cm^{-2}
1BA	0.012	0.008	1.58
2BA	0	0	0.042
3BA	0.031	0.021	0.748
4BA	0.024	0.016	2.64
5BA	0.019	0.001	0.333
6BA	0.102	0.067	1.47
7BA	0.024	0.016	0.187
8BA	0.034	0.022	0.144
9BA	0.023	0.016	1.42
10BA	0.054	0.036	2.75
11BA	0.015	0.001	1.35

Rates and fluxes displayed in Table 1 and 2 were calculated using linear regression statistics which were derived from all ^7Be -active depth layers and the first depth interval moving down from the sediment surface where ^7Be activity ceased (i.e., where activity first equals 0 dpm/g), when applicable. To estimate the age of the deepest

⁷Be-active layer, these rates and fluxes were also calculated excluding activities equal to 0 dpm/g, thereby limiting linear regressions to the ⁷Be-active interval. By excluding inactive (zero measured activity) layers, the linear regressions produced more representative curves than curves fit to all layers. This is explained by non-constant deposition, which would not present a consistent decrease in activity with depth but rather indicate a sharp start/stop. Six of 11 cores were counted to an inactive depth, but only four were reassessed with new linear regressions because the remaining two cores – 5BA and 11BA – had a single Be-active interval (0-1cm). A linear regression could not be performed on a single point. Based on non-zero active layers and unconsolidated depths, the deposition rate varies from 0.090 to 0.418 mm/day. These rates are greater than the previous rates presented in Table 1 (0.037 to 0.094 mm/day). Consolidated depths from these cores yielded deposition rates from 0.035 to 0.218 mm/day, which exceeds the aforementioned range of deposition predicted by these 4 cores (0.012 to 0.031 mm/day). The mass depositional flux computed from consolidated depths ranges from 0.023 to 0.115 mg/cm²/day (Table 3), which is also greater than the fluxes calculated in Table 2. The age of the active ⁷Be layer is calculated using the following equation (Equation 5):

$$N(t) = N_0 e^{-\lambda t} \quad (5)$$

where $N(t)$ is the initial quantity, N_0 is the remaining quantity after time t , and λ is the decay constant for ⁷Be. The age of the active layer of ⁷Be ranges from 7.72 to 22.35 days (Table 3). The $t_{1/2}$ for ⁷Be is 53.3 days, so the deepest active layer is approximately half one (1) half-life old, indicating deposition started less than one half-life prior to collection.

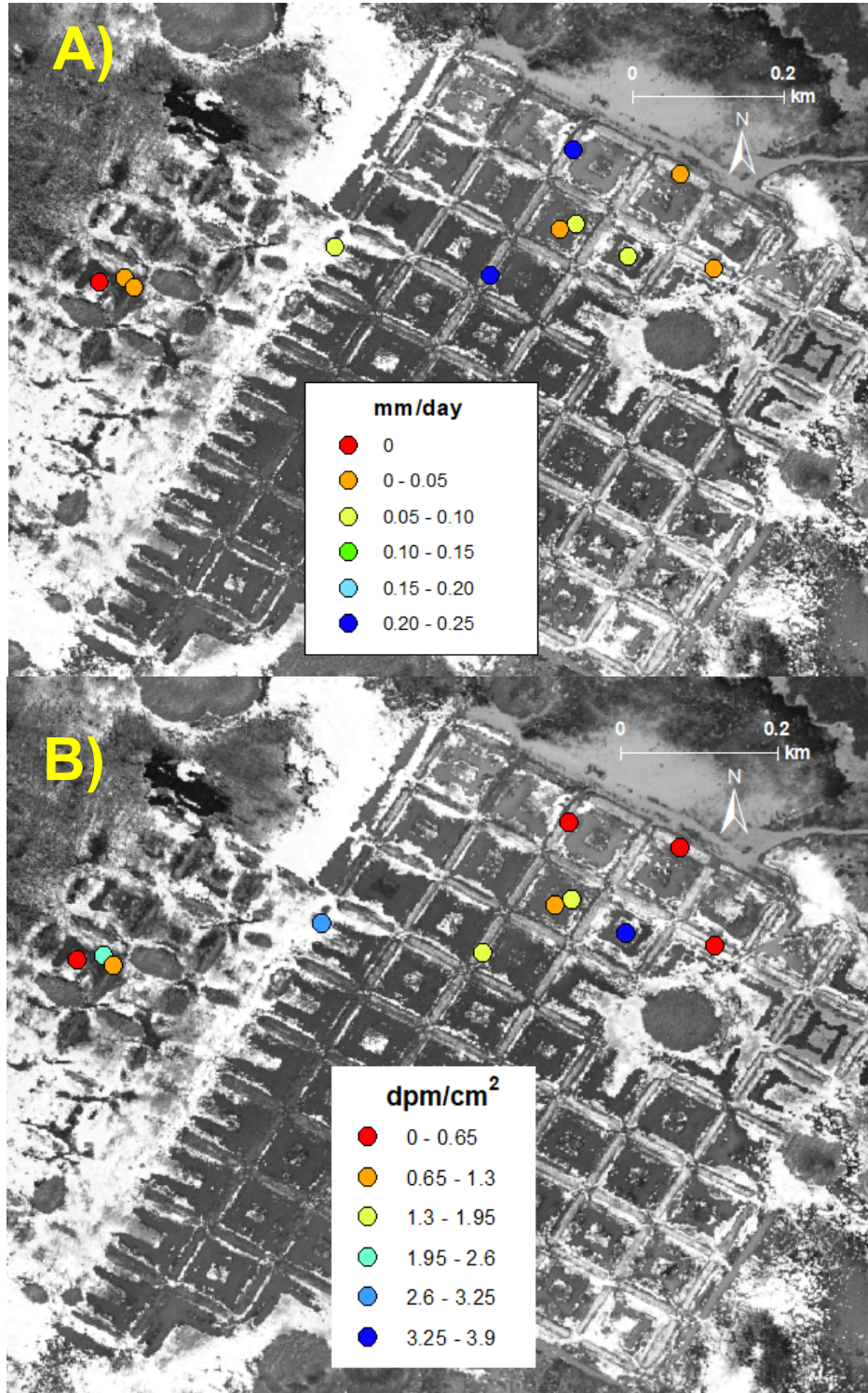


Figure 25. Deposition rates (mm/d) and ^7Be inventories (dpm/cm²) at Bay Alexis. A) Deposition rates derived from ^7Be activity at unconsolidated depths from cores collected at Bay Alexis. B) ^7Be integrated inventory values from the same cores.

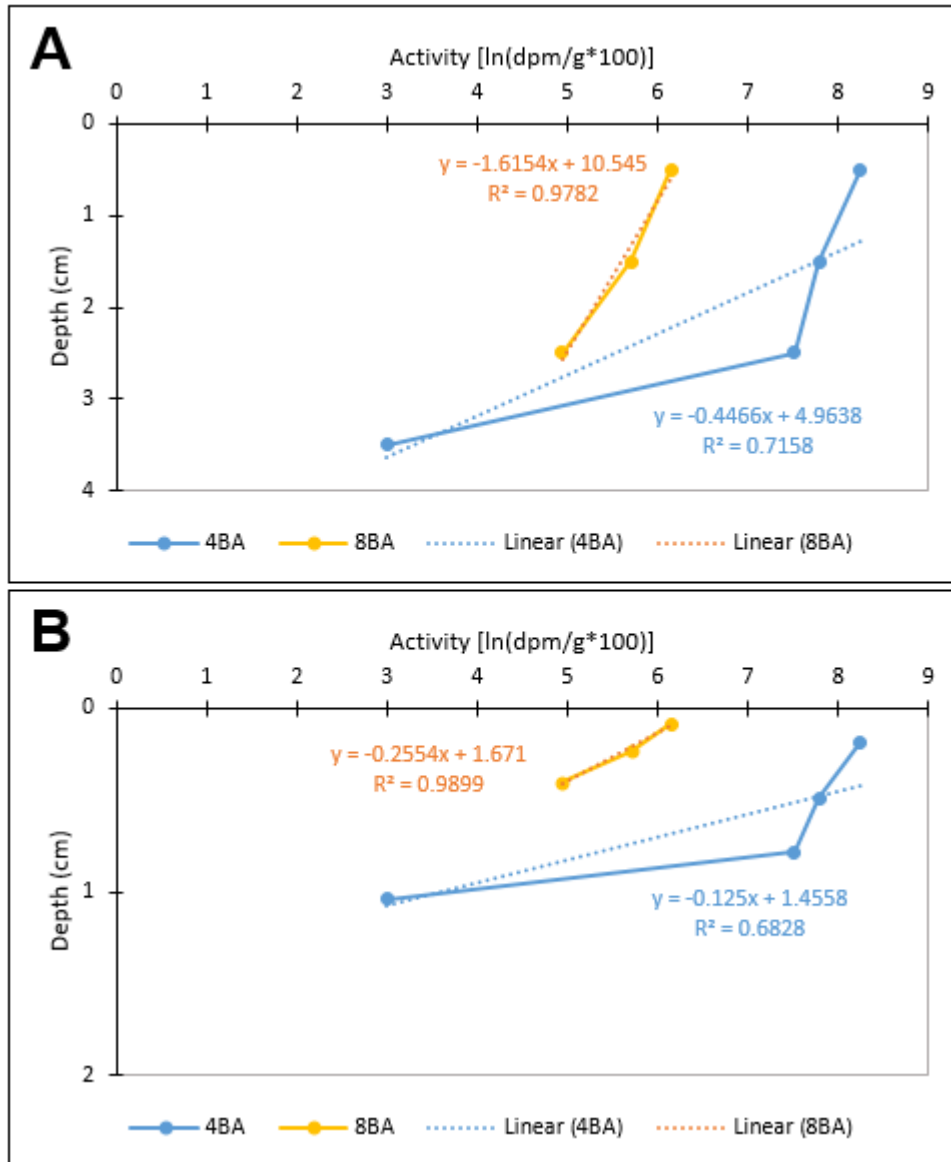


Figure 26. Downcore ^7Be activity in two cores from Bay Alexis. Note that the unconsolidated plots (panel A) and consolidated plots (panel B) illustrate the same overall downcore trend, though the latter occurs at shallower depths. The unconsolidated deposition rates for 4BA and 8BA are 0.081 and 0.215 mm/d, respectively. The consolidated deposition rates are 0.024 and 0.034 mm/d, respectively as well.

Table 3. ^7Be deposition rates and mass deposition fluxes from four of eight cores reassessed by excluding activities equal to 0 dpm/g. Values presented are derived from both unconsolidated and consolidated depths.

Site	Unconsol. Deposition rate mm day^{-1}	Consol. Deposition rate mm day^{-1}	Mass depositional flux $\text{mg cm}^{-2} \text{day}^{-1}$	Age of active ^7Be interval days
1BA	0.136	0.035	0.023	22.35
3BA	0.090	0.051	0.034	22.12
7BA	0.331	0.218	0.144	7.72
9BA	0.418	0.173	0.115	14.84

4.2 Characteristics of Short-term Sediment Deposition

4.2.1 Bayou Monnaie

Thirty-four of 48 sediment deposition rates are shown in Figure 27 for samples retrieved from three terraces at Bayou Monnaie. Seven sites were washouts with no visible feldspar, and seven plots either indicated no deposition (5) or the deposition was

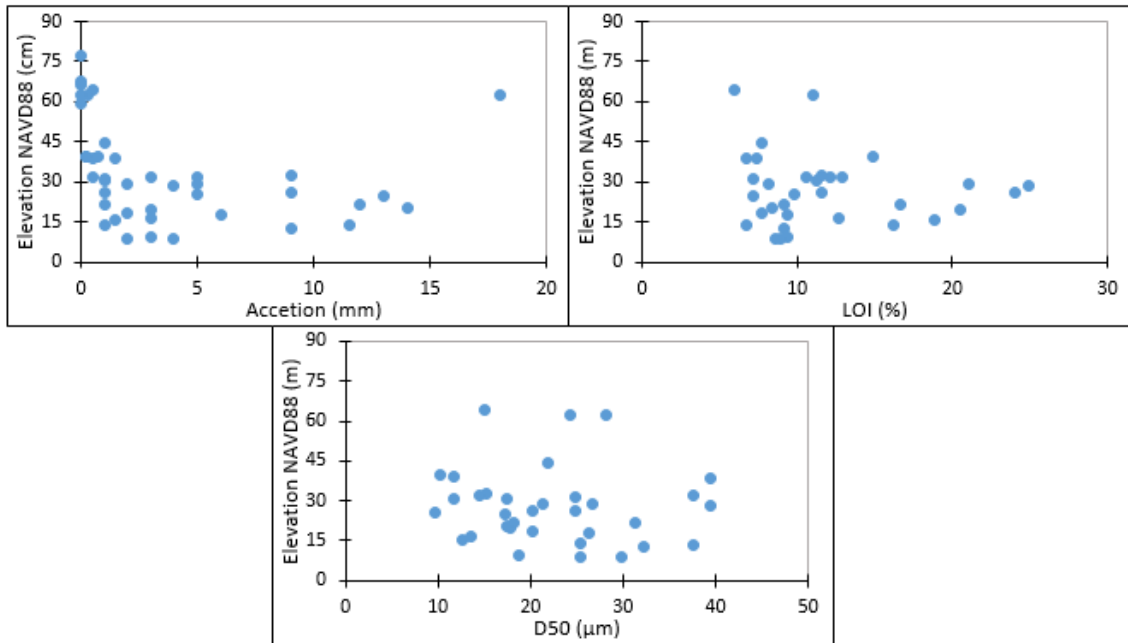


Figure 27. Properties at Bayou Monnaie from feldspar plot samples against elevation measured to NAVD88. A) Total accretion (mm) over 71 days. B) LOI (%). C) Median grain size (D_{50}). There is a coarse trend of increasing organic content (LOI) with increasing elevation, but there is no trend between D_{50} and elevation at Bayou Monnaie.

too thin to yield a viable sample (2). In general, the trend was for decreasing deposition with elevation on the terrace. Porosity, organic matter (OM) contents (LOI), average particle size (D_{50}), saturated bulk density (SBD), and estimated dry bulk density (DBD) are presented in the Appendix (Table A3) and in Figure 27. Porosity values are between 0.48 and 0.73 with percent organic matter based on LOI ranging from 6.71 to 24.06%. Based on the Wentworth (1922) grain size classification, all samples from Bayou Monnaie are classified as fine (8), medium (20), or coarse (6) silt as D_{50} is no larger than $39.5\mu\text{m}$ and no smaller than $9.77\mu\text{m}$. LOI showed a coarse trend of increasing organic content for the low elevation sites, while grain size (D_{50}) exhibited no elevation-related trends.

4.2.2 Yankee Canal

Of 18 plots deployed, 14 were recovered from across six terraces at Yankee Canal (Figure 28). Three plots indicate washouts with no retrievable feldspar, and one showed no deposition, yielding no sample for collection. Table A4 in the Appendix presents porosity, OM contents (LOI), average particle size (D_{50}), saturated bulk density, and estimated dry bulk density values for feldspar samples from Yankee Canal (Figure 28). Porosity values show little variation, ranging from 0.39 to 0.42. Percent organic matter based on LOI ranges from 9.86 to 42.00%. Based on the Wentworth (1922) grain size classification, the samples from Yankee Canal are classified as fine (4), medium (8), or coarse (1) silt as D_{50} falls between 11.2 and $32.6\mu\text{m}$, inclusively. The grain size for one sample (4-2) is not included as its material was insufficient for measurement. No trend

with elevation is observed for either sediment deposition rate, LOI or D_{50} at the Yankee Canal site.

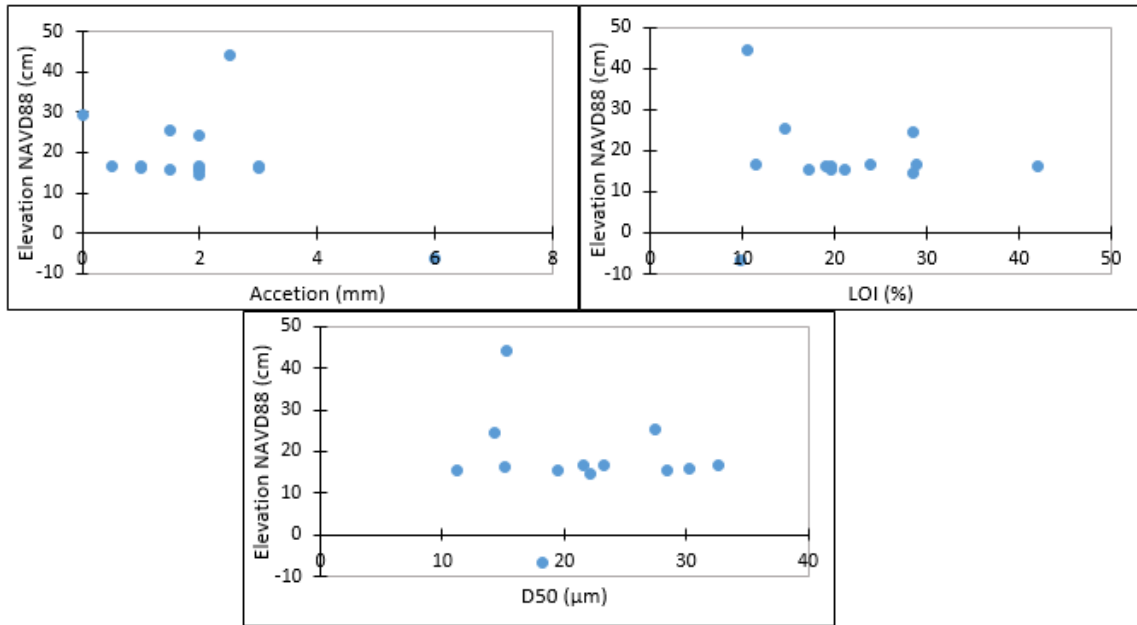


Figure 28. Properties at Yankee Canal from feldspar plot samples against elevation measured to NAVD88. A) Total accretion (mm) over 72 days. B) LOI (%). C) Median grain size (D_{50}). No trend is observed between elevation and organic content (LOI) or D_{50} at Yankee Canal.

4.2.3 Bay Alexis

Samples from 11 cores collected within the terrace fields to characterize the short-term deposition (^7Be) deposition at Bay Alexis (Figure 29) were also analyzed for sedimentological properties. The unconsolidated depth of penetration determines the inclusive depth interval used for analysis from each core. Appendix Table A5 show porosity, OM contents (LOI), average particle size (D_{50}), saturated bulk density, and dry bulk density for Bay Alexis. Dry bulk density is a function of the dry weight because the volume of each sample interval is known. Due to the complexity of the grid terrace design and its construction methods, results are reported classified by sub-environment. This was also enabled by the collection of information from submerged areas of the

terrace field unlike the feldspar plot method used at the other two sites. The results show an inverse relationship between elevation and accretion in the submerged areas of the terrace field, as is consistent with the results from Bayou Monnaie and Yankee Canal where accretion decreases as elevation increases on the terraces.

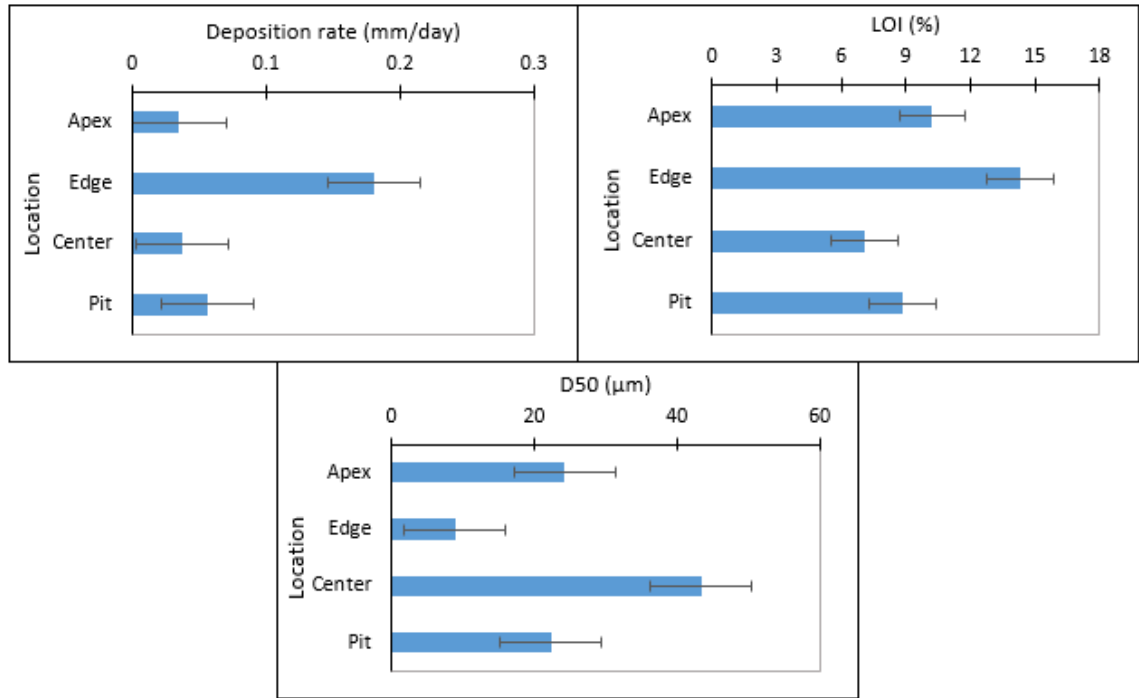


Figure 29. Properties at Bay Alexis from 11 cores against elevation by location within the terrace field. A) Total deposition (mm/d) derived from ^7Be activity. B) LOI (%). C) Median grain size (D_{50}).

4.3 Core Stratigraphy and Properties

Idealized stratigraphic columns from representative transects between terraces at Bayou Monnaie are shown in Figure 30. Derived from piston and auger cores, the stratigraphic columns reflect the sedimentary characteristics described upon section and from laboratory analyzes of sedimentological parameters. The mineral granulometric values were obtained from core descriptions and from Malvern laboratory analysis of aliquots after the LOI removal of organic constituents. All core intervals measured can

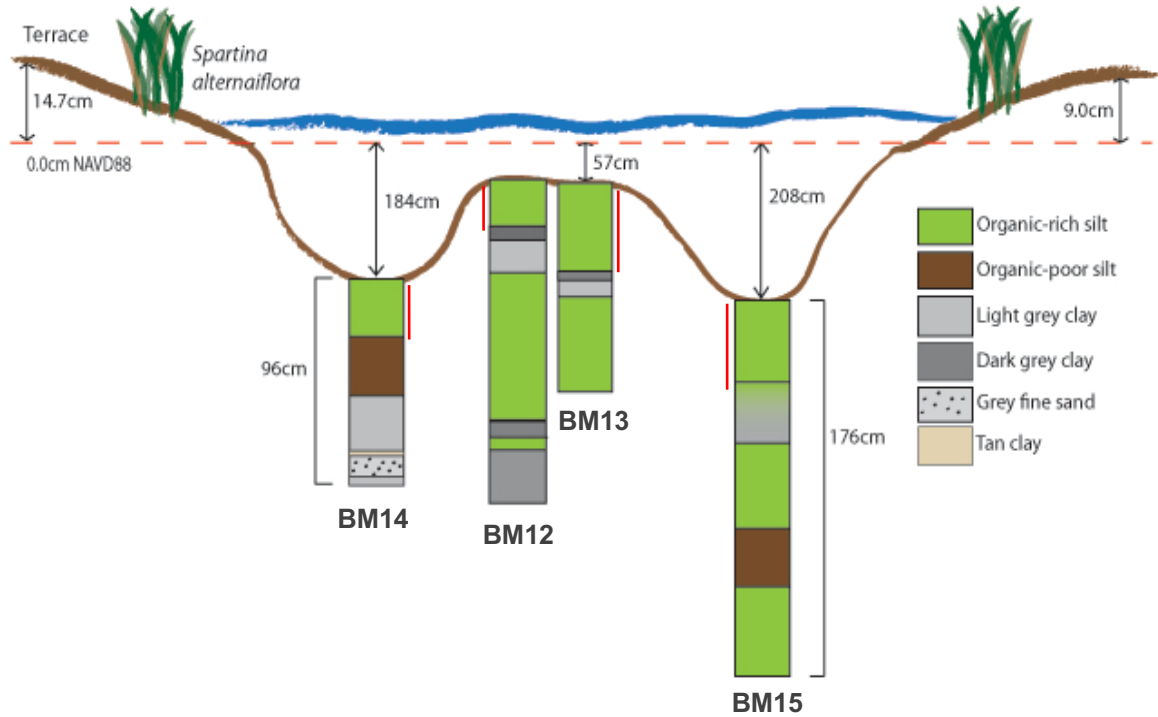


Figure 30. Transect collected from Bayou Monnaie on 06/14/2018 between two terraces. Field descriptions drive stratigraphic distinctions. Peat and clay layers appear consistent across the field, allowing for horizontal interpretations. Red line indicates extent of Organic-rich Mud (high porosity). All elevations measured to NAVD88.

be classified as either clayey silts or silty clays, with organic content varying from ~7 to 78% at Bayou Monnaie and 3.5 to ~25% at Yankee Canal. Facies were determined using organic content (through the LOI proxy) and porosity values as explained in the methods (§3.2.1.1 Bulk Properties and Sedimentary Facies).

Using the organic content and porosity distinctions, all Bayou Monnaie and Yankee Canal cores show two distinct layers and most (4 of 6) long cores at Bay Alexis do as well. At Bayou Monnaie, surficial layers and shallower intervals are represented by low porosity and low organic content. These intervals range from 2 to > 24 cm with the thickest low porosity, Organic-poor Muds found in excavation pits. Deeper layers are distinctly different high porosity, Organic-rich Muds and are found at shallower depths on the central plateaus between terraces than in excavation pits. The longest cores were

collected Bayou Monnaie and indicated additional facies beneath the high porosity, organic-rich layer that were distinguished by color (Figure 30). At Yankee Canal (Figure 31), the surficial layers – ranging in thickness from 0 to 28 cm – are high porosity, Organic-rich Mud. The thickest high porosity, Organic-rich Mud surficial layer is located in the plateau areas of the South field and in excavation pits in both the North and South fields. The deeper intervals are low porosity, Organic-poor Mud. This stiff, Organic-poor Mud is exposed at the sediment surface on the central plateaus of the North field at Yankee Canal. Additionally, the facies at Yankee Canal show distinct colors; the surficial layer of high porosity, Organic-rich Mud is brown and the underlying low porosity, Organic-poor mud is grey (Figure 32). Sufficient LOI data is not available for Bay Alexis to define facies based on organic content, so facies were determined using porosity values only. At Bay Alexis, the surficial layer is a high porosity mud and ranges in thickness from 1 to 34 cm. The thickest high porosity muds are located in the Old terrace field and in excavation pits in the New field. Deeper intervals are low porosity muds and are found at the shallowest depth in cores from the central plateaus between terraces in the New field. Stratigraphic transects did not include cores from the subaerial marsh terraces themselves because the terrace stratigraphy was extensively reworked during excavation, construction, and the subsequent consolidation and reorganization of its sediments.

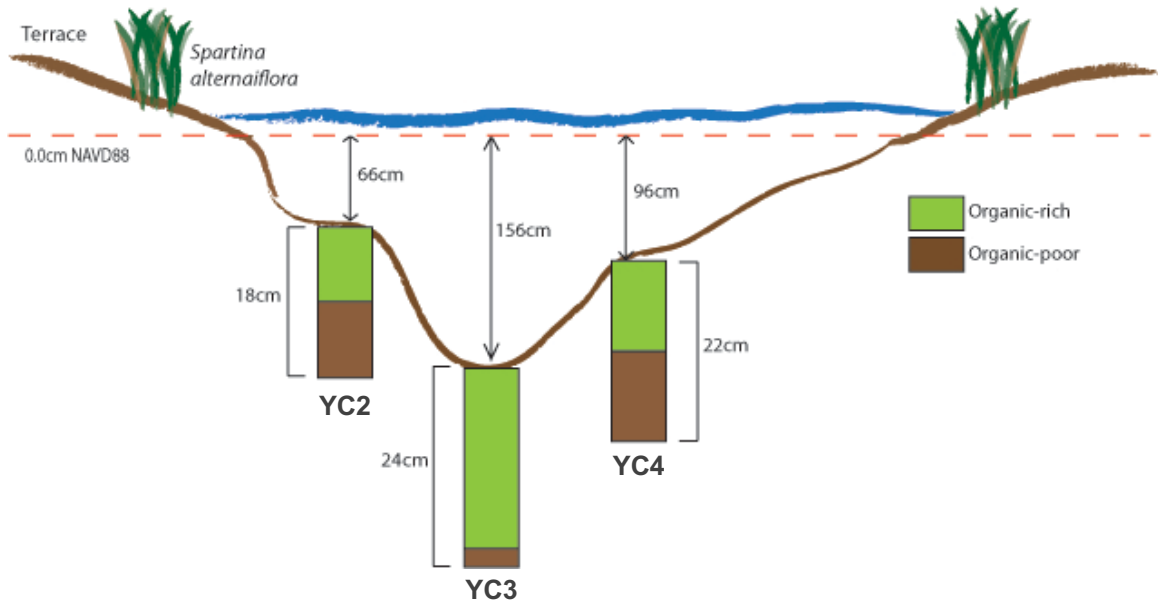


Figure 31. Transect collected from Yankee Canal on 03/19/2020 between two terraces. Field descriptions, porosity, and organic content drive stratigraphic distinctions. All elevations measured to NAVD88.



Figure 32. Piston cores from Yankee Canal subaqueous sites between the terraces, illustrating the visual differences between the interpreted pre-construction, stiff grey clay layer and the surficial black-brown and high porosity silt. Core YC8 (left) from an excavation pit shows a ~25 cm of distinct surficial material interpreted as post-construction deposition, while the deposit in core YC14 (right) on an adjacent (shallower) area that was not excavated is < 1 cm thick.

4.4 Remote Sensing Analysis

Each classified image from the remote sensing (geospatial) analysis of the 10 Louisiana terrace fields examined using satellite imagery is compartmentalized spatially into four classes – marsh, vegetated mudflat, bare mudflat, and water. Given that each class was assigned an integer value on a pixel-by-pixel basis, upon subtraction to produce the difference map, up to 13 resultant integer subclasses were produced that categorize the change between two images (Table 4). Marsh conversion to any other class (i.e., water, vegetated mudflat, bare mudflat) is categorized as marsh (land) loss. Marsh growth (land gain) is defined by the conversion of any of the other three classes into marsh. For clarity in defining changes meaningful to the goals of the present study, vegetated mudflat and bare mudflat classes were combined when presenting or discussing change maps unless otherwise indicated. Hectare area change in each category in Table 4 in the pre- and post-construction period is presented in Appendix B.

Table 4. Definition of change detection by integer value utilized in the image classification analysis. Gain and loss in spatial extent are indicated by red and green, respectively.

Integer	Corresponding Change
-6	Water to marsh
-5	Water to vegetated mudflat
-4	Bare mudflat to marsh
-3	Bare mudflat to vegetated mudflat
-2	Water to bare mudflat
-1	Vegetated mudflat to marsh
0	No change
1	Marsh to vegetated mudflat
2	Bare mudflat to water
3	Vegetated mudflat to bare mudflat
4	Marsh to bare mudflat
5	Vegetated mudflat to water
6	Marsh to water

4.4.1 Overall Marsh Area Change In Terrace Fields Pre- and Post-Construction

Each site was initially assessed for sitewide annual marsh area change (ha/y), which includes bounding marsh, its shoreline, and the terrace field within the study area polygon before and after terrace construction (Table 5). Prior to terrace construction, 6 of 10 (60%) studied sites (2015W, 2015E, 3008, 3006, 7006N, and 7006S) were experiencing overall marsh area loss. This land loss ranged from 0.136 ha/y between 2015 and 2017 to 2.554 ha/y between 2007 and 2017 at 7006S and 2015W, respectively. Four of 10 (40%) of sites were experiencing land gain prior to terrace construction, ranging from 0.101 ha/y (at 2015C from 2007 to 2017) to 2.284 ha/y (at 1102 from 2005 to 2017). Following terrace construction, sites 3008 (2005 to 2017), 3006 (2005 to 2017), and 7006S (2015 to 2017) saw increased land loss rates relative to the pre-construction analysis period. Additionally, sites 1102 and 5001 exhibited land loss following terrace construction (both from 2005 to 2017), at sites that had previously recorded land gain. One site (7006N from 2015 to 2017) displayed a continued, albeit reduced rate of land loss following terrace implementation (Table 5). Overall polygon land gain occurred at 4 sites (2015W, 2015C, 2015E, 7001) after terrace construction, with land gain ranging from 0.089 ha/y to 1.795 ha/y at 2015E (2007 to 2017) and 2015W (2007 to 2017), respectively. At two of these sites (2015W, 2015E), this marsh area gain reversed a trend of pre-construction land loss. The 2 other sites (2015C, 7001) experienced an increased rate of overall marsh land area gain post-construction (Table 5).

Table 5. Annual marsh land change (ha/y) at each remote sensing site before and after terrace construction for the entire polygon of the studied sites and years studied. Conversion of marsh to any other class defines land loss (ref), while any change into marsh illustrated land gain (green). Site names are italicized where land gain is greater (or land loss is lesser) following terrace construction.

Site	Δ Before (ha/y)	Δ After (ha/y)	Before (years)	After (years)
1102	2.284	-1.919	1989 to 1998 (9)	2005 to 2017 (12)
<i>2015W</i>	-2.544	1.795	1998 to 2005 (7)	2007 to 2017 (10)
<i>2015C</i>	0.101	0.226	1998 to 2005 (7)	2007 to 2017 (10)
<i>2015E</i>	-1.022	0.089	1998 to 2005 (7)	2007 to 2017 (10)
3008	-0.199	-0.566	1998 to 2004 (6)	2005 to 2017 (12)
3006	-1.132	-1.800	1998 to 2004 (6)	2005 to 2017 (12)
5001	1.783	-3.933	1998 to 2004 (6)	2005 to 2017 (12)
<i>7001</i>	0.975	1.439	1998 to 2007 (9)	2007 to 2017 (10)
<i>7006N</i>	-0.266	-0.227	1990 to 2010 (20)	2015 to 2017 (2)
<i>7006S</i>	-0.136	-0.235	1990 to 2010 (20)	2015 to 2017 (2)

4.4.2 Overall Interior and Exterior Marsh Area Change In Terrace Fields

The overall gain or loss of marsh area inside of each terrace study site polygon took place in three distinct areas—the water body bounding shoreline, the terraces themselves, and fragments of remnant marsh within the water body adjacent to the terrace fields (Figures 33-35). To examine the relative importance of these areas to the overall marsh area change described above, land loss and land gain (change) was differentiated

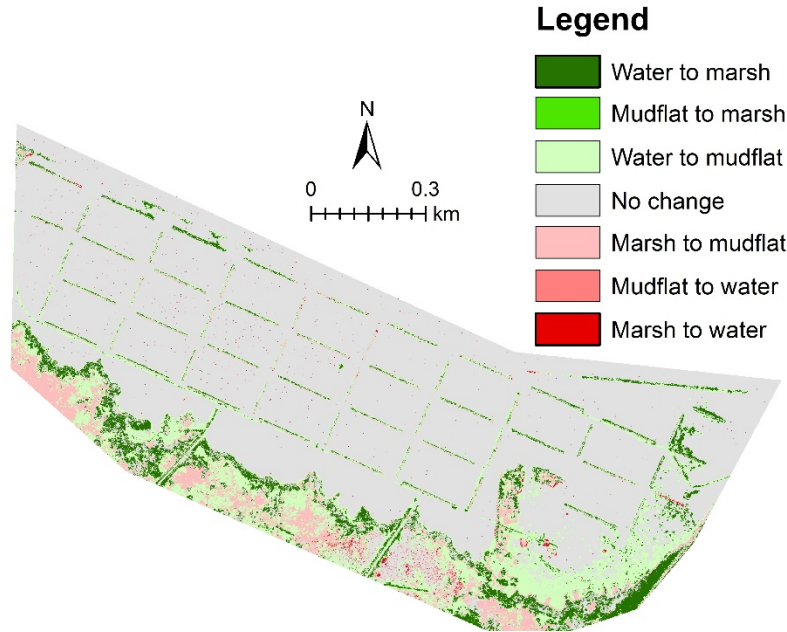


Figure 33. Image analysis of change at site 2015E observed within the grid terrace field and on the adjacent shoreline after construction (2007 to 2017). In this example, marsh land gain after terrace construction occurs predominately along the bounding marsh.

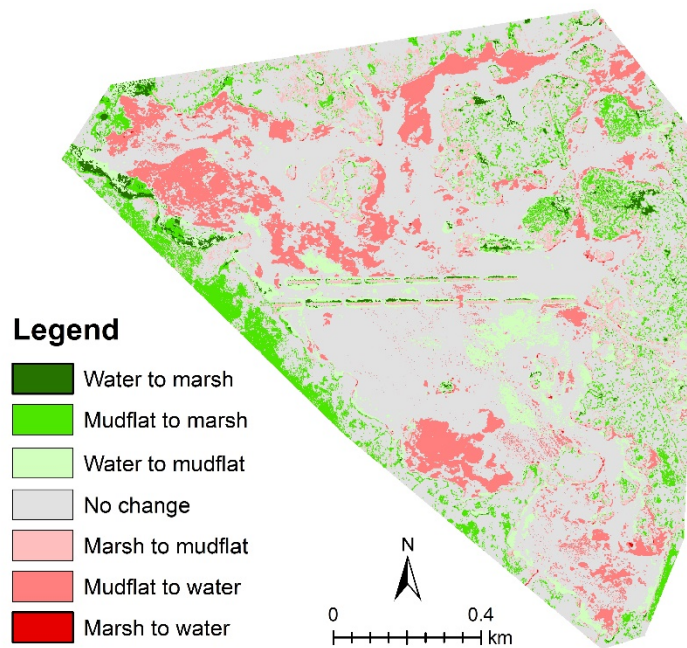


Figure 34. Image analysis of area change observed at site 7001 in the linear terrace field and in the surrounding basin after construction (2005 to 2017). In this example, land gain (water to marsh conversion) occurs predominately within the marsh interior and not in the water body bounding marsh.

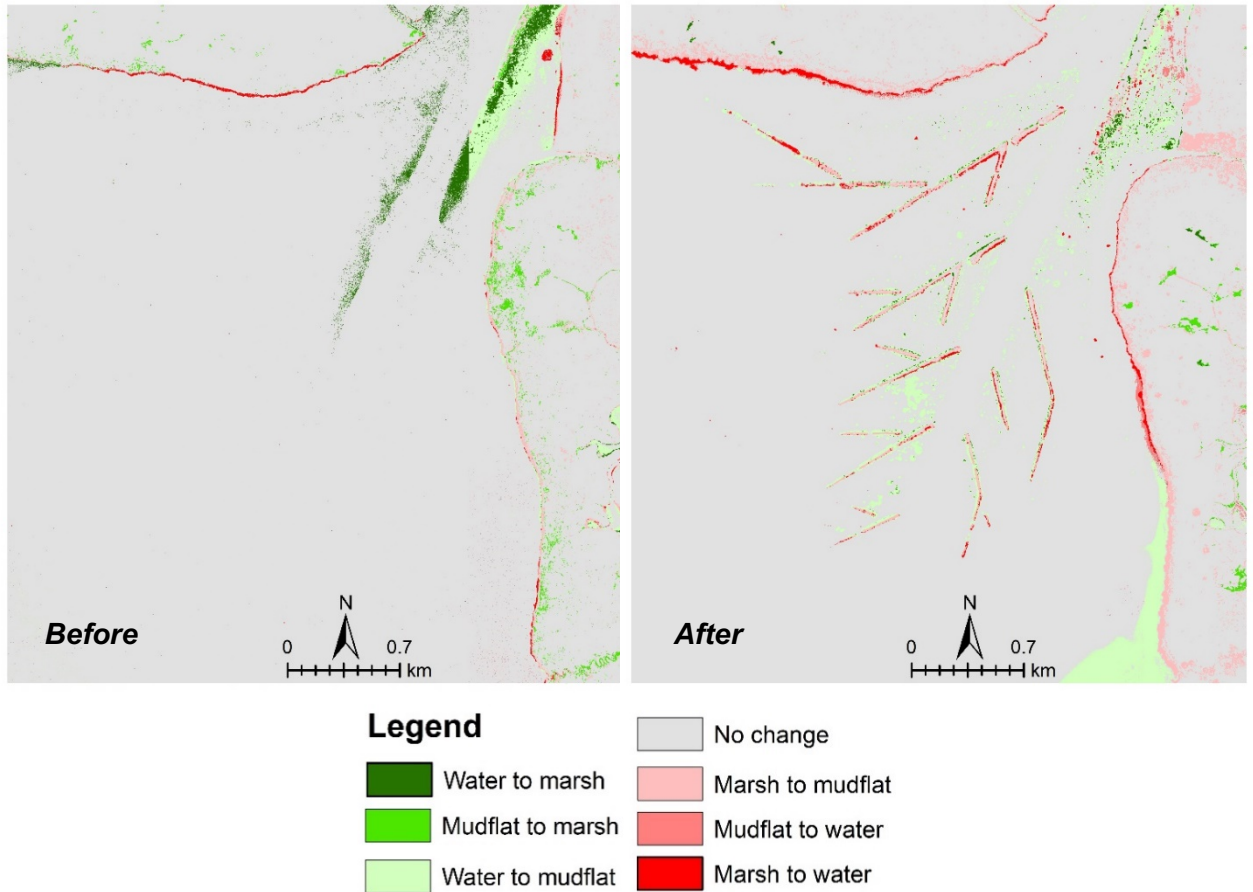


Figure 35. Image analysis of area change observed at site 5001 (The Jaws)7001 in the chevron terrace field and in the surrounding basin shoreline after before (1990 to 2004) and after construction (2005 to 2017). In this example, bounding shoreline erosion persisted even after terrace implementation, but water to marsh conversion decreased and marsh to water conversion accelerated following construction.

between marsh within the terrace field (interior) and along and within the bounding marsh (exterior) using an interior polygon that traced the approximate extent of the terrace field. This also allowed excluding any pre-existing interior marsh and bounding marsh shoreline (i.e., only newly constructed terraces/marsh was included for the interior assessment). Remnant interior marsh areas were lumped with bounding shoreline areas in this activity. As the interior polygon did not including any bounding marsh or remnant interior marsh, no change occurred within the interior polygon prior to terrace construction—it was all classified as either water, vegetated or bare mudflat.

Table 6 presents the annual marsh area change at each study site after terrace construction in the interior (terrace field) and the exterior (bounding and remnant marsh) of the subpolygon-defined field. Only two sites (2015C, 2015E) showed marsh land gain within their terrace field following construction, and both sites indicated even more land gain along the bounding marsh than within the terrace field (Figure 36). The remaining eight sites displayed land loss within the terrace field—evidence of the terraces themselves decreasing in spatial extent after their construction within only 2 to 12 years. At five of these eight sites (63%), the marsh land loss experienced within the terrace field is greater than the land loss experienced along the bounding marsh (Figure 37). Four of these five sites (80%) illustrate land loss within the terrace field but land gain along and within the bounding marsh. The three remaining sites (1102, 3006, and 5001) all show more land loss along the bounding marsh than within the terrace field.

Table 6. Interior (terrace field) and exterior (bounding marsh) annual marsh area change per site after terrace construction at each site compared to total annual loss experienced at each site. Annual land loss is shown in red and annual land gain is green. Site names are italicized where land loss is greater within the terrace field than along the bounding marsh.

Site	Δ Interior (ha/y)	Δ Exterior (ha/y)	Δ Total (ha/y)
1102	-0.082	-1.837	-1.919
<i>2015W</i>	-0.371	2.166	1.795
<i>2015C</i>	0.018	0.244	0.226
<i>2015E</i>	0.099	0.189	0.089
<i>3008</i>	-0.295	-0.272	-0.566
3006	-0.338	-1.462	-1.800
5001	-1.117	-2.816	-3.933
<i>7001</i>	-0.019	1.458	1.439
<i>7006N</i>	-0.660	0.433	-0.227
<i>7006S</i>	-0.357	0.122	-0.235

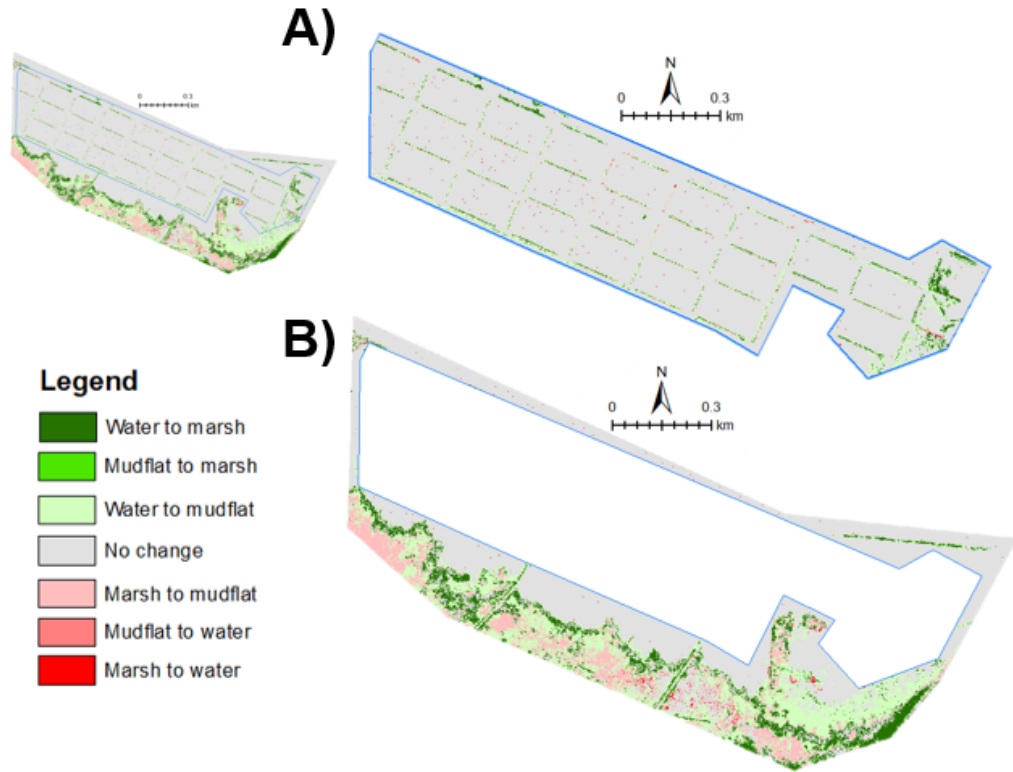


Figure 36. Image analysis of area change observed at site 2015E in the grid terrace field and in the surrounding basin after construction (2007 to 2017). The blue line shows an example of how the limits of the grid terrace field were selected to differentiate between land area change (A) within the terrace field from (B) within surrounding marsh and the water body bounding shoreline.

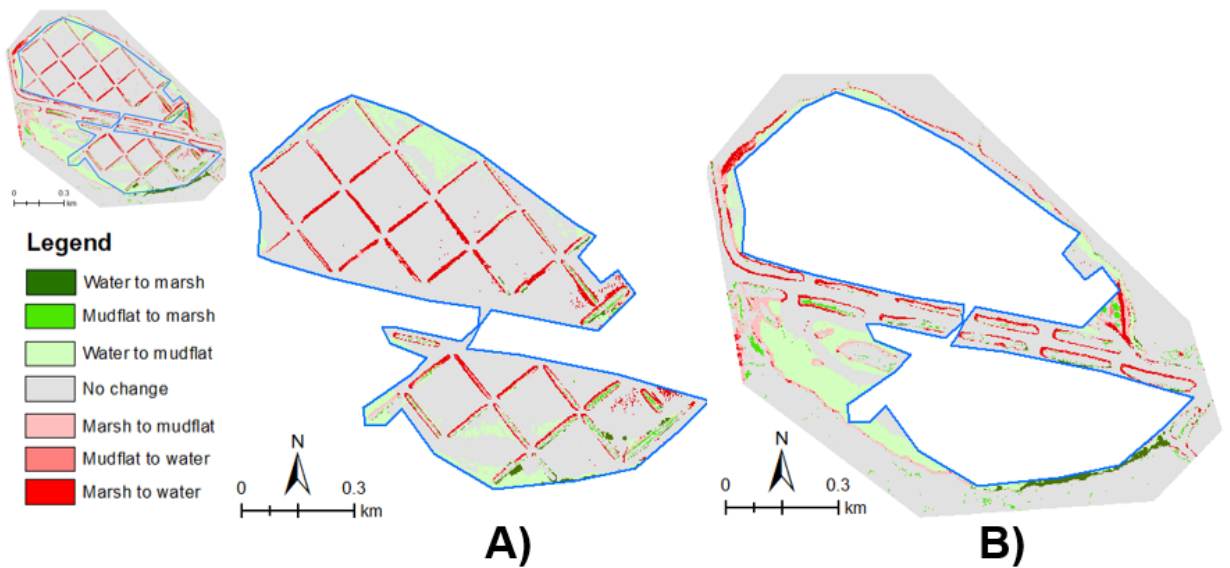


Figure 37. Image analysis of area change observed at site 3008 in the grid terrace field and in the surrounding basin after construction (2005 to 2017). The blue line is a more complex example of differentiating the land area change within and outside the terrace field.

By removing the change occurring within the terrace field and assessing only the change along the bounding marsh shoreline, six sites appear to experience land gain. Earlier analysis, which considered change sitewide, indicated only four sites experienced land gain. Sites 7006N and 7006S indicated net land loss initially, but both suggest net land gain along the bounding marsh shoreline when changes within the terrace field are considered separately.

4.4.3 Classification Accuracy Assessment

Each classified image was subjected to a quality assessment and quality control procedure through the creation and analysis of accuracy assessment points. Through a confusion matrix, a kappa coefficient is calculated by comparing classified and ground-truth values from one image. This value is used as an index of agreement, where values are interpreted as no agreement (≤ 0), none to slight (0.01-0.20), fair (0.21-0.40), substantial (0.41-0.60), and near perfect (0.60-1.00) (McHugh, 2012). For remote sensing analyses, a kappa ≥ 0.70 is considered acceptable (Osorio and Linhoss 2020). As shown in Table 7, all 40 classified images earned kappa scores ≥ 0.60 and are statistically considered to have above the level of “substantial agreement” between the true image and its classified counterpart, and 39 of these 40 had kappa scores ≥ 0.70 , meeting or exceeding established image classification standards (Rwanga et al. 2017). The arithmetic average kappa coefficient for these classified images was 0.858, which is considered as near perfect correlation between the true and classified images. The maximum agreement was measured as 0.961 at the second image for 2015E (Figure 38), while the lowest agreement equals 0.691 at terrace site 2015W in its third image (Figure

39). The complete descriptive statistics of the kappa coefficients are presented in

Appendix B.

Table 7. Kappa coefficient image analysis results for each classified image from each site. Coefficients that are statistically substantial but below the typical geospatial threshold are italicized.

Site No.	Image 1	Image 2	Image 3	Image 4
1102	0.897	0.820	0.904	0.840
2015W	0.889	0.782	<i>0.691</i>	0.930
2015C	0.854	0.814	0.708	0.845
2015E	0.801	0.961	0.797	0.756
3008	0.881	0.891	0.889	0.892
3006	0.870	0.866	0.881	0.917
5001	0.817	0.798	0.854	0.808
7001	0.859	0.838	0.859	0.867
7006N	0.824	0.853	0.942	0.940
7006S	0.910	0.939	0.775	0.917

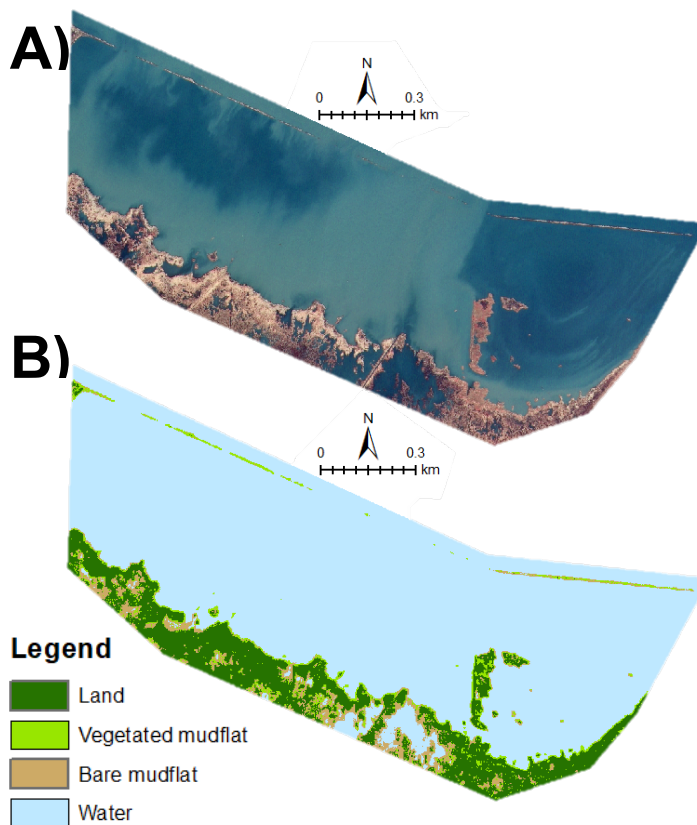


Figure 38. Image analysis of Site 2015E taken in 2005. Image (A) is the true color NAIP imagery. Image (B) is the classified image. Using 100 stratified random accuracy assessment points, the index of agreement between the classification map (B) and the true color image (A) in this example is equal to 0.961. This represents the highest index of agreement across the 40 images analyzed.

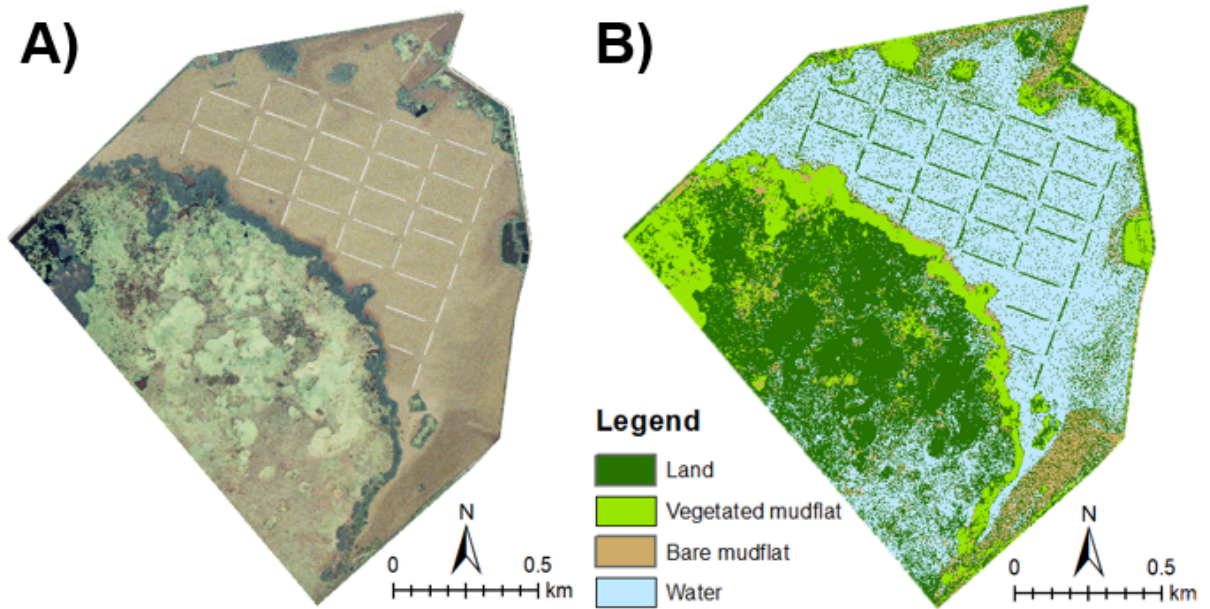


Figure 39. Image analysis of Site 2015W taken in 2007. Image (A) is the true color NAIP imagery. Image (B) is the classified image. Using 100 stratified random accuracy assessment points, the index of agreement between the classification map (B) and the true color image (A) in this example is equal to 0.691. This represents the lowest index of agreement across all 40 images.

4.5 Numerical Modeling of Hydrodynamic Impacts of Terrace Designs

The 12 model runs simulated hydrological and hydrodynamic conditions within a 15 x 15 km basin designed with a small riverine input (10 m³/s) and a coastal tidal signal that mimics that of NOAA tidal gage 8761724 at Grand Isle, LA. The results allowed comparison of hydrodynamic conditions derived from winds, and tidal and riverine input-induced currents with and without terraces (of three different designs). It should be noted that the Delft3D models runs did not utilize the wave module, hence, the results do not include the additional wave-orbital bottom shear stress but do include the direct wind stress-induced current contribution. Sediments are also not included in the model design, but spatial energy characteristics can be used to infer areas of sediment erosion and focusing. Sediment is also indirectly present through the bottom friction coefficients selected to be characteristic of muddy, shallow water bodies in coastal Louisiana.

Within the domain, water velocity was controlled by the riverine (upstream) boundary and the tidal (downstream) boundary as well as the uniformly applied wind. Generally, water velocities within the terrace field decreased relative to the water velocities present in the control (no terraces) regardless of terrace shape. Along the outer edge of each terrace field (the terrace field is defined here as the area of the grid that contains multiple individual terraces) defined by the wind-current direction in the hypothetical basin, water velocities accelerated, producing substantially higher water velocities than experienced in the same location in the control model run (Figure 42-44). Additionally, gaps between individual terraces in the field (that were oriented parallel to the wind direction and aligned between multiple rows), experienced accelerated water velocities as compared to the control (Figures 40-42). However, submerged areas between individual terraces, including the excavation pits, experienced reduced water velocities relative to the control (Figure 40-42). Observed water velocities were highest within the grid terrace field (Figure 41) and lowest within the linear terrace field (Figure 40). The total bed shear stress varies across each simulation with the lowest bed shear stress recorded in the control (no terrace) and the greatest bed shear stress recorded in the grid terrace field (Figure 41). Bed shear stress was lower in the linear terrace field than in the chevron terrace field, as the latter featured regions of relatively high shear stress at the downstream end of its field (Figure 40). Overall, bed shear stress decreased or remained low in areas sheltered between terraces and increased in areas between terraces parallel to the dominate wind direction (Figure 40-42). Edges and corners of the terrace fields – particularly the grid (Figure 41) and chevron (Figure 42) terraces – experienced higher bed shear stress than the same regions of the control.

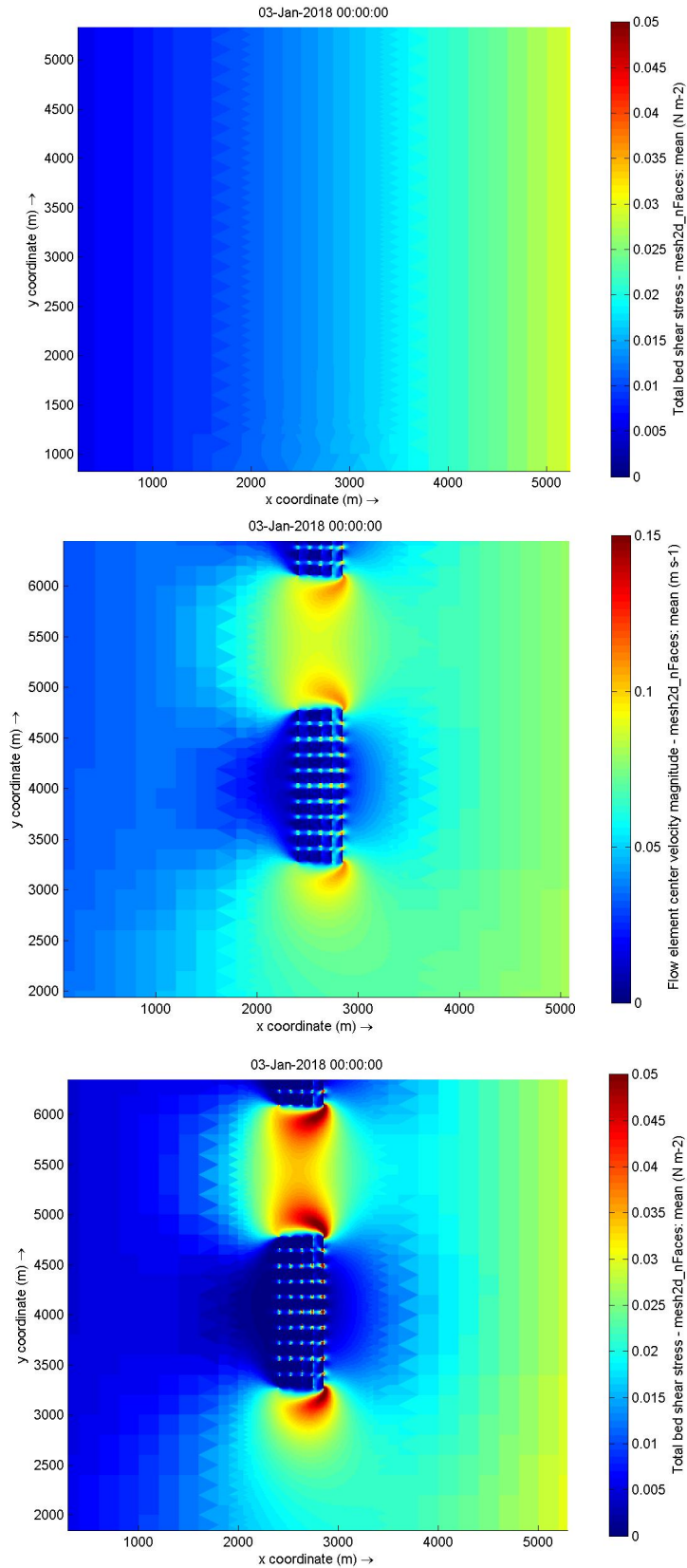


Figure 40. Hydrodynamic impacts of the lower linear terraces. The simulation with no terraces (A) shows the hydrodynamic conditions of the control. Water velocity (m/s) and total bed shear stress (N/m²) outputs illustrate the same trends, so only total bed shear stress is shown for the control. Water velocity (B) and total bed shear stress (C) values are decreased within and behind the linear terrace field, but increase around the downstream edge of the field. The maximum water velocities and total bed shear stress experienced during the control simulation occurred at the third timestep (shown). Impacts from the upper linear field are visible along the top of (B) and (C).

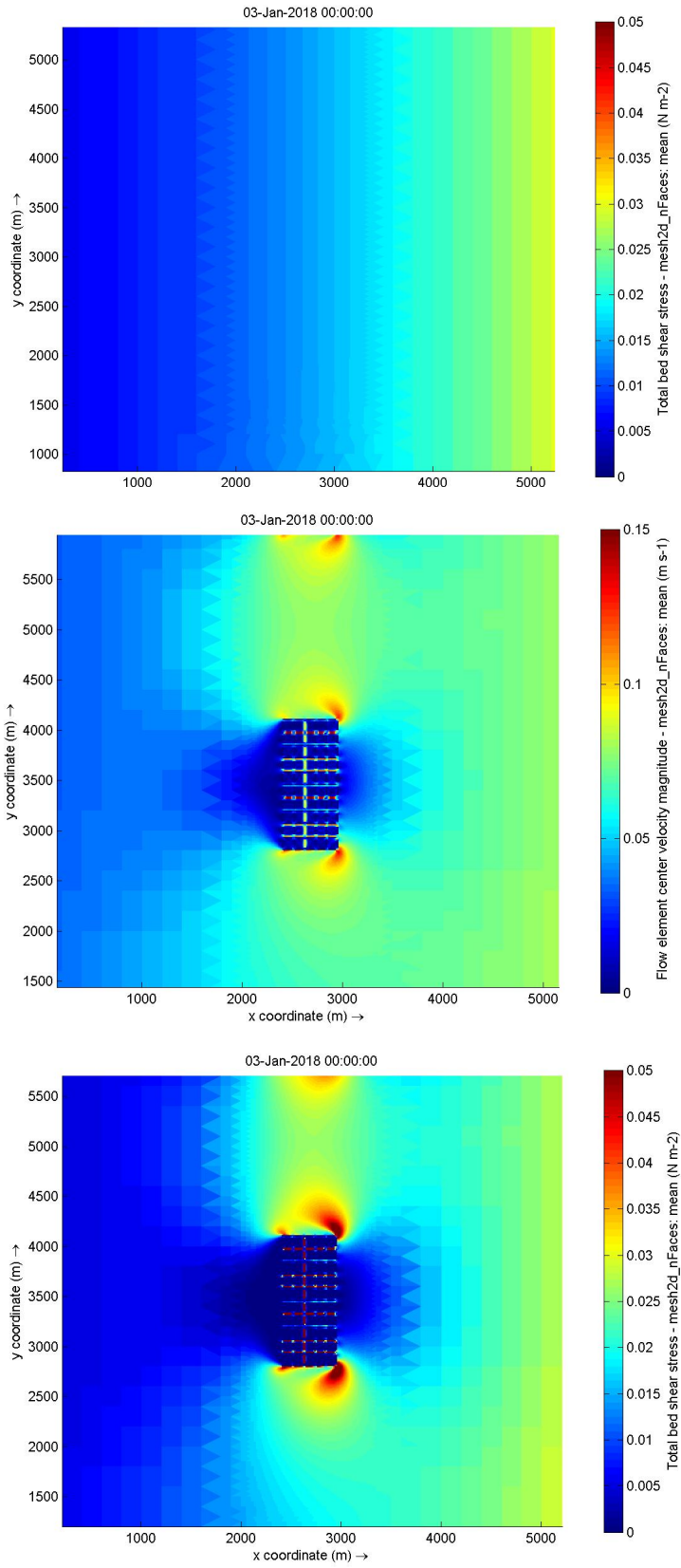


Figure 41. Hydrodynamic impacts of the lower grid terraces. The simulation with no terraces (A) shows the hydrodynamic conditions of the control. Water velocity (m/s) and total bed shear stress (N/m^2) outputs illustrate the same trends, so only total bed shear stress is shown for the control. Water velocity (B) and total bed shear stress (C) values are decreased within and behind the linear terrace field, but increase around the downstream edge of the field. The maximum water velocities and total bed shear stress experienced during the control simulation occurred at the third timestep (shown). Impacts from the upper grid field are visible along the top of (B) and (C).

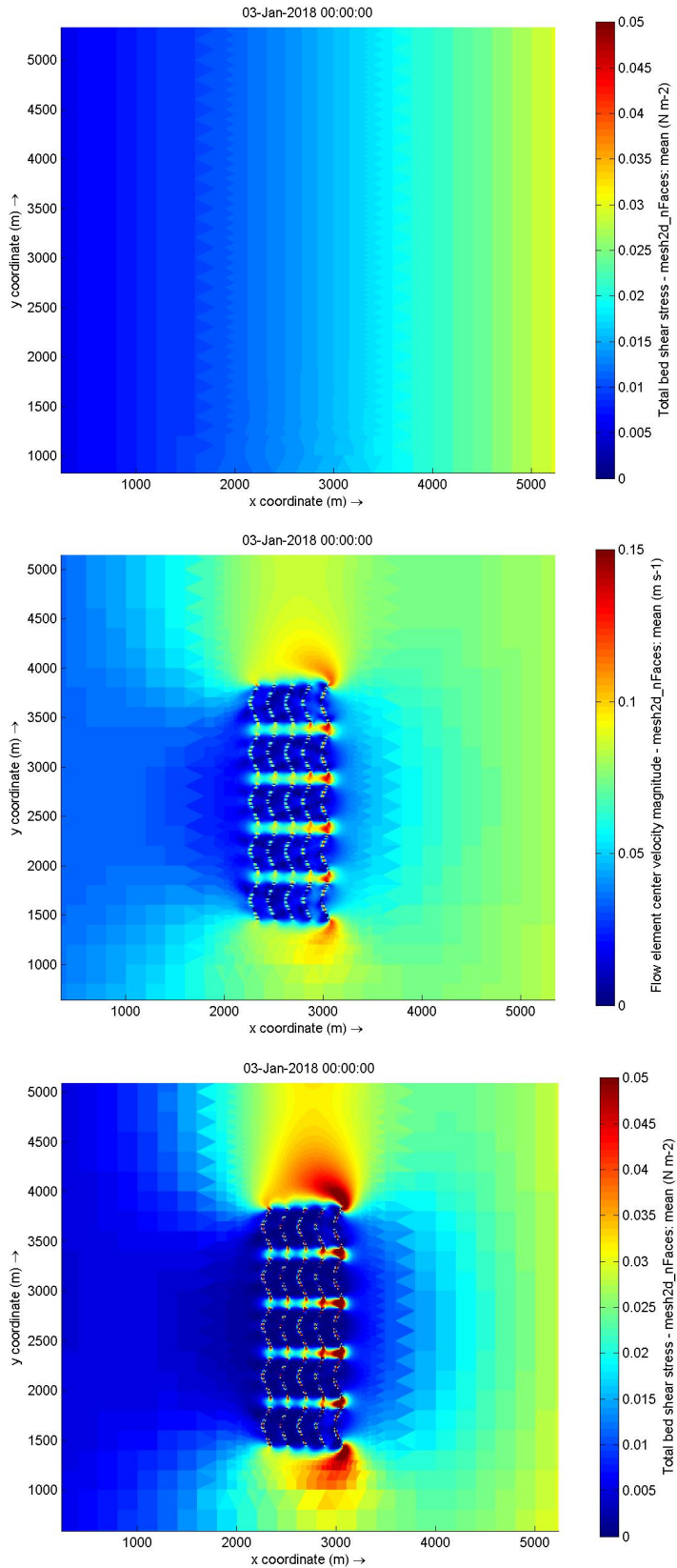


Figure 42. Hydrodynamic impacts of the lower chevron terraces. The simulation with no terraces (A) shows the hydrodynamic conditions of the control. Water velocity (m/s) and total bed shear stress (N/m²) outputs illustrate the same trends, so only total bed shear stress is shown for the control. Water velocity (B) and total bed shear stress (C) values are decreased within and behind the linear terrace field, but increase around the downstream edge of the field. The maximum water velocities and total bed shear stress experienced during the control simulation occurred at the third timestep (shown). Slight impacts from the upper chevron field are visible along the top of (B) and (C).

5. Discussion

5.1 Effect of Marsh Terracing on Nearfield Sediment Deposition and Marsh Stability

Two distinct geomorphic benefits have been proposed for marsh terrace construction projects in Louisiana. The first is that they increase the trapping efficiency of sediment in the water bodies where they are constructed, including from mineral sediment brought in by hydrologic exchange, and from particulate organic matter, both imported and yielded from local marshes. As such, they might reduce elevation loss with RSLR, or even lead to a transition of submerged areas to mudflats that are ultimately colonized by marsh grasses, leading to land gain. The second espoused potential benefit is that they reduce wave-current energy in the water body, reducing erosional loss of marshes bounding the water body.

The results of the present study yield information at the field observational scale about sediment retention that is explored in §5.1.1 below. The remote sensing results are explored for sediment retention and marsh erosional land loss are discussed in §5.1.2 and 5.1.3. A multiparameter assessment is required to gauge terrace success, as terracing projects are implemented for a variety of purposes. Morphologically, marsh terraces are proposed to reduce shoreline erosion by interrupting fetch and reducing wave energy dissipated along the bounding marsh as well as promote increased sediment retention by reducing water velocities within the terrace fields (Brasher, 2015). Thereby, terracing projects are evaluated for their ability to reduce shoreline erosion via wave attenuation and to retain sediment measured by a mudflat development proxy. Factors that co-influence these geomorphic responses include uninterrupted basin fetch, vertical accretion surpluses and deficits (VA_{SD}), hydrologic connectivity, and tropical storm impacts help predict and explain marsh terrace performance. All of these factors can be quantified to examine the context of the field and geospatial analytical results in the present study of sediment retention and marsh shoreline loss. Uninterrupted basin fetch is measured in a given project basin across the longest points leading to or within the basin that are not disrupted by

marsh or other barriers prior to terrace construction. VA_{SD} can be calculated using Equation 1 presented by Jankowski et al. (2017). Hydrologic connectivity is defined by using a proxy for water exchange calculated by the 10-day averaged variance (v) about mean water level derived from water level statistics retrieved from a site's most adjacent CRMS site for the 2017 calendar year. These values then group each site as having low ($v < 0.005$), intermediate ($0.005 < v < 0.015$), or high ($v > 0.015$) hydrologic connectivity. Hydrologic connectivity – its calculations, application, and considerations – are discussed in Appendix D regarding its use in this study. Tropical storm impact can also be considered as to whether they bring at least tropical storm force winds to the project site with a given time after terrace construction (six months is used herein, as the material comprising terrace ridges needs several months to consolidate and their integrity is likely compromised by large storm surges from strong tropical storm events (Morton and Barras, 2011; Ducks Unlimited, personal communication, 2018).

5.1.1 Sediment Deposition Patterns in Terrace Fields and Implications for Marsh Emergence

The short-term (days to months) vertical deposition rates measured from feldspar marker horizons (FMHs) at Bayou Monnaie and Yankee Canal, and derived from ^7Be activities at Bay Alexis, indicate that there is significant sediment trapping occurring on the marsh terraces and within subaqueous areas contained within the terrace field during the Winter-Spring period. Deposition rates vary spatially, and a relationship exists between deposition rate and elevation (measured to NAVD88; Figure 24). The only plots to display no accretion during the study intervals were located on the apex (crown) of the terrace ridge – the region on the terrace with the highest elevation and lowest submergence frequency. Despite washouts (which exclusively occurred at shoreline

FMH plots) that are likely due to wave effects at the shoreline, terraces at Bayou Monnaie and Yankee Canal recorded their highest accretion values at vegetated, near-shoreline/edge plots—rates that ranged from 9 to 14 mm on the three studied terraces at Bayou Monnaie and from 3 to 6 mm on the six terraces sampled at Yankee Canal. There is a clear inverse linear relationship between accretion and elevation to NAVD88 (Figure 24). These results are consistent with previous studies that recognize a direct relationship between sediment deposition and inundation frequency in natural coastal marshes in coastal Louisiana (Christiansen et al. 2000; Andersen et al. 2011; Butzeck et al. 2015). Lower elevations equate with greater frequency of submergence (i.e., inundation frequency), and this allows both higher organic production rates (due to nutrient fluxes) and higher rates of mineral trapping from particulates brought into the nearfield water body by tidal and wave-driven currents. All sampled plots were in areas vegetated by *Spartina alterniflora*, which likely indicates a strong trapping induced by the dense network of stems and leaves (Ranwell, 1964; Gleason et al. 1979; Li and Yang, 2009; Olliver et al. 2020). It can be anticipated that since these measurements were made during the strong winter-spring frontal period that causes resuspension in the Bay systems of coastal Louisiana (Carlin et al. 2016) that are hydrologically connected to the terrace water bodies, that these are maximum rates of mineral deposition annually. This supports earlier sediment trap work in Louisiana coastal marshes (Reed, 1989).

In submerged parts of the terrace field (i.e., those areas contained between and immediately outside of the terraces), ⁷Be deposition rates as measured in 2020 at Bay Alexis also showed evidence of elevation control. As these rates were collected during

the winter-spring frontal period and during a period of high Mississippi River discharge, they also likely represent seasonal maxima in mineral supply rates.

Total deposition rate in submerged areas of the three study terrace fields since terrace construction can also be determined using the distinct core stratigraphy of the post-construction layer—marked by significantly higher porosity and a distinctly different organic content (higher or lower depending on the site) than underlying, pre-construction sediment. At Yankee Canal, the distinct high-porosity and high organic content surficial layer ($\phi = 0.75$ to 0.91 , $\text{LOI} = >10\%$) in submerged area cores is interpreted as the post-construction deposit. The underlying lower porosity ($\phi = 0.54$ to 0.75) material, which precedes terrace construction, tends to be lower organic content ($\text{LOI} = <10\%$) with a lighter grey color that is distinct from the surficial dark brown layer interpreted as post-construction (Figure 31-32). The facies transition (from high porosity, organic-rich to low porosity, organic-poor) occurs at a shallower depth in the northern field than in the southern field; the post-emplacment layer averages 14.5 cm in the South field and 2.7 cm in the North field. Given that both fields were constructed fairly closely in time in late 2015, this difference is interpreted as being due to the lower hydrologic connectivity of the North field with larger water bodies like Barataria Bay (Figure 11) that contain relatively high suspended sediment concentrations. Within the two fields at Yankee Canal, excavation pits have the thickest post-emplacment layer; approximately 24.5 ± 1.0 cm in the South terrace field and only 5 ± 0.0 cm in the North. Pit deposition totals exceed those in the six cores sampled from the plateau areas by an average of 6.4 cm. Pits are located approximately 10 m from their terrace with plateaus occurring on either side of the pit. The average elevation of the excavation pits sampled

at Yankee Canal is -148 cm NAVD88, while the average plateau elevation is -72 cm NAVD88. Since terrace construction was completed in late 2015, the post-placement layer is 4.5 years old, as sampling occurring in early 2020. Therefore, deposition rates in the South field average 5.2 ± 0.2 cm/y in excavation pits and 2.0 ± 0.3 cm/y on plateaus. In the North field, deposition rates average 1.1 ± 0.0 cm/y in excavation pits and 0.3 ± 0.3 cm/y on plateaus. Together this evidence suggests that mineral and detrital organic matter trapped in the submerged areas of the fields is preferentially focused in the lowest elevation pit areas. Additionally, remote sensing analysis of Yankee Canal indicated very little (-0.001 ha/y) wetland erosion in the North field during the post-construction era (after 2015), while change in the South field showed significant wetland loss (-0.113 ha/y), including the erosion of the terraces themselves that are facing the direction of maximum wave fetch. This suggests that, in addition to more hydrologic connectivity in the South field, deposition rates in submerged areas of that field were magnified by sediment recycled from erosion of the terraces and surrounding shoreline yielding both mineral and organic particulates.

At Bayou Monnaie, the post-placement layer in cores was characterized by low porosity ($\phi < 0.85$) and low organic content ($\leq 30\%$), while the material immediately underlying this, and interpreted as pre-construction was high porosity ($\phi > 0.85$) and organic rich ($>30\%$ LOI). This reverse porosity trend at depth is attributed to the higher organic content of the pre-construction layer: the distinct difference between these two layers still allows attribution as the pre- and post-construction stratigraphy. Deposition rates were highest in the deepest pits excavated for terrace construction and exceeded 24 cm (> 5.3 cm/y) in the four examples sampled. This again suggests sediment focusing in

the deepest subaqueous areas. In cores collected from the center plateaus between terraces at Bayou Monnaie, which were minimally disrupted by excavation during construction (i.e., disruption was limited to excavator placement but no material was dredged or redistributed), the post-construction deposition is only 2 to 5 cm thick (0.1 to 0.4 cm/y). The observed post-construction deposition rates at Bayou Monnaie are similar to those at Yankee Canal South (or even higher in the pits since the bottom of the post-construction deposit was not defined by coring). Both sites are considered intermediately connected by the water level variance ($v_{BM} = 0.0182$; $v_{YC} = 0.0139$) measured at each local CRMS station.

Only one transect of cores was collected from Bay Alexis extending from a terrace to a central plateau that can be used to define the post-construction submerged deposition rates. This transect included only one excavation pit core. Post-construction deposition in that excavation pit, which took the form of a low porosity ($\phi < 0.65$) medium to coarse silt, was the highest observed in the three sites (> 34 cm thick as the core was not long enough to penetrate to the low porosity pre-emplacement layer). This core was collected from the Old terrace field, which was completed in 2005, so the annual deposition rate is > 2.3 cm/y. As at Bayou Monnaie and Yankee Canal, the limited sampling at Bay Alexis showed lower deposition rates in the central plateaus (mean = 2 cm or 0.1 cm/y) relative to the excavation pit sampled. Three other cores, two from central plateaus and one from a New terrace excavation pit, were also collected, but did not form a complete transect. In the New terrace field, stratigraphy-derived deposition rates are also greater in the excavation pit (4.4 cm/y; 20 cm over 4.5 years as construction was completed in 2015) than in central plateaus (1.4 ± 1.2 cm/y).

Additionally, ^7Be -derived results from submerged core sites support higher deposition rates in excavation pits over central plateaus: excavation pits (2 cores) across both terrace fields record an average unconsolidated deposition rate of 0.06 ± 0.01 mm/d and the central plateaus (3 cores) record an average unconsolidated deposition rate of 0.04 ± 0.04 mm/d. This difference is also discernible in total integrated inventories, where excavation pits average 1.5 ± 0.08 dpm/cm² and central plateaus average 1.4 ± 1.1 dpm/cm².

The inverse relationship of post-construction deposition rate with NAVD88 elevation observed from core stratigraphy and ^7Be /feldspar data at all three field sites, excepting the highest elevations of the terraces themselves, is marked by differences in porosity and organic content characteristic of taking place in coastal settings after a significant environmental change (Ward et al. 1998). This involves both a re-organization of the hydrologic connectivity of the system, a reduction in hydrodynamic energy (see §5.3), and spoilage from the excavation of *in situ* material. The greater accumulation measured in the deeper excavation pits is consistent with sediment focusing (Likens and Davis, 1975) and is a spatial pattern observed by many other studies (Wilson and Opdyke, 1941; Deevey, 1955; Lehman, 1975). Sediment migrates from regions of high energy (erosion to low deposition) to regions of low energy (deposition), and as is illustrated in Figures 40-42, the total bed shear stress is lowest in the regions immediately adjacent to the terraces – the excavation pits. These modelled regions of lower energy correspond to the field-determined locations of excess sedimentation, supporting the explanation of sediment focusing.

Marsh terraces constructed above the mean tide level have been rapidly shown to colonize with vegetation, which aids in particle trapping, supporting the cost-effective perimeter planting of sprigs pervasive in marsh terrace construction (Steyer, 1993; Castellanos and Aucoin, 2004; Thibodeaux and Guidry, 2009; Miller and Aucoin, 2011; Hymel and Breaux, 2012; McGinnis et al. 2012). The question emerging from the field studies at Yankee Canal, Bayou Monnaie and Bay Alexis is whether the observed deposition rates will be sufficient to result in emergent marsh beyond the initial boundaries of the terraces themselves. Spatially, sediment accumulation is focused in the excavation pits and along existing vegetated areas, but neither particularly supports subaerial marsh emergence through expansion of the terrace footprint (prograding laterally). While, as shown in Table 8, stratigraphy-derived deposition rates exceed RSLR in excavation pits at each field site, which is an essential component of marsh building and sustainability (Jankowski et al. 2017). These rates will decrease as the pits infill and reach an elevation equilibrium with the central plateaus (plateau areas are likely only keeping pace or losing elevation to RSLR). This will tend to reduce bathymetry differences in the submerged areas, but at least in the three fields studied, are unlikely to result in sufficient sediment trapping to result in marsh emergence.

Table 8. RSLR rates at each adjacent CRMS site and the average excavation pit (maximum) & central plateau (minimum) deposition rates derived from stratigraphy at each field site (data derived from Jankowski et al. 2017). *Bayou Monnaie is represented by the next closest CRMS station (0386) as 0387 is unavailable in the dataset. RSLR is highly spatially variable.

Field Site	CRMS Station	RSLR (cm/y)	Dep. Rate, Pit (cm/y)	Dep. Rate, Plateau (cm/y)
Bayou Monnaie	0386*	2.75	> 5.33	0.4
Yankee Canal	6303	1.78	3.85	0.1
Bay Alexis	2614	2.05	> 2.34	0.2

5.1.2 Geospatial Evidence for Increased Sediment Retention

As is evident in the remote sensing results, changes occurred within and around the terraced sites beyond marsh land gain and land loss. The conversions into and from the 2 subclasses – vegetated mudflat (floating vegetation), a subclass to land, and unvegetated (bare) mudflat, a subclass to water – provide insights into the processes influencing each terraced basin before and after terrace construction that do not constitute true marsh land gain or loss; these changes are more transitional in nature. Tables B1 and B2 display all class changes at each site (Appendix B). Vegetated mudflat is defined here as areas that are not colonized by marsh grasses but by floating or submerged aquatic vegetation, and hence, are likely at lower elevations than conditions needed for classification as land. As presented by Westphal and Nakashima (2019), (bare) mudflats may lead to land development if vertical accretion outpaces RSLR to allow for subaerial emergence and colonization by marsh grasses. Additionally, considering the relatively short time period assessed by this remote sensing study, these intermediate (subclass) changes may be more measurable than changes that rely on slower processes (e.g., land gain). Mudflat development, which is defined by the conversion of water into either vegetated or unvegetated mudflat, is outlined for each remote sensing site in Table 9. It is important to note that mudflat presence, especially in aerial imagery, is heavily dependent on water level, and reliable water level statistics do not exist for each site at the time of each image acquisition (as early as 1989 prior to the inception of the CRMS monitoring station program in the early 2000s). Therefore, some changes in mudflat extent between image dates may be attributable to water level fluctuations in the compared images. The assessment of vegetated mudflat development may also be

contaminated by the presence of detached (floating) vegetation (e.g., water hyacinth) that is typically present in Louisiana coastal marshes and is indistinguishable in aerial imagery or by the classification schemes used herein. Therefore, vegetated mudflat development is presented for each site (Table 9), and nine of the 10 sites studied showed an increase in areal extent after terrace construction, but it is not evaluated toward the determination of marsh terrace success or performance. In addition to the random aspect of floating aquatic vegetation, any reduction in hydrodynamic energy caused by terrace barriers in the water body presumably would increase the likelihood of the basin storing floating aquatics.

Table 9. Conversion of water to vegetated mudflat and unvegetated (bare) mudflat across 10 remote sensing study sites measured in ha/y. Blue indicates increased mudflat development following terrace construction (i.e., increased water to mudflat conversion after terrace implementation).

Site	Vegetated Mudflat		Unvegetated Mudflat	
	Δ Before	Δ After	Δ Before	Δ After
1102	0.013	0.110	0.000	0.315
2015W	0.112	0.176	0.004	0.052
2015C	0.046	0.050	0.069	0.411
2015E	0.132	1.153	0.075	0.545
3008	0.005	0.585	0.568	0.367
3006	0.769	0.187	1.064	0.059
5001	0.000	3.992	3.375	1.338
7001	0.170	0.576	0.519	1.020
7006N	0.012	2.601	0.242	0.509
7006S	0.003	0.132	0.029	0.159

Distinct from vegetated mudflats are unvegetated or bare mudflats. These mudflats may be periodically exposed by fluctuating water levels, but unlike vegetated mudflats, they are distinguishable from floating vegetation. Following the remote sensing methodology presented by Westphal and Nakashima, 2019, unvegetated mudflats were classified as a subclass to water as they are either always submerged or infrequently

exposed. Seven of 10 remote sensing sites showed evidence of greater water to unvegetated mudflat conversion following terrace implementation (Table 9). Of the three remaining sites, all recorded some conversion from water to unvegetated mudflat. Hence, all 10 remote sensing study sites show evidence of stepwise elevation gain that might lead eventually to emergent marsh from unvegetated mudflat growth, suggesting at least partial success in meeting the geomorphic criteria for judging marsh terraces as successful as proposed by Brasher (2015) and others (e.g., Steyer 1993; Turner and Streever, 2002; Nyman and Chabreck, 2012). The accumulation of sediment as unvegetated mudflat and the resulting conversion of water to unvegetated mudflat patterns are supported by the reduced total bed shear stress within the terrace fields (see §4.4), as sediment migrates from regions of high energy (erosion) to regions of lower energy (deposition). The presence of marsh terraces reduces the energy within the terrace field (Figures 40-42), thus creating more favorable conditions for sediment accumulation, unvegetated mudflat growth, and eventual marsh emergence if the vertical accretion outpaces RSLR. By reducing water velocities and total bed shear stress, terraces encourage the deposition and retention of material that would otherwise be mobilized through (and out of) the system.

Linked to the exchange into and out of a system is hydrologic connectivity, which appears to play a role in governing terrace performance regarding sediment retention. As mentioned previously, as a terraced water body exchange with external waterbodies increases, it is presumed that the amount of sediment removed from the system increases as well. Therefore, sites with high hydrologic connectivity are more likely to lose land or mudflat building material to external sinks, which tracks with the three sites that do not

illustrate mudflat development following terrace construction as they all have high hydrologic connectivity. Of the seven sites that do show increased mudflat development, six (86%) have low or intermediate hydrologic connectivity (Table 10, Table D1); these lower hydrologic connectivities suggest less water exchange, likely resulting in less sediment loss as well. The CRMS stations used to calculate hydrologic connectivity were either not located in the same basin as the remote sensing study sites or not activated prior to terrace inception, precluding a comparison of hydrologic connectivity before and after project construction. Further studies are necessary to determine if terraces impact the hydrological connectivity, but this study suggests hydrological connectivity may be a consideration prior to the installation of a terracing project as sites with lower hydrological connectivities appear to achieve better terrace performance respective to increased sediment retention. While not explored in the current study, an additional consideration essential to future investigation and discussions of hydrologic connectivity is the astronomical tidal regime of each site, as dominant ebb or flood conditions would likely impact sediment transport within the basins.

5.1.3 Reduction of Bounding Shoreline Marsh Erosion

Six of 10 remote sensing study sites illustrated either a reversal or reduction of erosion (land loss) or an increase in aggradation (land gain), which indicates successful terrace performance (Table 6). Land loss was determined by the conversion of marsh class to any other class (vegetated mudflat, bare mudflat, or water), and land gain was defined as the conversion of any class to a distinguishable marsh class. Following terrace construction, two sites – 2015W and 2015C – showed an erosion reversal, two sites

(7006N and 7006S) indicated a decrease in rates of land loss, and sites 2015C and 7001 recorded increased rates of marsh gain. Of the remaining four sites, 1102 and 5001 indicated a reversal of land gain to net erosion and 3006 and 3008 show increased rates of land loss after terrace construction. The present (mixed) results are consistent with those presented by recent remote sensing studies Osorio and Linhoss (2020) and Westphal and Nakashima (2019) as the former found 55% of terrace projects to be successful while the latter found 60% to perform positively. Both studies featured randomly selected terracing sites across coastal Louisiana with Osorio and Linhoss (2020) as the largest study, having examined 20 terrace fields. Osorio and Linhoss (2020) is limited in its comparability to the current study as the former only measured changes within the terrace fields (interior) and did not assess changes along or within the bounding marsh. Westphal and Nakashima (2019) assessed five study sites but did not measure the change within the terrace field separate from the change along the bounding marsh. Rates of change varied spatially within each of the 10 study sites assessed by the present study, suggesting that the comparison of change within the interior to the change along the exterior is an important advancement from these previous studies.

Table 10 is an examination of the quantified potential drivers of bounding shoreline edge erosion. Of the six sites that indicated positive terrace performance regarding a reduction of land loss, four (67%) indicate a reversal from land loss to net gain or the reduction land loss rates along the bounding marsh shoreline. Two of these sites (2015E and 7006S) exist in basins where wind-waves may be capable of eroding marsh edge, as uninterrupted fetch nearly reaches or exceeds 4 km at each site (Table 10; Allison et al. 2017). Initially, the entire basin at 7006S appeared to be eroding at -0.235

ha/y following terrace construction; however, assessing the terrace field (interior) separately from the bounding marsh (exterior) indicated the terraces were eroding faster (-0.357 ha/y) while the bounding marsh had reverted to land gain (+ 0.122 ha/y). This occurrence at 7006S highlights the importance of distinguishing the terrace field from the bounding marsh, as the sitewide rate of change oversimplifies the origin of land area changes occurring within the basin. Additionally, this introduces a consideration for assessing terrace performance and subsequent success; although the site recorded net erosion, this land loss is most concentrated along the terraces, meaning the terraces are operating in a sacrificial capacity to allow the bounding marsh to rebound. As evident at 7006S, marsh terraces may not be perpetual shoreline erosion reducers, but they may allow the natural marsh to grow at a rate it could otherwise not achieve during the period they remain as energy buffers.

In addition to 7006S and 2015E, Site 5001 exists within a basin large enough for fetch to produce erosive wind-waves (Table 10). However, unlike 7006S and 2015E, 5001 does not indicate successful terrace performance as its land gain (1.783 ha/y) reverted to a loss rate of -3.933 ha/y, which is the greatest annual loss experienced at any of the sites examined in this study. Over the period of study, the Jaws (5001) lost land at a rate of 1.117 ha/y within the terrace field and at a rate of 2.816 ha/y in the bounding marsh, indicating that while the terraces may be acting in a sacrificial capacity, they are not creating conditions favorable for marsh growth along the adjacent marsh. Further, unlike the terraces at 7006S and 2015E, which provided evidence of successful terrace shoreline erosion reduction performance by interrupted fetch and reducing wave energy, the terraces at the Jaws were not constructed with traditional excavation pits adjacent to

the terraces. Instead, the terraces at the Jaws were constructed with material dredged from the Gulf Intracoastal Waterway and Charenton Drainage Ditch, both of which feed into the Jaws basin (CWPPRA). The dredging and deepening of these input channels would have altered the hydrologic regime in the Jaws basin and likely results in increased water velocities following through the terrace field area. With higher water velocities, more material is mobilized and transported through the system. Bed shear stress also increases, tending a system more toward erosion than deposition or retention. In addition to removing material for marsh accretion, these higher velocities entering into the 5001 basin may have also increased energy dissipated along the bounding marsh shoreline, leading to the shoreline erosion and retreat illustrated at the Jaws (Figure 35). The potentially overwhelming hydrodynamics of the Jaws are reflected in its very high hydrologic connectivity, which suggests substantially more water exchange than any other site in this study. This is also consistent with Day et al. (2000) findings that marshes with high density of channels (i.e., high hydrologic connectivity and water exchange) experience greater land loss. Individual site hydrologic connectivity values are provided in Appendix D.

Three sites (1102, 3008, and 3006) that do not show decreased shoreline erosion (Table 10) are located within basins insufficiently large to reach the 4 km fetch minimum as described by Allison et al. (2017). Thereby, it is unlikely these terracing projects were installed to reduce shoreline erosion caused by wind-waves. Instead, these basins are likely eroding due to subsidence and pond expansion, which terraces are neither designed nor proposed to combat directly. Each of these sites recorded a vertical accretion deficit (VA_{SD}), indicating shallow subsidence, deep subsidence, and sea level rise are greater

than the vertical accretion (Table 10; Equation 1). Unable to outpace RSLR, these sites may face increased inundation and eventually permanent submergence despite the installation of terraces. This vertical accretion deficit may be linked to the high hydrological connectivity at each site as their water level variances all suggest high hydrologic connectivity and subsequently extensive water exchange throughout each system. If high rates of water exchange are occurring within the system, then it is presumed that high amounts of sediment are being removed by exiting waters. This assumption dominates the opposite possibility, where enhanced hydrologic connectivity allows for increased sediment import, because most terracing sites are in basins relatively isolated from significant sediment sources.

Table 10. Factors impacting terrace performance against overall success of terracing at each remote sensing study site in reducing bounding shoreline marsh loss. Maximum uninterrupted basin fetch (< 4 km = X, ≥ 4 km = ✓), VA_{SD} rates (surplus = S, deficit = D), hydrological connectivity (connectivity), and tropical storm impacts immediately following construction (storms) for each site are provided to help predict or explain marsh terrace performance, and quantitative distinctions are available in Appendix D.

Site	Success	Fetch	VA_{SD}	Connectivity	Storms
1102	X	X	D	high	intermediate
2015W	✓	X	S	low	low
2015C	✓	X	S	low	low
2015E	✓	✓	S	low	low
3008	X	X	D	high	high
3006	X	X	D	high	high
5001	X	✓	D	high	high
7001	✓	X	D	low	low
7006N	✓	X	D	intermediate	low
7006S	✓	✓	D	intermediate	low

5.1.4 Role of Tropical Storms

Tropical storm events may be an important factor governing terrace performance. Major tropical storm events (hurricanes) can be destructive to natural coastal wetlands (Michener et al. 1997; FEMA, 2015; Hauser et al. 2015), so their impact is presumed similar for manmade features constructed of the same materials. The impact of hurricanes on specific terrace projects has been well documented by aerial photography captured after storm passage as well as from Federal Emergency Management Agency (FEMA) reports. As documented by both imagery and several FEMA reports, the “Old” 70-terrace project at field site Bay Alexis was decimated following the historic Category 4 Hurricane Katrina that made landfall in August 2005 several kilometers away (Figure 43A). Aerial imagery also shows a similar impact at the Belle Isle Lake terrace project (remote sensing study site 3008; Figure 37) after the passage of major storm Hurricane Rita in September 2005 (Figure 43B). Although these storm events may deposit substantial amounts of sediment or other land building materials (Cahoon et al. 1995; Reed, 2002; Tweel and Turner, 2014), they appear to be detrimental to overall extent of the subaerial terraces land area, particularly when they pass during the essential first months of terrace ridge consolidation. All four remote sensing study sites that did not indicate positive terrace performance (Table 10) and were rated as unsuccessful projects in the present study (1102 – Hurricane Lili, 2002; 3008, 3006, 5001 – Hurricane Rita, 2005) were directly impacted by hurricanes within six months of project completion. None of the successful terracing projects assessed herein as successful for reducing or reversing basin marsh loss (see §5.1.1 and §5.1.2) experienced nearby passage of a major hurricane within the first year of their placement. The excessive wind, rainfall, and storm surges associated with hurricanes likely overwhelm the freshly completed, inadequately

settled terrace ridges, compromising their long-term integrity by disrupting their essential initial consolidation. Some sites, like the older terrace field at field site Bay Alexis and both fields at remote sensing site 3008 (Belle Isle Lake), never completely recover from hurricane impacts (Figure 44). Over 15 years after the passage of Hurricanes Katrina and Rita, both the Bay Alexis Old field and Belle Isle Lake sites still appear inundated in remote sensing imagery and are likely permanently submerged.

Hurricanes are natural disasters common to the northern Gulf Coast. Since they are generally unpredictable and are expected to increase in intensity over time (Ting et al. 2019), hurricanes are an unavoidable component of the southern Louisiana climate that must be considered when embarking on coastal restoration efforts across the state. The impact of hurricanes on juvenile terracing projects indicates terraces should be constructed with ample time to consolidate before the potential passage of a major tropical storm event. Currently, terracing projects are generally completed during the spring and summer; however, these construction periods are either at the beginning or through the middle of the Atlantic hurricane season, which extends from June 1 to November 30 each year. To allow terraces adequate time to consolidate and potentially increase their ability to withstand the conditions caused by a major tropical storm event, construction should be considered to be completed earlier—such as from November to February. Although the correlation between terrace success and storm passage is limited and further studies are required to further illuminate the legitimacy of this relationship, there appears to be a strong connection and adjusting construction schedules may prove to be a simple, low-cost consideration to improve the overall success of marsh terracing projects across coastal Louisiana.

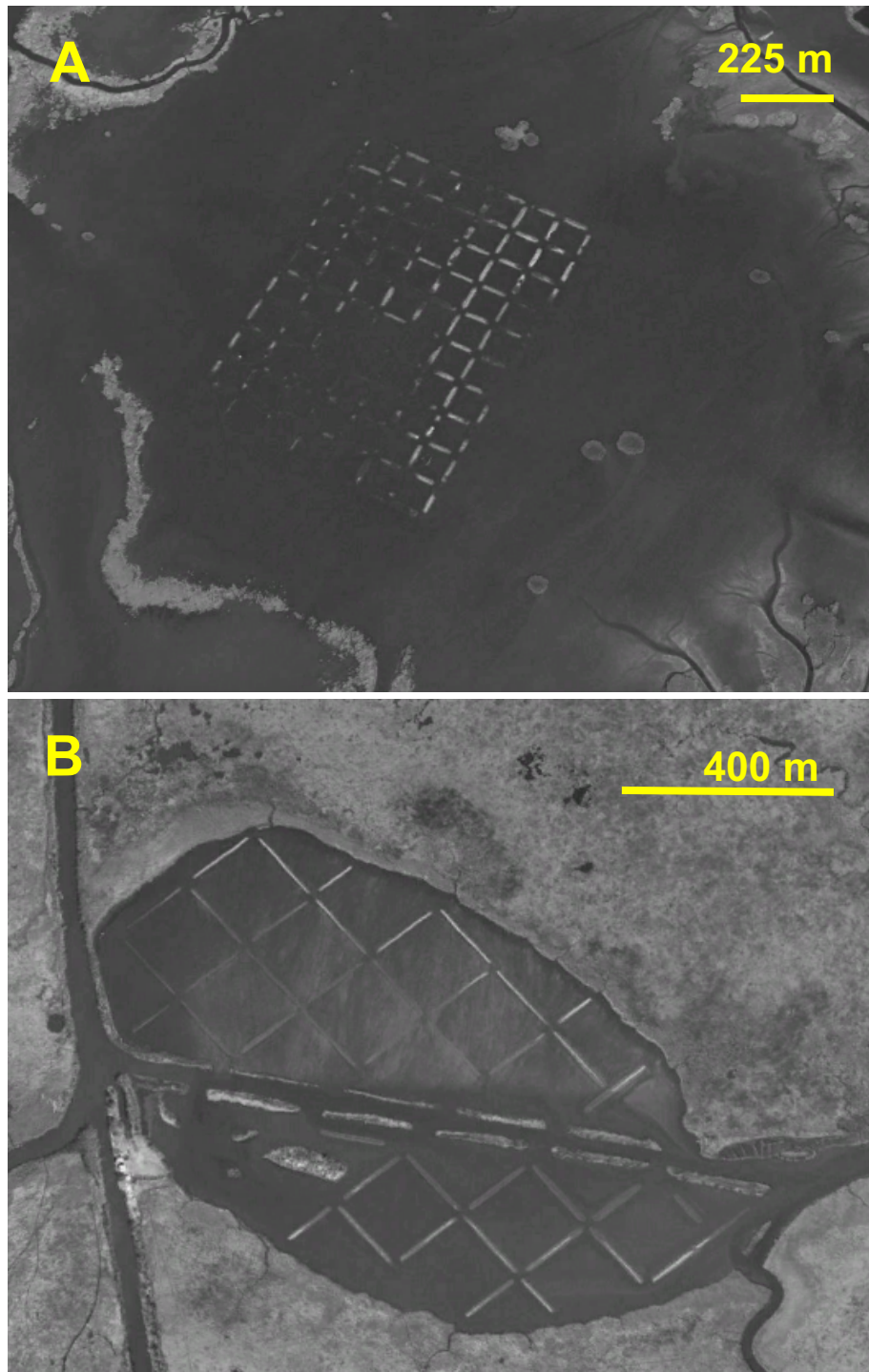


Figure 43. Impacts of hurricane passage on recently constructed terracing projects. A) Field site Bay Alexis following Hurricane Katrina. B) Remote sensing site 3008 (Belle Isle Lake) following Hurricane Rita. Both images capture the inundated terraces in October 2005, less than two months after both storms struck Louisiana.

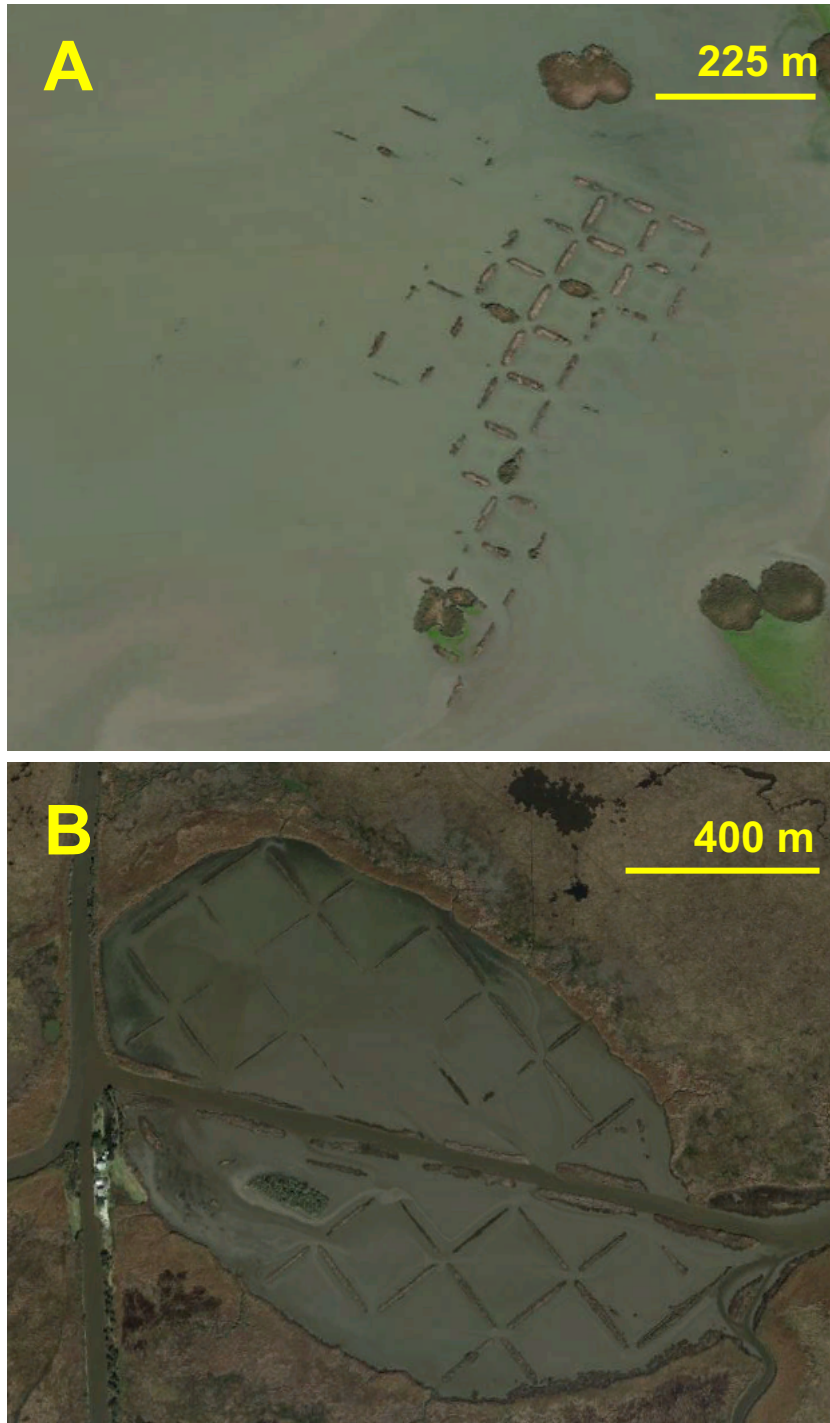


Figure 44. Long-term impact of hurricane passage on terracing projects. A) Field site Bay Alexis in January 2015, almost 10 years after Hurricane Katrina. B) Remote sensing site 3008 (Belle Isle Lake) in January 2016, over 10 years after Hurricane Rita. Both terrace projects were struck by major hurricanes within six months of their construction and the terraces remained inundated for over a decade.

5.2 Insights into Terrace Geometry and Orientation on Performance

5.2.1 Terrace Geometry

The most prominent hydrodynamic effect observed in the modeling runs was the acceleration of water velocities, and thereby total bed shear stresses, around the edge of the terrace field (Figure 40 to 42). Acceleration occurs as flow velocity changes along a streamline, leading to larger velocity vectors around the edge of a structure (terrace). This phenomenon is also illustrated along the edges of individual terraces within the overall field as more localized flow is also accelerated upon interaction with the elevated terraces (Figures 40 to 42). As water velocities increase, total bed shear stress increases because there is increased force (friction) acting against the bed. Although sediment was not part of the modeling, it can be assumed that these areas of increased total bed shear stress would lead to localized bed erosion during high energy (frontal and tropical storm) events. This sediment would then be focused, as observed in the field results, into lower energy areas such as the excavation pits, into adjacent marshes (including terraces), or exported out of the field.

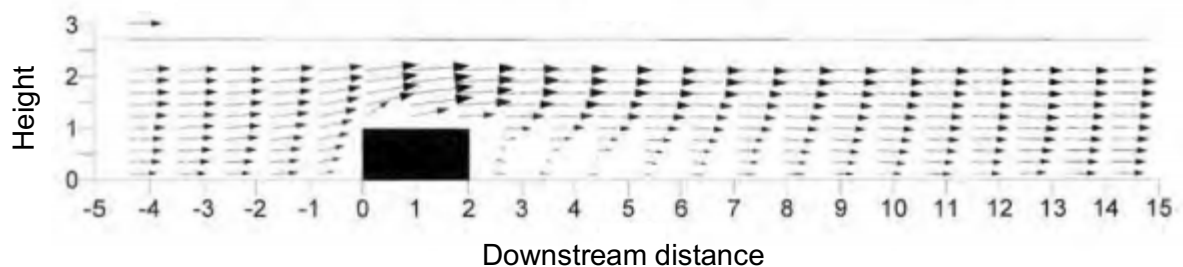


Figure 45. Mean velocity field around an impermeable ($\Phi = 0$) structure modified from Chan et al. (2012). Approaching velocity vectors are lifted along the upstream side of the structure then recirculate in a region some distance downstream. As concluded by Chan et al. (2012), the distance to this recirculation region increases as structure permeability increases due to bleed flow.

Model results also show evidence of a cone-shaped energy reduction zone (both water velocity and bed shear stress) downstream of the predominant wind-current forcing orientation (Figure 40-42). This zone has its greatest lateral extent (y-direction width) immediately behind the terrace field and thins in the downstream direction to ends within ~500 m of the terrace field. As shown in Figure 45 (modified from Chan et al. 2012), the velocity vectors are initially lifted by the terrace field (structure) and settle into a recirculation region some distance beyond the terrace field (structure). This ‘energy shadowing’ suggests terraces may shelter basin-bounding shoreline from wind-wave attack if within (<500 m) from ‘shadow’ zone. Chan et al. (2012) also relates differences in energy shadowing to differing gap-to-structure ratios, concluding that high ratios (large areas of gaps between individual terraces) produce less effective and elongated shadow zones due to bleed flow through the field. The proportion of terrace to “gap” space along the cross-sectional area of the field relative to the predominant direction of forcing, varies by geometry as setup in the hypothetical basin grid, as does the distance of the energy shadow zone from the bounding shoreline (Table 11). The highest gap-to-structure ratio modeled “open” terrace field, the linear (0.278), displays the most elongated shadow zone (extending 900 m out from the rear of the terrace field), and the lowest, the chevron design (0.220), produced the shortest shadow zone (750 m). These results are consistent with previous studies regarding permeable structures (Chan et al. 2012). Linear terraces likely allow the most bleed flow through the field, but their elongated shadow zone suggests they may reduce energies dissipated along shorelines located at a greater distance from the terrace field. Grid and chevron terraces both produce the energy shadow zones, but they would need to be placed closer to basin-bounding shorelines in

order for them to be effective at shadowing hydrodynamic energy. As most terrace projects constructed to date in Louisiana have been placed well within the modeled shadow zones (typically < 100 m from the bounding marsh shoreline), there will be significant energy reduction along the bounding shoreline, with closer placement favoring both greater energy reduction and energy reduction over a greater length of bounding shoreline (due to the cone shape of the shadow zone). Given that the modeled gap-to-structure ratios are characteristic of real project builds in coastal Louisiana, it can also be concluded that chevron terraces re the most effective at reducing wave-current energy impacting the downwind and down current basin shoreline.

Table 11. *Gap-to-structure ratios and energy dissipation efficacy of terrace field by geometry. Terrace to void space ratio for each terrace geometry with percentage of terrace/void along cross-sectional area compared to the approximate distance of the end of energy shadow zone from terrace field at a central time step (time of maximum water velocity and total bed shear stress).*

Geometry	Ratio (m)	% Terrace	% Void	End of shadow zone (m)
Linear	520:200	72.2	27.8	900
Grid	400:150	72.7	27.3	820
Chevron	1850:520	78.0	22.0	750

None of the remote sensing study sites examined in the present study featured terraces at a great enough distance from the shoreline to contrast energy shadowing effects on shoreline marsh loss rates. In prototype terrace fields, bounding shoreline erosion will also be shaped by a variety of factors not accounted for in the modeled fields, including (1) variable compass orientation of individual high-energy hydrodynamic events, (2) variable bed strength/sediment type in the basin impacting frictional reduction of energy, (3) the importance of tropical storms, and (4) variable marsh strength/sediment type to erosion. However, all three geometries suggest

decreased regions of total bed shear stress between individual terraces as compared to the control (Figures 40-42), indicating sediment retention is likely to occur between individual terraces if sufficient material is available. This supports the field and geospatial conclusions, which found sediment retained between terraces and increased mudflat development within fields.

5.2.2 Terrace Orientation

As demonstrated by the model simulations, terrace orientation to the dominant wind-current direction influences the hydrodynamics within the field, and presumably the sediment transport as well. In these model runs displayed in Figures 42 to 44, the dominant wind-current direction was modeled a perpendicular to the orientation of the individual terraces and the long-axis of the overall terrace field. Other simulations (presented in Appendix C) tested dominant wind directions parallel (0°) and oblique (45°) to terrace (individual and field). Both the parallel and oblique simulations produced areas of higher water velocities and total bed shear stress as compared to the perpendicular simulation. These results are consistent with another study (French, 2020) which found that the perpendicular orientation of terraces is most optimal to reduce hydrodynamic energy associated with the dominant cold-front passage winds (NW and SE) in southern Louisiana.

6. Conclusions

The results of the present, combined field, remote sensing, and numerical study of marsh terracing projects across coastal Louisiana lead to the following conclusions about their effectiveness as a strategy for increasing sediment retention (i.e., reducing RSLR

elevation loss) and reducing marsh land loss in the water bodies in which they are constructed:

1. Deposition rates, as measured by feldspar plots and ^{7}Be geochronology, indicate that post-construction sediment trapping in and around the submerged areas of the terrace field can reach several cm/y—well above RSLR calculated for the sites. Deposition rates within the submerged areas of the marsh terrace field are greatest in areas of lowest elevation, which typically corresponds to the excavation pits produced during construction. This suggests that continued infilling will reduce bathymetric differences but is not definitive as to whether continued deposition will lead to mudflat evolution and an eventual emergence and marsh colonization as the few years since construction are too short to determine a long-term trajectory for the sites. Accretion on marsh terraces decreases with increasing elevation with the lowest accretion rates at the crown (apex) of the terrace ridge. These rates and patterns of trapping suggest that the terraced marshes, when fully vegetated, will begin to accumulate organo-mineralic sediments approaching those of natural marshes that will make them more resistant to RSLR.
2. In addition to field results showing marsh retention in and around constructed terrace fields, remote sensing results show evidence of elevation gain in submerged areas in the form of a conversion post-construction of more water to unvegetated wetland area (and vegetated wetland area) in the majority of sites (6 of 10) studied. These results are in agreement with numerical model results that show that, within the margins of the terrace field, water velocities and total bed shear stresses created by the wind-current regime are reduced relative to the surrounding basin. A comparison of

- hydrologic connectivity (water exchange) with the sites relative to their sediment retention suggests that trapping is favored when connectivity is low to intermediate; high connectivity appears linked to increased sediment washout from the system.
3. Remote sensing results support a reduction in the rates of bounding shoreline marsh retreat or reverses to a net land gain condition in the majority of sites (6 of 10) following terrace construction. Marsh terraces interrupt fetch to reduce wave-current energies in basins where previously uninterrupted fetch was sufficiently large to generate erosive waves (≥ 4 km) if hydrologic regimes are not significantly altered during terrace construction. Numerical modeling results show that this interruption or “shadowing” of hydrodynamic energy impacting the bounding shoreline is sensitive to wind direction, distance of the terraces from the shoreline, gap-to-terrace ratio, basin water depth, and terrace type.
 4. The success of terraces – both terrace resilience and bounding shoreline protection – are sensitive to the passage of tropical storm events: all four of the 10 sites studied that showed no wetland loss benefit were struck by a hurricane in the first hurricane season after terrace construction. The period of greatest danger to the terraces and, by extension, the surrounding basin appears to be in situations where tropical storm force winds are experienced in the first six months after terrace construction (e.g., prior to terrace settling/consolidation and marsh root colonization of the substrate).
 5. Based on the results of the numerical modeling experiment, marsh terraces should be constructed perpendicular to the orientation strongest winds if possible, which are typically (e.g., non-tropical storm) the SE (pre-frontal) and NNW (post-frontal) winds associated with cold front passages through the winter and early spring in southern

Louisiana. This provides the greatest energy buffer to reduce erosion of the adjacent basin edge shoreline marshes. Construction of terraces within about 500 m of the bounding shoreline will show the largest reduction in hydrodynamic energy and over the largest extent of the shoreline. Further, these structures retain more sediment inside the field when built in multiple rows and with a low gap-to-structure ratio (elements close together). Finally, marsh terrace projects should be completed during the winter months (November – February) to allow sufficient time for terrace ridges to consolidate prior to the passage of major tropical storm events, as hurricane strikes seem to detrimentally impact the long-term success of juvenile marsh terracing projects.

References Cited

- Allison, M. A., Chen, Q. J., Couvillion, B., Leadon, M., McCorquodale, A., Meselhe, E. & White, E. D. (2017). Coastal master plan: model improvement plan, attachment C3–2: Marsh Edge Erosion. *Coastal Protection and Restoration Authority of Louisiana*.
- Allison, M. A., Sheremet, A., Goñi, M. A., & Stone, G. W. (2005). Storm layer deposition on the Mississippi–Atchafalaya subaqueous delta generated by Hurricane Lili in 2002. *Continental Shelf Research*, 25(18), 2213-2232.
- Andersen, T. J., Svinth, S., & Pejrup, M. (2011). Temporal variation of accumulation rates on a natural salt marsh in the 20th century—The impact of sea level rise and increased inundation frequency. *Marine Geology*, 279(1-4), 178-187.
- Baumann, R. H., Day, J. W., & Miller, C. A. (1984). Mississippi deltaic wetland survival: sedimentation versus coastal submergence. *Science*, 224(4653), 1093-1095.
- Bildstein, K. L., Bancroft, G. T., Dugan, P. J., Gordon, D. H., Erwin, R. M., Nol, E. & Senner, S. E. (1991). Approaches to the conservation of coastal wetlands in the Western Hemisphere. *The Wilson Bulletin*, 218-254.
- Blum, M. D., & Roberts, H. H. (2009). Drowning of the Mississippi Delta due to insufficient sediment supply and global sea-level rise. *Nature Geoscience*, 2(7), 488-491.

Brasher, M. G. (2015). Review of the benefits of marsh terraces in the Northern Gulf of Mexico. *Ducks Unlimited, Inc., Gulf Coast Joint Venture: Lafayette, LA, USA*.

Boesch, D. F., Josselyn, M. N., Mehta, A. J., Morris, J. T., Nuttle, W. K., Simenstad, C. A., & Swift, D. J. (1994). Scientific assessment of coastal wetland loss, restoration and management in Louisiana. *Journal of Coastal Research*, i-103.

Bush Thom, C. S, La Peyre, M. K., & Nyman, J. A. (2004). Evaluation of nekton use and habitat characteristics of restored Louisiana marsh. *Ecological Engineering*, 23(2), 63-75.

Butzeck, C., Eschenbach, A., Gröngröft, A., Hansen, K., Nolte, S., & Jensen, K. (2015). Sediment deposition and accretion rates in tidal marshes are highly variable along estuarine salinity and flooding gradients. *Estuaries and Coasts*, 38(2), 434-450.

Cahoon, D. R., Reed, D. J., Day Jr, J. W., Steyer, G. D., Boumans, R. M., Lynch, J. C., ... & Latif, N. (1995). The influence of Hurricane Andrew on sediment distribution in Louisiana coastal marshes. *Journal of Coastal Research*, 280-294.

Cahoon, D. R., & Turner, R. E. (1989). Accretion and canal impacts in a rapidly subsiding wetland II. Feldspar marker horizon technique. *Estuaries*, 12(4), 260-268.

Cannaday, C. D. (2006). Effects of terraces on submerged aquatic vegetation in shallow marsh ponds in coastal southwest Louisiana.

Carlin, J. A., Lee, G. H., Dellapenna, T. M., & Laverty, P. (2016). Sediment resuspension by wind, waves, and currents during meteorological frontal passages in a micro-tidal lagoon. *Estuarine, Coastal and Shelf Science*, 172, 24-33.

Castellanos, D., & Aucoin, S. (2004). Operations, Maintenance, and Monitoring Report for Little Vermilion Bay Sediment Trapping (TV-12). *Louisiana Department of Natural Resources, Coastal Restoration Division, Lafayette, Louisiana*.

Chan, H. C., Leu, J. M., & Lai, C. J. (2007). Velocity and turbulence field around permeable structure: Comparisons between laboratory and numerical experiments. *Journal of Hydraulic Research*, 45(2), 216-226.

Cherfas, J. (1990). The fringe of the ocean-under siege from land. *Science*, 248(4952), 163-166.

Chmura, G. L., Anisfeld, S. C., Cahoon, D. R., & Lynch, J. C. (2003). Global carbon sequestration in tidal, saline wetland soils. *Global biogeochemical cycles*, 17(4).

Christiansen, T., Wiberg, P. L., & Milligan, T. G. (2000). Flow and sediment transport on a tidal salt marsh surface. *Estuarine, Coastal and Shelf Science*, 50(3), 315-331.

Coastal Protection and Restoration Authority (CPRA). (2017). *Louisiana's Comprehensive Master Plan for a Sustainable Coast*. State of Louisiana.

Couvillion BR, Barras JA, Steyer GD, Sleavin W, Fischer M, Beck H, Heckman D (2011) Land area change in coastal Louisiana from 1932 to 2010 (scientific investigations map no. 3164) (p. 12). U.S. Geological Survey.

Couvillion, B. R., Beck, H., Schoolmaster, D., & Fischer, M. (2017). *Land area change in coastal Louisiana (1932 to 2016)* (No. 3381). US Geological Survey.

Craig, N. J., Turner, R. E., & Day Jr, J. W. (1980). Wetland losses and their consequences in coastal Louisiana: *Zeitschrift zur Geomorphologie Neue Folge*, v. 34.

Day JW Jr, Britsch LD, Hawes SR, Shaffer GP, Reed DJ, Cahoon D. (2000). Pattern and process of land loss in the Mississippi Delta: a spatial and temporal analysis of wetland habitat change. *Estuaries* 23(4):425–438.

Deevey, E. S. 1955. The obliteration of the hypolimnion. *Mem. 1st. Ital. Idrobiol.* 8(suppl.): 9-38.

Elsley-Quirk, T., Graham, S. A., Mendelsohn, I. A., Snedden, G., Day, J. W., Twilley, R. R., ... & Lane, R. R. (2019). Mississippi river sediment diversions and coastal wetland

sustainability: Synthesis of responses to freshwater, sediment, and nutrient inputs. *Estuarine, Coastal and Shelf Science*, 221, 170-183.

Emanuel, K. A. (1987). The dependence of hurricane intensity on climate. *Nature*, 326(6112), 483-485.

Fagherazzi, S. (2013). The ephemeral life of a salt marsh. *Geology*, 41(8), 943-944.

French, J. E. (2020). *Optimization of Marsh Terracing as a Wetland Restoration Technique: Mitigation of Cohesive Sediment Erosion by Waves Associated with Frontal Passage* (Doctoral dissertation, Mississippi State University).

Friedrichs, C. T., & Perry, J. E. (2001). Tidal salt marsh morphodynamics: a synthesis. *Journal of Coastal Research*, 7-37.

Gagliano, S. M., Meyer-Arendt, K. J., & Wicker, K. M. (1981). Land loss in the Mississippi River deltaic plain.

Gleason, M. L., Elmer, D. A., Pien, N. C., & Fisher, J. S. (1979). Effects of stem density upon sediment retention by salt marsh cord grass, *Spartina alterniflora* Loisel. *Estuaries*, 2(4), 271-273.

Gonzalez, J. L., & Törnqvist, T. E. (2009). A new Late Holocene sea-level record from the Mississippi Delta: evidence for a climate/sea level connection?. *Quaternary Science Reviews*, 28(17-18), 1737-1749.

Gould, H. R., & McFarlan Jr, E. (1959). Geologic history of the Chenier Plain, southwestern Louisiana.

Hauser, S., Meixler, M. S., & Laba, M. (2015). Quantification of impacts and ecosystem services loss in New Jersey coastal wetlands due to Hurricane Sandy storm surge. *Wetlands*, 35(6), 1137-1148.

Hijma, M. P., Shen, Z., Törnqvist, T. E., & Mauz, B. (2017). Late Holocene evolution of a coupled, mud-dominated delta plain–chenier plain system, coastal Louisiana, USA. *Earth Surface Dynamics*, 5(4), 689.

Hilton, J. (1985). A conceptual framework for predicting the occurrence of sediment focusing and sediment redistribution in small lakes. *Limnology and Oceanography*, 30(6), 1131-1143.

Hopkinson, C. S., Gosselink, J. G., & Parrando, R. T. (1978). Aboveground Production of Seven Marsh Plant Species in Coastal Louisiana. *Ecology*, 59(4), 760-769.

Hydraulics, D. (2006). Delft3D-FLOW, a Simulation Program for Hydrodynamic Flows and Transports in 2 and 3 Dimensions. *User Manual. Version, 3*.

Hymel, M. K., & Breaux, K. A. (2012). Operations, maintenance, and monitoring report for Delta Management at Fort St. Philip. *Coastal Protection and Restoration Authority of Louisiana, New Orleans, Louisiana, USA*.

Jankowski KL, Törnqvist TE, Fernandes AM (2017) Vulnerability of Louisiana's coastal wetlands to present-day rates of relative sealevel rise. *Nature Communications* 8:14792.

Keogh, M. E., & Törnqvist, T. E. (2019). Measuring rates of present-day relative sea-level rise in low-elevation coastal zones: a critical evaluation. *Ocean Science, 15*(1).

Kesel, R. H. (1989). The role of the Mississippi River in wetland loss in southeastern Louisiana, USA. *Environmental Geology and Water Sciences, 13*(3), 183-193.

Kirwan, M. L., & Megonigal, J. P. (2013). Tidal wetland stability in the face of human impacts and sea-level rise. *Nature, 504*(7478), 53-60.

Knutson, T. R., McBride, J. L., Chan, J., Emanuel, K., Holland, G., Landsea, C. & Sugi, M. (2010). Tropical cyclones and climate change. *Nature geoscience, 3*(3), 157-163.

Kolker, A. S., Miner, M. D., & Weathers, H. D. (2012). Depositional dynamics in a river diversion receiving basin: The case of the West Bay Mississippi River

Diversion. *Estuarine, Coastal and Shelf Science*, 106, 1-12.

Kolker AS, Allison MA, Hameed S (2011). An evaluation of subsidence rates and sea-level variability in the northern Gulf of Mexico. *Geophysical Research Letters*, 38, n/a–n/a.

Kvålseth, T. O. (1989). Note on Cohen's kappa. *Psychological reports*, 65(1), 223-226.

Lane, R. R., Day, J. W., & Day, J. N. (2006). Wetland surface elevation, vertical accretion, and subsidence at three Louisiana estuaries receiving diverted Mississippi River water. *Wetlands*, 26(4), 1130-1142.

La Peyre, M. K., Gossman, B., & Nyman, J. A. (2007). Assessing functional equivalency of nekton habitat in enhanced habitats: comparison of terraced and unterraced marsh ponds. *Estuaries and Coasts*, 30(3), 526-536.

Lehman, J. T. (1975). Reconstructing the rate of accumulation of lake sediment: the effect of sediment focusing. *Quaternary Research*, 5(4), 541-550.

Likens, G. E., & Davis, M. B. (1975). Post-glacial history of Mirror Lake and its watershed in New Hampshire, USA: an initial report: With 5 figures and 2 tables in the

text. *Internationale Vereinigung für theoretische und angewandte Limnologie: Verhandlungen*, 19(2), 982-993.

Lin, Q., & Yu, S. (2018). Losses of natural coastal wetlands by land conversion and ecological degradation in the urbanizing Chinese coast. *Scientific reports*, 8(1), 1-10.

Liu, Y., Li, J., Fasullo, J., & Galloway, D. L. (2020). Land subsidence contributions to relative sea level rise at tide gauge Galveston Pier 21, Texas. *Scientific reports*, 10(1), 1-11.

McGinnis, T., and M. Guidry. (2011). Operations, maintenance, and monitoring report for Grand White Lake Land Bridge Protection (ME-19). Louisiana Office of Coastal Protection and Restoration, Operations Division, Lafayette Field Office, Lafayette, Louisiana, USA.

McGinnis, T., T. Pontiff, and J. White. (2012). Operations, maintenance and monitoring report for East Sabine Lake Hydrologic Restoration (CS-32). Coastal Protection and Restoration Authority of Louisiana, Lafayette, Louisiana, USA.

McHugh, M. L. (2012). Interrater reliability: the kappa statistic. *Biochemia medica: Biochemia medica*, 22(3), 276-282.

Michener, W. K., Blood, E. R., Bildstein, K. L., Brinson, M. M., & Gardner, L. R. (1997). Climate change, hurricanes and tropical storms, and rising sea level in coastal wetlands. *Ecological Applications*, 7(3), 770-801.

Meckel, T. A., ten Brink, U. S., & Williams, S. J. (2006). Current subsidence rates due to compaction of Holocene sediments in southern Louisiana. *Geophysical Research Letters*, 33(11).

Miller, M., & Aucoin, S. (2011). Operations, maintenance, and monitoring report for the Four-Mile Canal Terracing and Sediment Trapping (TV-18). *Coastal Protection and Restoration Authority of Louisiana, Lafayette, Louisiana, USA*.

Mitsch, W. J., & Gosselink, J. G. C. (1993). Mangrove wetlands. *Wetlands*, 2, 293-328.

Mitsch, W. J., & Gosselink, J. G. (2000). The value of wetlands: Landscapes and institutional perspectives. *Ecological Economics*, 35(200), 25-33.

Mohammed, J. (2013). Land use and cover change assessment using Remote Sensing and GIS: Dohuk City, Kurdistan, Iraq (1998–2011). *International Journal of Geomatics and Geosciences*, 3(3), 552-569.

Morton RA, Bernier JC, Barras JA (2006) Evidence of regional subsidence and associated interior wetland loss induced by hydrocarbon production, Gulf Coast region, USA. *Environmental Geology* 50(2): 261–274.

Morton, R. A., Bernier, J. C., & Kelso, K. W. (2009). *Recent subsidence and erosion at diverse wetland sites in the southeastern Mississippi Delta plain*. U. S. Geological Survey.

National Ocean and Atmospheric Administration (NOAA). (2020). *What percentage of the American population lives along the coast?* National Ocean Service website.

Nienhuis, J. H., Törnqvist, T. E., Jankowski, K. L., Fernandes, A. M., & Keogh, M. E. (2017). A new subsidence map for coastal Louisiana. *GSA Today*, 27(9), 58-59.

Nienhuis, J. H., Törnqvist, T. E., & Erkens, G. (2020). Altered surface hydrology as a potential mechanism for subsidence in coastal Louisiana. *Proceedings of the International Association of Hydrological Sciences*, 382, 333-337.

Nyman, J. A., Carloss, M., DeLaune, R. D., & Patrick Jr, W. H. (1994). Erosion rather than plant dieback as the mechanism of marsh loss in an estuarine marsh. *Earth Surface Processes and Landforms*, 19(1), 69-84.

Nyman, J. A., & Chabreck, R. H. (2012). Managing coastal wetlands for wildlife. *Wildl. Tech. Man. Manag*, 2, 133-156.

Nyman, J. A., DeLaune, R. D., & Patrick Jr, W. H. (1990). Wetland soil formation in the rapidly subsiding Mississippi River deltaic plain: Mineral and organic matter relationships. *Estuarine, Coastal and Shelf Science*, 31(1), 57-69.

Nyman, J. A., DeLaune, R. D., Roberts, H. H., & Patrick Jr, W. H. (1993). Relationship between vegetation and soil formation in a rapidly submerging coastal marsh. *Marine Ecology Progress Series*, 269-279.

Nyman, J. A., Walters, R. J., Delaune, R. D., & Patrick Jr, W. H. (2006). Marsh vertical accretion via vegetative growth. *Estuarine, Coastal and Shelf Science*, 69(3-4), 370-380.

O'Connell, J. L., & Nyman, J. A. (2010). Marsh terraces in coastal Louisiana increase marsh edge and densities of waterbirds. *Wetlands*, 30(1), 125-135.

O'Connell, J. L., & Nyman, J. A. (2011). Effects of marsh pond terracing on coastal wintering waterbirds before and after Hurricane Rita. *Environmental management*, 48(5), 975.

Odum, E. P. (1979). The value of wetlands: a hierarchical approach. *Wetland Functions and Values: The State of Our Understanding*, PE Greeson, JR Clark, and JE Clark, eds., American Water Resources Association, Bethesda, Maryland, 1-25.

Olliver, E. A., Edmonds, D. A., & Shaw, J. B. (2020). Influence of floods, tides, and vegetation on sediment retention in Wax Lake Delta, Louisiana, USA. *Journal of Geophysical Research: Earth Surface*, 125(1), e2019JF005316.

Osorio, R. J., & Linhoss, A. (2020). Evaluation of Marsh Terraces for Wetland Restoration: A Remote Sensing Approach. *Water*, 12(2), 336.

Ortiz, A. C., & Edmonds, D. A. (2016). Impact of Wind Driven Pond Expansion on Landloss in the Mississippi River Delta Plain. *AGUFM, 2016*, GC23D-1277.

Ortiz, A. C., Roy, S., & Edmonds, D. A. (2017). Land loss by pond expansion on the Mississippi River Delta Plain. *Geophysical Research Letters*, 44(8), 3635-3642.

Proffitt, C. E., Travis, S. E., & Edwards, K. R. (2003). Genotype and elevation influence *Spartina alterniflora* colonization and growth in a created salt marsh. *Ecological Applications*, 13(1), 180-192.

Ranwell, D. S. (1964). *Spartina* salt marshes in southern England: II. Rate and seasonal pattern of sediment accretion. *The Journal of Ecology*, 79-94.

Ratnaparkhi, N. S., Nagne, A. D., & Gawali, B. (2014). A Land Use Land Cover classification System Using Remote Sensing data. *International Journal of Scientific & Engineering Research*, 5(7), 2229-5518.

Reed, D. J. (1989). Patterns of sediment deposition in subsiding coastal salt marshes, Terrebonne Bay, Louisiana: the role of winter storms. *Estuaries*, 12(4), 222-227.

Reed, D. J. (1990). The impact of sea-level rise on coastal salt marshes. *Progress in Physical Geography*, 14(4), 465-481.

Reed, D. J. (2002). Sea-level rise and coastal marsh sustainability: geological and ecological factors in the Mississippi delta plain. *Geomorphology*, 48(1-3), 233-243.

Rogers, K., Kelleway, J. J., Saintilan, N., Megonigal, J. P., Adams, J. B., Holmquist, J. R. & Woodroffe, C. D. (2019). Wetland carbon storage controlled by millennial-scale variation in relative sea-level rise. *Nature*, 567(7746), 91-95.

Rozas, L. P., Caldwell, P., & Minello, T. J. (2005). The fishery value of salt marsh restoration projects. *Journal of Coastal Research*, 37-50.

Rozas, L. P., & Minello, T. J. (2001). Marsh terracing as a wetland restoration tool for creating fishery habitat. *Wetlands*, 21(3), 327-341.

Rozas, L. P., & Minello, T. J. (2007). Restoring coastal habitat using marsh terracing: the effect of cell size on nekton use. *Wetlands*, 27(3), 595-609.

Rozas, L. P., & Minello, T. J. (2009). Using nekton growth as a metric for assessing habitat restoration by marsh terracing. *Marine Ecology Progress Series*, 394, 179-193.

Rwanga, S. S., & Ndambuki, J. M. (2017). Accuracy assessment of land use/land cover classification using remote sensing and GIS. *International Journal of Geosciences*, 8(04), 611.

Sapkota, Y., & White, J. R. (2019). Marsh edge erosion and associated carbon dynamics in coastal Louisiana: a proxy for future wetland-dominated coastlines world-wide. *Estuarine, Coastal and Shelf Science*, 226, 106289.

Sendrowski, A., Sadid, K., Meselhe, E., Wagner, W., Mohrig, D., & Passalacqua, P. (2018). Transfer entropy as a tool for hydrodynamic model validation. *Entropy*. 20(1), 58.

Snedden, G. A., Cable, J. E., Swarzenski, C., & Swenson, E. (2007). Sediment discharge into a subsiding Louisiana deltaic estuary through a Mississippi River diversion. *Estuarine, Coastal and Shelf Science*, 71(1-2), 181-193.

Sommerfield, C. K., Nittrouer, C. A., & Alexander, C. R. (1999). ^{7}Be as a tracer of flood sedimentation on the northern California continental margin. *Continental Shelf Research*, 19(3), 335-361.

Southworth, M. (1989). Theory and practice of contemporary urban design: a review of urban design plans in the United States. *The Town Planning Review*, 369-402.

Stevenson, J. C., Ward, L. G., & Kearney, M. S. (1986). Vertical accretion in marshes with varying rates of sea level rise. In *Estuarine variability* (pp. 241-259). Academic Press.

Steyer GD (1993). Final report, Sabine terracing project. Louisiana Department of Natural Resources, Coastal Restoration Division, Baton Rouge.

Taylor, A., Blake, W. H., Couldrick, L., & Keith-Roach, M. J. (2012). Sorption behaviour of beryllium-7 and implications for its use as a sediment tracer. *Geoderma*, 187, 16-23.

Taylor, A., Blake, W. H., Smith, H. G., Mabit, L., & Keith-Roach, M. J. (2013). Assumptions and challenges in the use of fallout beryllium-7 as a soil and sediment tracer in river basins. *Earth-science reviews*, 126, 85-95.

Thibodeaux, C., & Guidry, M. (2009). Operations. *Maintenance, and Monitoring Report for Pecan Island Terracing (ME-14)*.

Tiner, R. W. (1984). *Wetlands of the United States: current status and recent trends*. National Wetlands Inventory, Fish and Wildlife Service, US Department of the Interior.

Ting, M., Kossin, J. P., Camargo, S. J., & Li, C. (2019). Past and future hurricane intensity change along the US east coast. *Scientific reports*, 9(1), 1-8.

Törnqvist, T. E., Jankowski, K. L., Li, Y. X., & González, J. L. (2020). Tipping points of Mississippi Delta marshes due to accelerated sea-level rise. *Science Advances*, 6(21), eaaz5512.

Turner, R. E., & Streever, B. (2002). *Approaches to coastal wetland restoration: Northern Gulf of Mexico*. Kugler Publications.

Turner, R. E., Baustian, J. J., Swenson, E. M., & Spicer, J. S. (2006). Wetland sedimentation from hurricanes Katrina and Rita. *Science*, 314(5798), 449-452.

Tweel, A. W., & Turner, R. E. (2014). Contribution of tropical cyclones to the sediment budget for coastal wetlands in Louisiana, USA. *Landscape ecology*, 29(6), 1083-1094.

Watson CS, White NJ, Church JA, King MA, Burgette RJ, Legresy B (2015) Unabated global mean sea-level rise over the satellite altimeter era. *Nature Climate Change* 5(6):565–568.

Westphal K.A. and Nakashima L.D. (2019). The Efficacy of Terraces used as Sediment Retention Devices: National Audubon Society, Baton Rouge, LA. In press.

White, F. M., & Corfield, I. (2006). *Viscous fluid flow* (Vol. 3, pp. 433-434). New York: McGraw-Hill.

White, E. D., Reed, D. J., & Meselhe, E. A. (2019). Modeled Sediment Availability, Deposition, and Decadal Land Change in Coastal Louisiana Marshes under Future Relative Sea Level Rise Scenarios. *Wetlands*, 39(6), 1233-1248.

Whittaker, R. H., & Likens, G. E. (1973). Primary production: the biosphere and man. *Human Ecology*, 1(4), 357-369.

Wilson, C. A., & Allison, M. A. (2008). An equilibrium profile model for retreating marsh shorelines in southeast Louisiana. *Estuarine, Coastal and Shelf Science*, 80(4), 483-494.

Wilson, I. T., & Opdyke, D. F. (1941). The distribution of the chemical constituents in the accumulated sediment of Tippecanoe Lake. *Investigations of Indiana Lakes and Streams*, 2, 16-42.

Wolstencroft, M., Shen, Z., Törnqvist, T. E., Milne, G. A., & Kulp, M. (2014). Understanding subsidence in the Mississippi Delta region due to sediment, ice, and ocean loading: Insights from geophysical modeling. *Journal of Geophysical Research: Solid Earth*, 119(4), 3838-3856.

Xiao, D., Zhang, L., & Zhu, Z. (2010). The range expansion patterns of *Spartina alterniflora* on salt marshes in the Yangtze Estuary, China. *Estuarine, Coastal and Shelf Science*, 88(1), 99-104.

Yuill, B., Lavoie, D., & Reed, D. J. (2009). Understanding subsidence processes in coastal Louisiana. *Journal of Coastal Research*, (54), 23-36.

Appendices

Appendix A: Feldspar Deposition Rates and Layer Characteristics in Terraces

Table A1. Deposition statistics (rate in mm/d) derived from feldspar marker horizon plots at Bayou Monnaie and Yankee Canal.

Bayou Monnaie								
<i>Terrace</i>	<i>Plot</i>	<i>Rate</i>	<i>Terrace</i>	<i>Plot</i>	<i>Rate</i>	<i>Terrace</i>	<i>Plot</i>	<i>Rate</i>
T1	1	w/o	T2	1	w/o	T3	1	w/o
T1	2	0.127	T2	2	0.169	T3	2	0.127
T1	3	0.056	T2	3	0.021	T3	3	0.070
T1	4	0.042	T2	4	0.014	T3	4	w/o
T1	5	0.014	T2	5	0.004	T3	5	0.042
T1	6	0.028	T2	6	0	T3	6	w/o
T1	7	0.162	T2	7	0.003	T3	7	0.056
T1	8	0.070	T2	8	0.007	T3	8	0.028
T1	9	0.070	T2	9	0	T3	9	0.028
T1	10	0.007	T2	10	0	T3	10	0.004
T1	11	0.021	T2	11	0.042	T3	11	0.007
T1	12	w/o	T2	12	0.197	T3	12	0.014
T1	13	0.014	T2	13	0.042	T3	13	w/o
T1	14	0.183	T2	14	0.014	T3	14	0.011
T1	15	0.127	T2	15	0	T3	15	0.085
			T2	16	0	T3	16	0.014
			T2	17	0.254			
Yankee Canal								
<i>Terrace</i>	<i>Plot</i>	<i>Rate</i>	<i>Terrace</i>	<i>Plot</i>	<i>Rate</i>	<i>Terrace</i>	<i>Plot</i>	<i>Rate</i>
1	1	0.007	2	1	0.028	3	1	0.028
1	2	0.028	2	2	0.021	3	2	0
1	3	0.014	2	3	0.028	3	3	0.028
<i>Terrace</i>	<i>Plot</i>	<i>Rate</i>	<i>Terrace</i>	<i>Plot</i>	<i>Rate</i>	<i>Terrace</i>	<i>Plot</i>	<i>Rate</i>
4	1	w/o	5	1	0.035	6	1	0.042
4	2	0.014	5	2	w/o	6	2	0.021
4	3	0.042	5	3	w/o	6	3	0.028

w/o = washouts where feldspar markers could not be retrieved due to water disturbance

Table A2. Bulk properties –for sediment layers recovered from feldspar deposits along terraces at Bayou Monnaie.

Terrace-Site	Porosity	OM %	D ₅₀ μm	SBD g cm ⁻³	DBD g cm ⁻³
T1-2	0.61	11.53	15.2	2.05	0.56
T1-3	0.68	24.87	39.5	1.85	0.30
T1-4	0.55	10.58	37.5	2.20	0.59
T1-5	0.61	24.06	20.2	2.05	0.31
T1-6	0.70	21.08	21.3	1.80	0.35
T1-7	0.56	16.24	25.4	2.17	0.43
T1-8	0.73	12.88	14.5	1.72	0.51
T1-9	0.62	8.11	26.7	2.01	0.71
T1-10	0.50	5.96	15.0	2.33	0.85
T1-11	0.56	7.41	11.7	2.17	0.75
T1-13	0.56	7.16	17.4	2.15	0.76
T1-14	0.62	7.19	17.3	2.03	0.76
T1-15	0.68	11.58	24.9	1.87	0.55
T2-2	0.67	9.15	18.1	1.89	0.65
T2-3	0.69	18.84	12.6	1.82	0.38
T2-4	0.64	11.19	11.7	1.96	0.57
T2-5	0.52	10.97	28.2	2.28	0.58
T2-8	0.48	6.72	39.5	2.39	0.79
T2-11	0.67	20.54	17.4	1.87	0.36
T2-12	0.62	8.40	17.8	2.02	0.69
T2-13	0.71	12.67	13.5	1.79	0.52
T2-14	0.56	7.74	21.9	2.17	0.73
T2-17	0.57	5.69	24.3	2.14	0.87
T3-2	0.66	9.13	32.3	1.92	0.65
T3-3	0.62	9.76	9.77	2.02	0.62
T3-5	0.67	9.36	18.7	1.89	0.64
T3-7	0.62	8.59	29.9	2.01	0.68
T3-8	0.59	7.48	20.2	2.09	0.73
T3-9	0.64	8.98	25.4	1.96	0.66
T3-11	0.63	12.11	24.8	1.99	0.54
T3-12	0.57	6.71	37.5	2.15	0.80
T3-14	0.64	14.91	10.3	1.96	0.46
T3-15	0.62	9.38	31.3	2.02	0.64
T3-16	0.70	16.67	26.4	1.80	0.42

OM% = organic matter content of the homogenized layer based on loss on ignition

D₅₀ = median particle size from grain size analysis

SBD and DBD = saturated and dry bulk density of the homogenized layer

Table A3. Bulk properties –for sediment layers recovered from feldspar deposits along terraces at Yankee Canal.

Terrace-Site	Porosity	OM %	D ₅₀ μm	SBD g cm ⁻³	DBD g cm ⁻³
1-1	0.446	28.89	23.3	2.48	0.266
1-2	0.398	11.37	21.6	2.61	0.561
1-3	0.407	23.86	32.6	2.58	0.314
2-1	0.409	21.09	11.2	2.58	0.348
2-2	0.395	17.19	19.5	2.61	0.410
2-3	0.407	19.63	28.4	2.58	0.368
3-1	0.400	28.57	22.1	2.60	0.268
3-3	0.397	9.86	18.2	2.61	0.620
4-2	0.395	42.00	--	2.61	0.191
4-3	0.406	19.57	30.2	2.59	0.369
5-2	0.399	10.47	15.2	2.60	0.594
6-1	0.409	19.07	15.1	2.58	0.377
6-2	0.400	14.52	27.5	2.60	0.468
6-3	0.420	28.49	14.3	2.55	0.269

Table A4. ⁷Be activities for cores collected at Bay Alexis on 05/13/2020.

Core	Depth (cm)	⁷ Be Activity (dpm/g)	Error (±)
1BA	0-1	4.81	0.69
	1-2	1.91	0.64
	2-3	0.71	0.64
	3-4	0	0
2BA	0-1	0	0
	1-2	0.042	0.34
3BA	0-1	1.04	1.02
	1-2	0.33	0.70
	2-3	0	0
4BA	0-1	3.81	0.59
	1-2	2.42	0.46
	2-3	1.83	0.61
	3-4	0.02	0.41
5BA	0-1	0.324	0.306
	1-2	0	0
6BA	0-1	2.226	0.679
	1-2	0.687	0.767
	2-3	0.768	0.403
7BA	0-1	0.3	0.74
	1-2	0.22	0.62

	2-3	0	0
8BA	0-1	0.47	0.66
	1-2	0.3	0.61
	2-3	0.14	0.42
9BA	0-1	1.75	0.97
	1-2	0.2	0.61
	2-3	1.07	0.76
	3-4	0	0
10BA	0-1	1.555	0.482
	1-2	1.061	0.406
	2-3	0.868	0.439
	3-4	0.173	0.249
	4-5	0.00391	0.22
11BA	0-1	1.76	0.62
	1-2	0	0

Table A5. Porosity (Φ) and organic content (LOI) from cores intervals collected at Bayou Monnaie in April 2020.

Core	Depth (cm)	Φ	LOI (%)
BM-A	0-1	0.77	13.91
	1-2	0.75	11.81
	2-3	0.72	10.00
	3-4	0.75	13.04
	4-5	0.82	21.10
	5-6	0.82	20.70
	6-7	0.80	18.29
	7-8	0.74	9.77
	8-9	0.74	9.43
	9-10	0.73	8.72
	11-12	0.73	7.74
	13-14	0.73	7.94
	15-16	0.73	8.09
	17-18	0.73	8.68
	19-20	0.73	8.50
	21-22	0.73	9.02
	23-24	0.72	8.06
	25-26	0.72	8.18
	27-28	0.72	7.91
BM-B	0-1	0.82	19.94
	1-2	0.88	28.22
	2-3	0.92	52.86
	3-4	0.93	58.77

	4-5	0.91	43.04
	5-6	0.95	74.98
	6-7	0.95	76.45
	7-8	0.95	78.58
	8-9	0.95	78.30
	9-10	0.95	77.44
	11-12	0.95	76.93
	13-14	0.95	78.00
	15-16	0.94	76.05
	17-18	0.94	73.42
	19-20	0.94	71.40
	21-22	0.93	63.93
	23-24	0.91	60.15
	25-26	0.92	62.06
	27-28	0.93	69.78
	29-30	0.94	61.63
	31-32	0.93	57.27
	33-34	0.90	43.87
BM-C	0-1	0.91	22.72
	1-2	0.89	22.68
	2-3	0.90	22.25
	3-4	0.87	19.12
	4-5	0.87	18.64
	5-6	0.87	17.96
	6-7	0.86	17.92
	7-8	0.87	20.26
	8-9	0.86	19.33
	9-10	0.86	19.77
	11-12	0.86	22.08
	13-14	0.86	21.65
	15-16	0.85	21.29
	17-18	0.84	19.26
	19-20	0.83	19.30
	21-22	0.83	19.14
	23-24	0.83	20.74
BM-D	0-1	0.77	13.37
	1-2	0.77	13.21
	2-3	0.77	12.72
	3-4	0.75	10.48
	4-5	0.74	11.13
	5-6	0.74	10.31
	6-7	0.74	9.85
	7-8	0.73	9.18
	8-9	0.73	9.55
	9-10	0.75	11.72

	11-12	0.72	11.30
	13-14	0.74	12.87
	15-16	0.73	14.35
	17-18	0.73	12.07
	19-20	0.71	9.86
	21-22	0.68	9.05
	23-24	0.67	7.81
BM-E	0-1	0.76	13.45
	1-2	0.76	13.31
	2-3	0.76	12.85
	3-4	0.77	56.00
	4-5	0.78	16.59
	5-6	0.85	21.28
	6-7	0.83	31.15
	7-8	0.85	34.24
	8-9	0.85	28.25
	9-10	0.88	34.44
	11-12	0.93	68.07
	13-14	0.92	56.99
	15-16	0.94	78.29
	17-18	0.94	79.09
	19-20	0.94	83.97
BM-F	0-1	0.79	14.49
	1-2	0.82	16.31
	2-3	0.84	16.85
	3-4	0.84	17.23
	4-5	0.84	18.17
	5-6	0.83	16.28
	6-7	0.82	16.28
	7-8	0.82	16.13
	8-9	0.81	15.69
	9-10	0.80	15.65
	11-12	0.80	15.81
	13-14	0.80	15.16
	15-16	0.79	14.19
	17-18	0.78	26.30
	19-20	0.78	12.20
	21-22	0.77	12.12

Table A6. Porosity and organic content (LOI) values from long (auger) cores collected at Bayou Monnaie in June 2018.

Core	Depth (cm)	Φ	LOI (%)
BM12	0-2	0.93	62.32
	15-17	0.92	55.91

	25-27	0.82	22.06
	34-36	0.71	6.66
	52-54	0.86	33.33
	74-76	0.90	49.09
	96-98	0.91	50.11
	112-114	0.70	7.19
	116-118	0.87	29.04
	142-144	0.68	6.86
BM13	1-3	0.87	20.34
	14-16	0.94	73.32
	30-32	0.94	69.97
	38-40	0.89	45.18
	45-47	0.79	15.95
	78-80	0.90	50.10
BM14	4-6	0.83	25.33
	20-22	0.90	40.33
	44-46	0.72	12.16
	70-72	0.65	8.88
	80-82	0.60	19.18
	88-90	0.52	1.79
BM15	2-4	0.86	22.57
	20-22	0.83	23.80
	30-32	0.87	30.92
	48-50	0.88	33.52
	70-72	0.85	26.12
	94-96	0.84	26.46
	114-116	0.83	24.59
	132-134	0.85	26.40
	170-172	0.82	22.04

Table A7. Porosity and organic content (LOI) values from long (push) cores collected at Yankee Canal in March 2020.

Core	Depth (cm)	Φ	LOI (%)
YC-2	0-1	0.88	13.29
	1-2	0.66	9.89
	2-3	0.88	14.77
	3-4	0.88	20.24
	4-5	0.88	20.32
	5-6	0.89	20.43
	6-7	0.89	21.59
	7-8	0.91	25.31
	8-9	0.90	23.23
	9-10	0.89	9.92
	11-12	0.74	11.12

	13-14	0.76	8.10
	15-16	0.74	8.29
	17-18	0.78	9.93
YC-3	0-1	0.73	18.36
	1-2	0.85	19.67
	2-3	0.86	21.36
	3-4	0.86	20.28
	4-5	0.91	20.80
	5-6	0.88	20.54
	6-7	0.89	20.62
	7-8	0.89	19.87
	8-9	0.89	20.25
	9-10	0.89	14.72
	11-12	0.90	28.24
	13-14	0.84	8.37
	15-16	0.89	14.56
	17-18	0.88	25.70
	19-20	0.83	12.63
	21-22	0.83	24.10
	23-24	--	11.74
	25-26	--	6.14
YC-4	0-1	0.91	21.79
	1-2	0.88	22.00
	2-3	0.88	22.37
	3-4	0.88	19.76
	4-5	0.87	20.29
	5-6	0.88	20.12
	6-7	0.89	20.74
	7-8	0.88	20.22
	8-9	0.87	21.01
	9-10	0.75	20.50
	11-12	0.67	9.71
	13-14	0.79	10.54
	15-16	0.79	6.55
	17-18	0.74	6.32
	19-20	0.76	7.92
	21-22	0.75	6.61
YC-7	0-1	0.88	23.10
	1-2	0.86	20.12
	2-3	0.86	20.33
	3-4	0.86	17.70
	4-5	0.86	21.55
	5-6	0.82	16.86
	6-7	0.81	15.35
	7-8	0.77	12.23

	8-9	0.76	14.23
	9-10	0.71	7.35
	11-12	0.71	--
	13-14	0.70	8.05
	15-16	0.72	9.50
	17-18	0.74	8.72
	19-20	0.75	9.59
	21-22	0.74	8.98
	23-24	0.76	9.71
	25-26	0.78	7.89
YC-8	0-1	0.87	24.70
	1-2	0.86	22.77
	2-3	0.86	23.18
	3-4	0.85	21.36
	4-5	0.81	17.49
	5-6	0.83	17.53
	6-7	0.82	16.26
	7-8	0.82	14.66
	8-9	0.81	12.78
	9-10	0.80	12.17
	11-12	0.80	11.69
	13-14	0.80	13.34
	15-16	0.80	13.05
	17-18	0.80	13.17
	19-20	0.79	12.63
	21-22	0.77	11.38
	23-24	0.78	12.48
	25-26	0.79	6.60
	27-28	0.80	5.78
	29-30	0.70	7.07
YC-9	0-1	0.85	23.18
	1-2	0.84	20.62
	2-3	0.82	18.53
	3-4	0.78	16.58
	4-5	0.77	14.57
	5-6	0.76	12.78
	6-7	0.76	12.32
	7-8	0.76	4.65
	8-9	0.77	8.58
	9-10	0.75	9.68
	11-12	0.75	6.68
	13-14	0.72	7.22
	15-16	0.73	6.29
YC-12	0-1	0.79	9.11
	1-2	0.75	21.12

	2-3	0.72	10.27
	3-4	0.74	6.31
	4-5	0.78	--
	5-6	0.61	5.88
	6-7	0.68	6.03
	7-8	0.74	6.18
	8-9	0.81	5.63
	9-10	0.56	5.65
	11-12	0.69	--
	13-14	0.60	--
	15-16	0.54	--
	17-18	0.76	--
YC-13	0-1	0.77	10.49
	1-2	0.72	10.96
	2-3	0.73	6.80
	3-4	0.69	6.22
	4-5	0.68	10.39
	5-6	0.67	5.13
	6-7	0.67	5.49
	7-8	0.66	4.88
	8-9	0.66	4.48
	9-10	0.67	6.53
	11-12	0.66	--
	13-14	0.66	--
	15-16	0.66	--
	17-18	0.66	--
	19-20	0.65	--
	21-22	0.64	--
	23-24	0.65	--
YC-14	0-1	0.62	4.40
	1-2	0.63	4.13
	2-3	0.62	3.87
	3-4	0.61	3.56
	4-5	0.62	4.03
	5-6	0.60	3.52
	6-7	0.62	3.50

Table A8. Porosity (Φ) values from cores collected at Bay Alexis in May 2020. Organic content (%) by LOI was not performed on these cores.

Core	Depth (cm)	Φ
1 BA	0-1	0.94
	1-2	0.86
	2-3	0.86

	3-4	0.88
	4-5	0.86
	5-6	0.91
	6-7	0.85
	7-8	0.82
	8-9	0.79
	9-10	0.77
	11-12	0.75
	13-14	0.74
	15-16	0.77
	17-18	0.76
	19-20	0.79
	21-22	0.80
	23-24	0.78
	25-26	0.77
	27-28	0.76
	29-30	0.77
	31-32	0.76
	33-34	0.74
2 BA	0-1	0.70
	1-2	0.65
	2-3	0.61
	3-4	0.59
	4-5	0.60
	5-6	0.60
	6-7	0.60
	7-8	0.59
	8-9	0.60
	9-10	0.61
	11-12	0.59
	13-14	0.56
	15-16	0.55
	17-18	0.55
	19-20	0.57
	21-22	0.59
	23-24	0.63
	25-26	0.60
	27-28	0.62
	29-30	0.62
	31-32	0.63
	33-34	0.59
3 BA	0-1	0.81
	1-2	0.72
	2-3	0.52
	3-4	0.53

	4-5	0.62
	5-6	0.70
	6-7	0.81
	7-8	0.82
	8-9	0.83
	9-10	0.82
	11-12	0.84
	13-14	0.79
	15-16	0.80
	17-18	0.82
	19-20	0.81
	21-22	0.79
	23-24	0.78
	25-26	0.76
	27-28	0.76
	29-30	0.75
	31-32	0.74
	33-34	0.73
4 BA	0-1	0.90
	1-2	0.84
	2-3	0.84
	3-4	0.86
	4-5	0.84
	5-6	0.80
5 BA	0-1	0.64
	1-2	0.62
	2-3	0.62
	3-4	0.62
	4-5	0.60
	5-6	0.59
6 BA	0-1	0.87
	1-2	0.84
	2-3	0.77
	3-4	0.69
	4-5	0.67
	5-6	0.68
7 BA	0-1	0.83
	1-2	0.78
	2-3	0.69
	3-4	0.65
	4-5	0.64
	5-6	0.62
8 BA	0-1	0.95
	1-2	0.92
	2-3	0.91

	3-4	0.89
	4-5	0.86
	5-6	0.90
9 BA	0-1	0.80
	1-2	0.75
	2-3	0.85
	3-4	0.82
	4-5	0.80
	5-6	0.79
	6-7	0.77
	7-8	0.77
	8-9	0.76
	9-10	0.73
	11-12	0.73
	13-14	0.74
	15-16	0.70
	17-18	0.71
	19-20	0.71
	21-22	0.67
	23-24	0.68
	25-26	0.70
	27-28	0.67
	29-30	0.67
10 BA	0-1	0.73
	1-2	0.72
	2-3	0.72
	3-4	0.72
	4-5	0.73
	5-6	0.71
	6-7	0.72
	7-8	0.72
	8-9	0.72
	9-10	0.71
	11-12	0.69
	13-14	0.62
11 BA	0-1	0.72
	1-2	0.62
	2-3	0.61
	3-4	0.56
	4-5	0.53
	5-6	0.58
	6-7	0.56
	7-8	0.58
	8-9	0.60
	9-10	0.62

	11-12	0.61
	13-14	0.60

Table A9. Sample locations at Bayou Monnaie.

Feldspar		
Terrace-Plot	Latitude (°)	Longitude (°)
T1-2	29.410017	90.313833
T1-3	29.410144	-90.313601
T1-4	29.410104	-90.313657
T1-5	29.410026	-90.313802
T1-6	29.410062	-90.313752
T1-7	29.410002	-90.313865
T1-8	29.409985	-90.31385
T1-9	29.409965	-90.313931
T1-10	29.409957	-90.31393
T1-11	29.409988	-90.31394
T1-13	29.40994	-90.313963
T1-14	29.409911	-90.314019
T1-15	29.409888	-90.314012
T2-2	29.409834	-90.31414
T2-3	29.406917	-90.308667
T2-4	29.406786	-90.308623
T2-5	29.406831	-90.308676
T2-7	29.406844	-90.308651
T2-8	29.406842	-90.308622
T2-11	29.406842	-90.308603
T2-12	29.406855	-90.308599
T2-13	29.406866	-90.308597
T2-14	29.40688	-90.308635
T2-17	29.406882	-90.308654
T3-2	29.4069	-90.308703
T3-3	29.406923	-90.308721
T3-4	29.406946	-90.308754
T3-5	29.406976	-90.308734
T3-7	29.406983	-90.308702
T3-8	29.40709	-90.30879
T3-9	29.40711	-90.30883
T3-10	29.40315	-90.3074
T3-11	29.403082	-90.307228
T3-12	29.403094	-90.307232
T3-14	29.403089	-90.307277
T3-15	29.403108	-90.307352
T3-16	29.403116	-90.307369
Cores		
BM A	29.409394	-90.313784
BM B	29.409570	-90.313503
BM C	29.409755	-90.313192

BM D	29.405869	-90.310284
BM E	29.405849	-90.309862
BM F	29.405852	-90.309425
BM12	29.402060	-90.307090
BM13	29.402480	-90.307340
BM14	29.401890	-90.307080
BM15	29.402430	-90.307790

Table A10. Sample locations at Yankee Canal.

Feldspar		
Terrace-Plot	Latitude (°)	Longitude (°)
1-1, 2, 3	29.408252	-90.217338
2- 1, 2, 3	29.408284	-90.217259
3-1	29.409858	-90.215260
3-3	29.409875	-90.215281
4-2	29.425542	-90.226165
4-3	29.425542	-90.226181
5-2	29.424058	-90.222937
6-1	29.423694	-90.225217
6-2	29.423685	-90.225271
6-3	29.423643	-90.225332
Cores		
YC 2	29.409187	-90.220019
YC 3	29.409030	-90.219961
YC 4	29.408700	-90.219850
YC 7	29.407690	-90.217883
YC 8	29.407555	-90.217784
YC 9	29.407276	-90.217512
YC 12	29.424325	-90.226488
YC 13	29.424076	-90.226386
YC 14	29.423703	-90.226244

Table A11. Sample locations at Bay Alexis.

Cores (⁷Be)		
Site	Latitude (°)	Longitude (°)
1 BA	29.324126	-89.335285
2 BA	29.324086	-89.335578
3 BA	29.324021	-89.335171
4 BA	29.324503	-89.332774
5 BA	29.324240	-89.328245
6 BA	29.324163	-89.330927
7 BA	29.325352	-89.328647
8 BA	29.325649	-89.329933
9 BA	29.324849	-89.329781
10 BA	29.324699	-89.330088
11 BA	29.324381	-89.329281

Appendix B: Remote Sensing Category Change Results

Refer to Table 4 (§4.3 Remote Sensing Analysis) for integer-corresponding change definitions.

Table B1. Total categorical changes in area (m²) within the study area polygon before terrace construction at remote sensing sites.

Site	-6	-5	-4	-3	-2	-1	0	1	2	3	4	5	6
1102	136064	1165	214738	9745	0	76853	2696955	68099	133071	0	0	111016	154031
2015W	64255	7858	36771	14315	299	86284	1674313	336714	28393	3019	4798	2338	23891
2015C	9434	3202	2574	888	4840	6892	481485	10367	3749	265	237	4649	1251
2015E	10175	9236	10088	5821	5237	1241	1186497	29953	21459	370	32237	9152	30878
3008	11854	311	1597	153	34075	9295	1015108	4045	8793	565	7414	2992	23234
3006	188077	46169	199437	30180	63825	25685	2475396	394835	35335	1079	22988	7662	63289
5001	151391	0	8897	0	202511	95426	15328717	0	11397	14289	107693	2440	41016
7001	37085	15314	6856	3214	46701	166093	1206170	2634	32800	57581	31952	81331	87729
7006N	9205	2385	0	0	48466	7044	1097533	11178	0	5581	21981	8427	36205
7006S	9661	622	0	0	5878	0	494541	4521	0	0	5234	0	22015

Table B2. Total categorical changes in area (m²) within the study area polygon after terrace construction at remote sensing study sites.

Site	-6	-5	-4	-3	-2	-1	0	1	2	3	4	5	6
1102	27869	13188	94441	27867	37773	68851	2554295	158176	365964	12364	198458	2020	64761
2015W	19788 5	17574	62864	16376	5173	140242	1540489	62084	59538	8866	16262	12707	143188
2015C	33203	4983	251	10	41105	400	438095	3519	309	183	3600	80	4095
2015E	82760	115344	1719	3812	54502	836	1013177	37885	3634	139	34382	24	4130
3008	11776	70256	6915	1282	44098	5269	883865	18480	2405	555	16657	1077	56801
3006	7570	22491	15726	3395	7121	46694	2707251	189888	362564	3749	22315	91414	73779
5001	44367	479004	33702	78788	160536	141	14552492	408025	64515	4	42395	5	99803
7001	21433	40332	65384	47856	71385	84151	1153110	61031	216188	3302	8015	2078	1195
7006N	700	52014	1311	16570	10172	5259	1040910	7500	10883	6870	4000	91510	306
7006S	116	2639	830	519	3176	3840	505693	2074	10152	3624	5045	2398	2366

Table B3. Categorical changes in area (m²) within the terrace field (excluding the bounding shoreline change) after terrace construction at each remote sensing study site. Changes associated with the bounding shoreline can be obtained by subtracting these results from those in Table B2.

Site	-6	-5	-4	-3	-2	-1	0	1	2	3	4	5	6
1102	11396	774	18491	1132	10521	3421	789697	4809	77435	1918	24413	630	13905
2015W	14649	653	464	79	151	1	486094	1520	1657	0	550	1	50190
2015C	6861	78	189	8	14994	0	325299	464	291	0	1353	27	3428
2015E	18713	37185	9	28	1927	2	680334	7139	322	0	52	0	1597
3008	4142	15364	4831	489	32348	0	487832	4585	1240	0	4986	0	34766
3006	2080	6821	3142	2926	885	1836	792967	20931	326450	206	4293	27770	22422
5001	16539	161184	2462	11954	69060	72	2694095	96872	9062	3	15683	1	40605
7001	2469	9064	1757	3683	6344	47	44017	5349	2629	13	224	0	2
7006N	10	28497	113	14159	3952	375	390276	12098	5471	3177	1559	52928	37
7006S	68	269	213	96	1573	842	284326	1518	5682	1499	4459	1481	2291

Table B4. Extent (UTM latitude/longitude in meters) of study polygon boundary for each remote sensing site. All sites are located within UTM Zone 15N and extents are measured within the NAD 1983 UTM Zone 15N coordinate system.

<i>Site</i>	<i>Upper left</i>	<i>Upper right</i>
	<i>Lower left</i>	<i>Lower right</i>
1102	433910.054, 3327951.155	435772.725, 3328041.113
	433920.638, 3325612.233	435788.600, 3325691.608
2015W	507625.357, 3287602.179	509335.892, 3287641.866
	507676.951, 3285689.237	509323.986, 3285685.269
2015C	509315.735, 3287394.153	510024.820, 3287387.803
	509260.702, 3286213.051	509967.670, 3286179.184
2015E	510025.167, 3287275.353	511926.202, 3287156.29
	510104.542, 3285989.476	511942.077, 3285862.475
3008	576694.745, 3284352.376	577950.517, 3284397.225
	576806.867, 3283249.090	578053.670, 3283275.999
3006	578947.439, 3281636.684	577951.644, 3282008.629
	579169.690, 3279684.055	578017.790, 3280255.761
5001	630447.604, 3291687.743	634289.362, 3291687.743
	630447.604, 3287528.484	634289.362, 3287528.484
7001	748028.412, 3269333.817	749731.670, 3269442.957
	748177.240, 3267723.162	749744.900, 3267706.626
7006N	768732.565, 3258623.061	770286.995, 3258546.993
	768838.399, 3257534.959	770270.459, 3257528.345
7006S	769349.099, 3256786.858	770708.002, 3256804.321
	769414.187, 3256204.245	770730.227, 3256116.932

Table B5. Summary (descriptive statistics) of the 10 kappa coefficients across each classified image analyzed for remote sensing.

<i>Characteristic</i>	<i>Value</i>
Mean	0.854
Median	0.859
Mode	0.889
Standard Error	0.009744
Standard Deviation	0.061629
Sample Variance	0.003798
Kurtosis	0.39707
Skewness	-0.6352
Range	0.270
Minimum	0.691
Maximum	0.961
Sum	34.176
Count	40
Confidence Level (95.0%)	0.0197

Appendix C: Numerical Modeling Supplementary Results

Twelve (12) numerical modeling simulations were ultimately used for this study. Each terrace geometry (linear, grid, chevron, and a control without terraces) was run in separate simulations with parallel (0°), oblique (45°), or perpendicular (90°) wind directions as shown in Figure C1. Within the 15 x 15 km domain were two latitudinal oriented terrace fields placed equidistance from the upstream river (discharge) boundary. Results presented herein feature the entire domain, showing both terrace fields. Unlike the resulting hydrodynamic patterns (water velocity, total bed shear stress values) of the perpendicular wind simulation (Figure 40-42) where the northern and southern terrace field vectors were virtually identical, the northern and southern fields present different hydrodynamic patterns in the parallel and oblique simulations. Figure C2 displays the water velocity outputs at the time step of maximum water velocity (01-03-2018 at 00:00:00.00) for the parallel wind simulation. Figure C3 presents the water velocity outputs at the same time step for the oblique wind simulation. Given the relationship between water velocity and total bed shear stress, outputs illustrating the latter may be extrapolated and were thereby excluded.

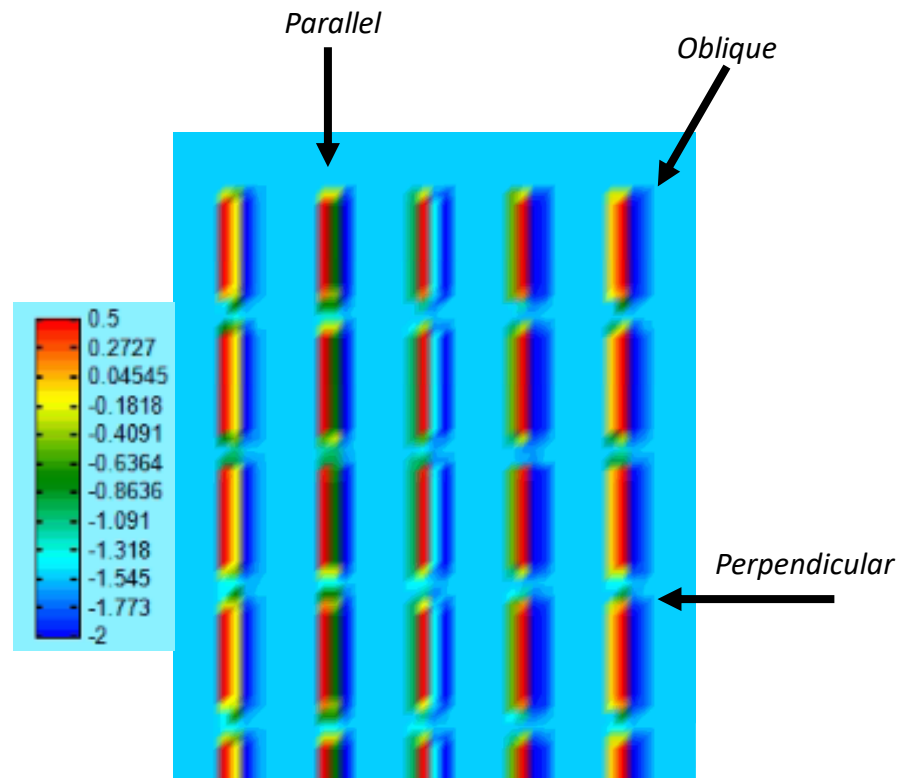


Figure C1. Wind directions tested in separate simulation runs shown relative to a fixed linear terrace field simulation design. Each bathymetry remained fixed and only the wind direction was varied from parallel (0°), oblique (45°), or perpendicular (90°)

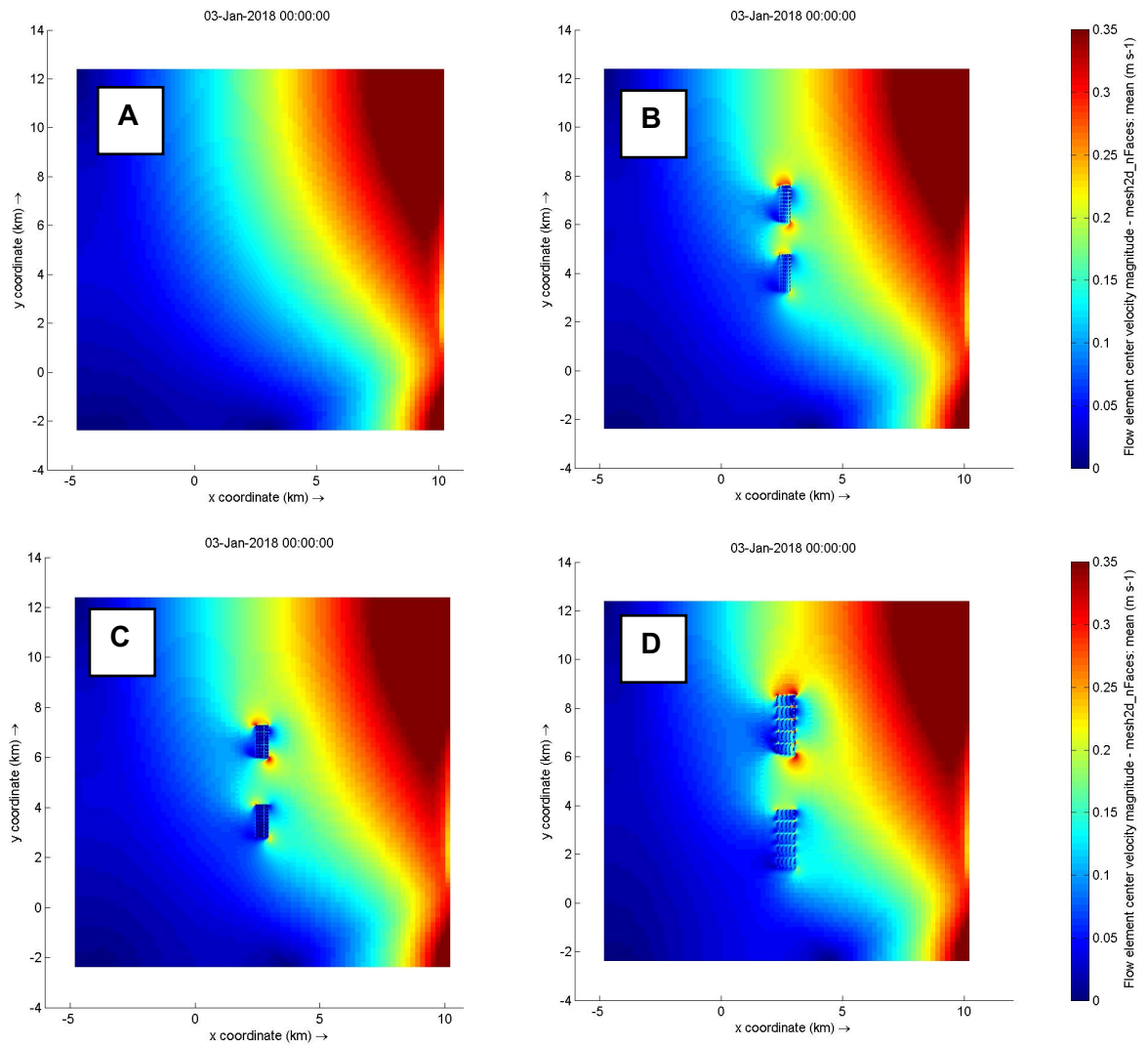


Figure C2. Hydrodynamic impacts (water flow velocities in m/sec) of both (northern and southern) terrace fields during the parallel (0°) wind simulation for each bathymetry at the time step where water velocities reach their maximum during the simulation. A) illustrates the water velocities (m/s) during the control (no terrace, flat bathymetry) run. B) corresponds to the water velocities during the linear terrace simulation. C) and D) represent the water velocities during the grid and chevron terrace runs, respectively.

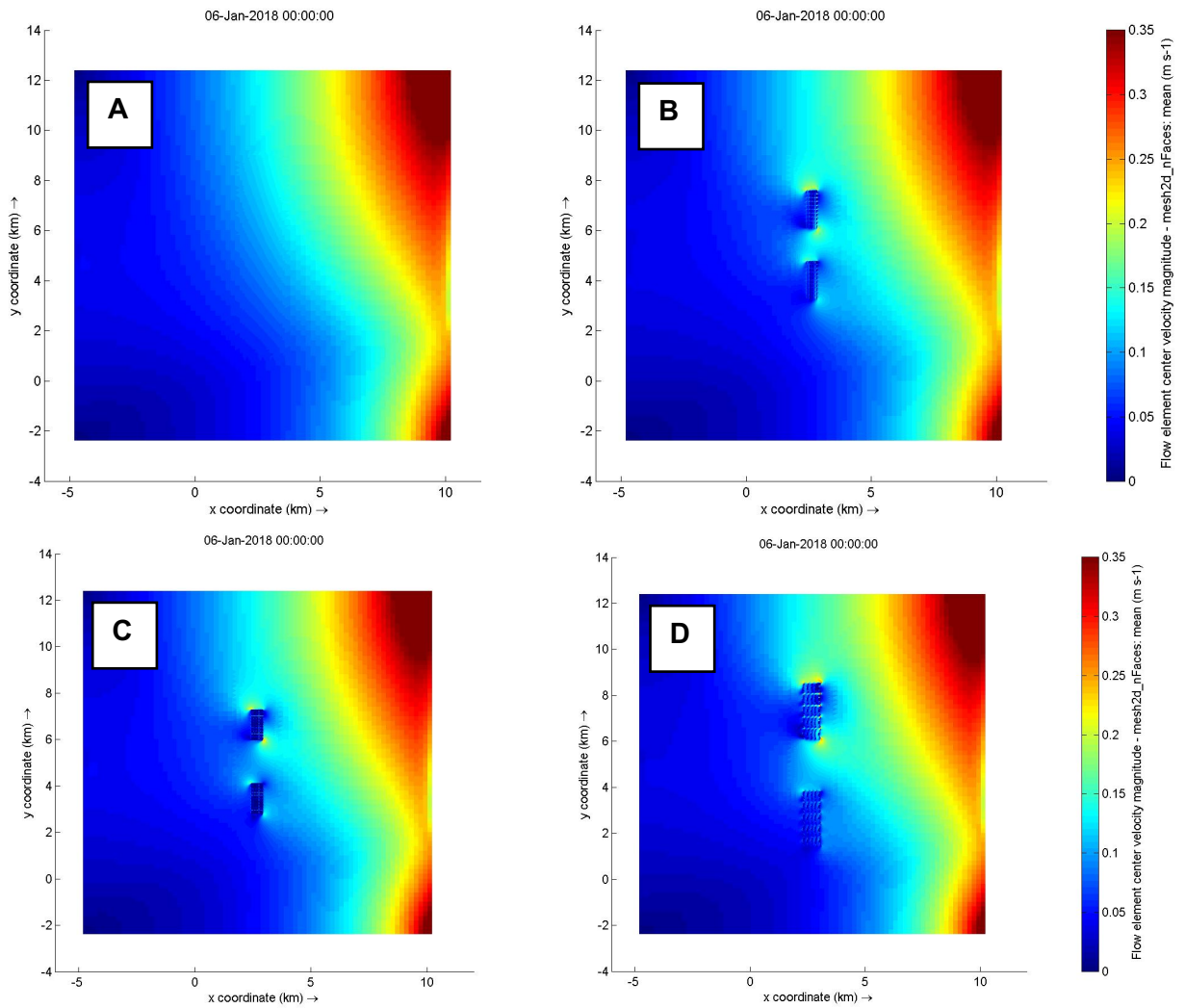


Figure C3. Hydrodynamic impacts (water flow velocities in m/sec) of both (northern and southern) terrace fields during the oblique (45°) wind simulation for each bathymetry at the third time step, where water velocities reach their maximum during the simulation. A) illustrates the water velocities (m/s) during the control (no terrace, flat bathymetry) run. B) corresponds to the water velocities during the linear terrace simulation. C) and D) represent the water velocities during the grid and chevron terrace runs, respectively.

Appendix D: Hydrological Connectivity Analysis for Remote Sensing Study Sites

Hydrologic connectivity is a commonly used term to describe the degree of connection for a particular basin to water supply and allochthonous resources; however, this term is rarely defined quantitatively. Existing marsh terracing research discusses this concept through channel density (Osorio and Linhoss, 2020), which qualitatively describes high channel density (natural or constructed) as the presence of channels into the terrace field of study and low channel density refers to basins with either few to no channels leading into the terrace field or channels blocked by structural marsh management (e.g., levees, dikes, etc.).

For the present study, two quantitative avenues were considered, known herein as percent perimeter and variance. The percent perimeter method calculates the spherical perimeter of the terrace field basin (i.e., circumference of open-water ‘pond’ the terraces were installed within) and determines the percent of the perimeter that are open water (channels). However, without reliable water depth measurements for each channel, the cross-sectional area over which water is exchanged cannot be calculated. Without this information, a site with many shallow channels may present a higher hydrologic connectivity than a site with fewer, deeper channels. Additionally, the percent perimeter value could vary significantly depending on the image selected (of the 4 available per site) due to varying water levels, which could not be reliably adjusted for images that predated CRMS station installation. For example, high water levels may flood lower elevation marsh along a channel edge, which would appear to be a wider channel on aerial imagery and would lead to a larger percent perimeter value. Ultimately, the percent perimeter method was not selected due to the variability associated with unadjusted/uncorrected water level and aerial imagery.

The variance method utilized in the present study measures the 10-day averaged variance about the mean water level obtained from the nearest CRMS station (Table D1) to the study site and is based on the approach presented in Sendrowski et al. (2018). CRMS water level data was available for all 10 geospatial study sites through the 2017 calendar year, which also corresponds to the final image used for every remote sensing study site (i.e., post-terrace construction analysis of each site was measured to 2017, the most recent image available at the time of the study). Further, no hurricanes made landfall in Louisiana during the 2017 calendar year, meaning no sites experienced storm-induced extreme fluctuations in water level over the period of study. To reduce the effects of high frequency water level fluctuations, a 10-day variance was calculated from the CRMS water level results, resulting in 37 variances per site. These 37 variances were averaged to a single value for each site (Table D1), which was interpreted to serve as a proxy for water exchange; thereby, the higher the variance value, the higher the presumed water exchange. Astronomical tidal influences are not reduced using this method. Instead, it seeks to combine astronomical and meteorological tidal impacts in the discussion of exchange because a site with a larger diurnal tidal range would experience more water exchange through the system during a tidal cycle than a site with a smaller (or nonexistent) tidal range. As intended, this method showed greater variance in sites with a

larger astronomical tidal range. Although this method is biased toward the vertical component of water exchange, it does produce a quantifiable estimate of hydrologic connectivity and an alternative to the aforementioned percent perimeter or channel density methods.

Table D1. Hydrologic connectivity values defined for each geospatial study site with distance to their respective CRMS stations from which water level data was obtained. Low, intermediate, and high connectivity are represented by varying shades of blue; the lightest blue represented low connectivity (low water exchange) and the darkest blue is high connectivity (high water exchange).

<i>Site</i>	<i>CRMS site</i>	<i>Distance (km)</i>	<i>Connectivity</i>
1102	0697	0.10	0.016
2015W	0614	2.74	0.003
2015C	0614	2.41	0.003
2015E	0614	2.46	0.003
3008	0535	4.67	0.022
3006	0535	0.64	0.022
5001	0543	0.29	0.046
7001	2825	2.90	0.008
7006N	6303	5.87	0.014
7006S	6303	7.45	0.014

Table D2. Categorical distinctions for parameters (uninterrupted fetch, V_{ASD} , hydrologic connectivity, hurricane impacts) used to predict terrace performance at each remote sensing site. Storm impacts are defined by number of hurricanes which passed the site within six months of terrace construction. Subsidence (mm/y) values were derived from most adjacent/proximal available CRMS station as reported by Jankowski et al. 2017.

<i>Site</i>	<i>Maximum fetch (km)</i>	<i>V_{ASD} (mm/y)</i>	<i>Connectivity</i>	<i>Storm Impacts</i>	<i>Subsidence (mm/y)</i>
1102	1.62	-1.82	0.016	1	4.27
2015W	1.62	4.53	0.003	0	6.62
2015C	2.30	4.53	0.003	0	6.62
2015E	4.00	4.53	0.003	0	6.62
3008	1.39	-1.10	0.022	1	5.11
3006	2.02	-1.10	0.022	1	5.11
5001	40+	-2.15	0.046	1	15.57
7001	1.86	-4.49	0.008	0	17.26
7006N	1.42	-3.33	0.014	0	15.81
7006S	4.16	-3.33	0.014	0	15.81

Biography

Marie is a loud and proud Jersey girl with a love for warm weather and Southern food. Following her enthusiasm for collegiate athletics, she attended Duke University, where she became a Cameron Crazie and serendipitously fell into Earth and Ocean Sciences. Upon graduation, she moved to New Orleans, LA to research coastal restoration with Mead Allison and has since continued onto her dream job at USACE-ERDC-CHL with the River and Estuarine Engineering Branch in Vicksburg, MS.